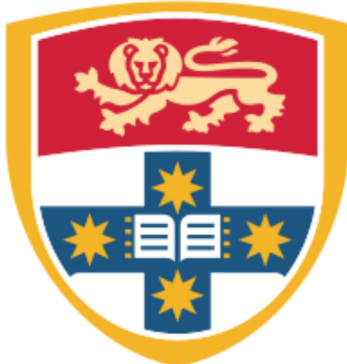

Micro-UAV Optimisation Including Propeller Slipstream Effects

Author:

Thomas RYAN

470 390 467



THE UNIVERSITY OF SYDNEY

School of Aeronautical, Mechanical and Mechatronic Engineering

*Submitted to the University of Sydney in Partial Fulfilment of the
Requirements of a Bachelor of Engineering Honours
(Aeronautical Engineering)*

Declaration of Contribution

I, Thomas RYAN, declare that this thesis titled "Micro-UAV Optimisation Including Propeller Slipstream Effects" and the following list of work completed are my own. I have consulted the published work of others, clearly stating the source of the finding. The following is a list of work that is my own:

- I reviewed literature that explored the areas of research relevant to this thesis topic.
- I conducted computational validation studies of VAP 3.5.
- I created and validated a static stability analysis function in MATLAB, using the potential flow method VAP 3.5.
- I adapted MATLAB code from Dr Dries Verstraete, integrating VAP 3.5 and the static stability analysis function into an optimisation structure.
- I post-processed data from optimisation studies and analysed the results.

The above statements accurately outline the student's contribution



Student

14/11/2021

Date

Abstract

Micro Aerial Vehicles (MAVs) have attracted increasing attention due to the improved performance provided by the miniaturisation of electric propulsion. With the increasing demand for high performance MAVs, traditional aircraft design methods are being replaced with numerical optimisation approaches. Existing research in this area has not currently extended to including propeller slipstream effects in the MAV optimisation. However, this needs to be considered because the propeller wake can deform the wing lift distribution, altering performance and changing the optimal MAV geometry. This thesis investigates the importance of propeller slipstream effects on MAV design optimisation.

The influence of propeller wake on aerodynamic performance was modelled with a Higher-Order Free Wake potential flow method. A numerical stability analysis function was created and validated at low Reynolds numbers. These programs were then integrated into a genetic algorithm to perform multi-objective optimisation with static stability constraints.

Three MAV configurations and two size classes (30 cm and 45 cm) were optimised, with and without the effect of propeller slipstream. The optimisations without propeller effects generated MAV designs with higher lift-to-drag ratios compared to published MAVs of a similar size. The optimisations with propeller effects produced significantly different optimal designs, featuring a maximum lift-to-drag ratio 25% to 35% lower than the optimisation without propellers for the 45 cm class. The reduction in lift-to-drag ratio was 25% less for the 30cm class. Furthermore, propeller slipstream reduced the longitudinal stability of the MAV, requiring changes in wing sweep and root chord to meet stability constraints. The optimisation results suggest that the influence of geometric variables on optimisation objectives changes with the inclusion of propeller effects. Therefore, it is important that effects from propeller-wing interaction be included in MAV optimisations.

Contents

| | |
|---|-----------|
| List of Figures | iv |
| List of Tables | ix |
| 1 Introduction | 1 |
| 1.1 Objectives | 2 |
| 1.2 Relevant Theory | 3 |
| 1.3 Thesis Structure | 3 |
| 2 Literature Review | 4 |
| 2.1 Non-Linear Lift Distribution | 4 |
| 2.2 Low Reynolds Number Effects | 6 |
| 2.3 Propeller Wing Interaction | 10 |
| 2.3.1 High Reynolds Numbers | 10 |
| 2.3.2 Low Reynolds Numbers | 13 |
| 2.3.3 Stability Effects of Propeller Slipstream | 15 |
| 2.4 MAV Optimisation | 16 |
| 3 Theory and Methodology | 18 |
| 3.1 High-Order Free Wake Method | 19 |
| 3.1.1 VAP 3 | 22 |
| 3.1.2 Time Dependence of Propeller-Wing Interaction | 22 |
| 3.2 Mass Calculation | 23 |
| 3.3 Stability Calculation | 25 |
| 3.4 Optimiser Algorithm | 27 |
| 4 Validation and Calibration of VAP 3 | 30 |
| 4.1 Wing Validation | 30 |

| | | |
|----------|---|-----------|
| 4.2 | Propeller Validation | 32 |
| 4.3 | Propeller-Wing Interaction | 34 |
| 4.4 | Stability Validation | 35 |
| 4.5 | Convergence and Time Dependency | 37 |
| 5 | Optimisation Results and Discussion | 41 |
| 5.1 | MAV Classes | 41 |
| 5.1.1 | GenMAV | 42 |
| 5.1.2 | Flying Wing | 42 |
| 5.1.3 | Winglet Class | 43 |
| 5.2 | Optimiser Set Up | 44 |
| 5.2.1 | Variables | 44 |
| 5.2.2 | Objectives | 45 |
| 5.2.3 | Constraints | 46 |
| 5.3 | Optimisation Without Propeller | 48 |
| 5.3.1 | 30 cm Class | 48 |
| 5.3.2 | 45 cm Class | 53 |
| 5.4 | Optimisation With Propeller | 58 |
| 5.4.1 | 45cm Class with 5 inch propeller | 58 |
| 5.4.2 | 45 cm Class with 7 inch propeller | 62 |
| 5.4.3 | 30 cm Class with 4 inch propeller | 65 |
| 5.5 | Variable Correlation | 68 |
| 6 | Conclusions and Future Work | 71 |
| 6.1 | Conclusions | 71 |
| 6.2 | Future Work | 73 |
| A | Appendix A Relevant Theory | 81 |
| A.1 | Reference Frames | 81 |
| A.2 | Aircraft Geometry | 83 |
| A.3 | Aerodynamic Forces and Coefficients | 87 |

| | | |
|-------------------|--|-----------|
| A.4 | Static Longitudinal Stability | 89 |
| A.5 | Static Lateral-Directional Stability | 90 |
| Appendix B | VAP 3.5 Input Settings | 93 |
| B.1 | Simulation Settings | 93 |
| B.2 | Solver Settings | 93 |
| B.3 | Flight Conditions | 94 |
| B.4 | Vehicle and Propeller Geometry | 94 |
| Appendix C | Extra Optimisation Figures | 98 |

List of Figures

| | |
|---|----|
| 2.1 Streamlines and pressure contours of the flow around a flat plate (Cosyn and Vierendeels, 2006) | 5 |
| 2.2 Laminar separation bubble detailing flow behaviour (Mueller & DeLaurier, 2003) | 6 |
| 2.3 Flow field around an airfoil at various Reynolds numbers (Winslow et al, 2018) | 7 |
| 2.4 Boundary layer visualisation showing laminar separation bubble with no turbulator strip (Trips, 2010) | 9 |
| 2.5 Boundary layer visualisation with turbulator strip generates no separation bubble (Trips, 2010) | 9 |
| 2.6 Influence areas of the propeller wing interaction varies with propeller spin direction (Velduis, 2004) | 11 |
| 2.7 Induced angle of attack on propeller blade by leading edge upwash (Velduis, 2004) | 13 |
| 2.8 The difference in flow behaviour can be seen with propeller turned off on left and on in the right image. At 9 degrees angle of attack the flow is almost fully separated with propeller disabled. With the tractor propeller turned on the slipstream maintains attachment until the trailing edge. Outside of the slipstream the flow reattaches forming a laminar separation bubble (Ananda et al, 2018) | 15 |
| 2.9 Variation of pitching moment with propeller size and rpm (Shams et al, 2020) | 16 |
| 2.10 The long range Mini-UAV <i>Eternity</i> with two fuselage configurations (Bronz et al, 2009) | 17 |
| 3.1 Optimisation structure including evaluation in VAP 3.5 and objective handling with NSGA-II | 18 |
| 3.2 Higher-order vorticity distribution across the DVE streamwise and transverse directions (Cole, 2016) | 20 |

| | | |
|------|--|----|
| 3.3 | Discretisation of rectangular wing into two DVEs (Cole, 2016) | 21 |
| 3.4 | Example of wake relaxation in a propeller-wing system (Cole et al, 2019) . . | 21 |
| 3.5 | Comparison between time accurate and time averaged lift predictions for varying panel densities and timesteps (Cole, 2016) | 23 |
| 3.6 | Example of dominated and non-dominated solutions (Pareto front) | 28 |
| 3.7 | Iteration process of the NSGA-II algorithm including evaluation, sorting, crossover and mutation (Chen, 2016) | 29 |
| 4.1 | WING000300: C_L vs C_D | 31 |
| 4.2 | WING000300: L/D vs C_L | 31 |
| 4.3 | WING000500: C_L vs C_D | 31 |
| 4.4 | WING000500: L/D vs C_L | 31 |
| 4.5 | WING001000: C_L vs C_D | 31 |
| 4.6 | WING001000: L/D vs C_L | 31 |
| 4.7 | Front view of propellers used in validation study. Not to scale | 32 |
| 4.8 | GWS4x4 Thrust Coefficient | 33 |
| 4.9 | GWS4x4 Torque Coefficient | 33 |
| 4.10 | GWS5x43 Thrust Coefficient | 33 |
| 4.11 | GWS5x43 Torque Coefficient | 33 |
| 4.12 | APC7x6 Thrust Coefficient | 33 |
| 4.13 | APC7x6 Torque Coefficient | 33 |
| 4.14 | Dimensions and layout of the PROWIM model (Velduis, 2004) | 34 |
| 4.15 | VAP model of the PROWIM system | 34 |
| 4.16 | Wing normal force distribution for the PROWIM validation model | 35 |
| 4.17 | GenMAV side view. Values in inches (Stewart et al, 2007) | 36 |
| 4.18 | GenMAV top view. Values in inches (Stewart et al, 2007) | 36 |
| 4.19 | Pitch, roll and yaw moment coefficients calculated in VAP 3 compared to AVL results | 36 |
| 4.20 | Main wing normal force convergence under the influence of propeller slipstream | 39 |

| | | |
|------|--|----|
| 4.21 | Horizontal tail normal force convergence under the influence of propeller slipstream | 39 |
| 4.22 | C_{m_α} convergence with no propeller | 40 |
| 4.23 | C_{m_α} convergence including propeller | 40 |
| 4.24 | C_{l_β} convergence with no propeller | 40 |
| 4.25 | C_{l_β} convergence including propeller | 40 |
| 4.26 | C_{n_β} convergence with no propeller | 40 |
| 4.27 | C_{n_β} convergence including propeller | 40 |
| 5.1 | VAP 3.5 model of the GenMAV class | 42 |
| 5.2 | GenMAV model (Stewart et al, 2007) | 42 |
| 5.3 | VAP 3.5 model of the Flying Wing class | 43 |
| 5.4 | PMAV model (Albertani et al, 2004) | 43 |
| 5.5 | VAP 3.5 model of the Winglet class | 44 |
| 5.6 | Winglet model (Van Magill, 2016) | 44 |
| 5.7 | Iteration history of Flying Wing 30cm class | 48 |
| 5.8 | Iteration history of Winglet 30cm class | 48 |
| 5.9 | Flying Wing 30cm: Root Chord | 50 |
| 5.10 | Winglet 30cm: Root Chrod | 50 |
| 5.11 | Flying Wing 30cm: Aspect Ratio | 51 |
| 5.12 | Winglet 30cm: Aspect Ratio | 51 |
| 5.13 | Flying Wing 30cm: Sweep | 52 |
| 5.14 | Winglet 30cm: Sweep | 52 |
| 5.15 | Flying Wing 30cm: Dihedral | 52 |
| 5.16 | Winglet 30cm: Dihedral | 52 |
| 5.17 | Iteration history of Flying Wing 45cm class | 53 |
| 5.18 | Iteration history of GenMAV 45cm class | 53 |
| 5.19 | Flying Wing 45cm: Aspect Ratio | 55 |
| 5.20 | Genmav 45cm: Aspect Ratio | 55 |
| 5.21 | Flying Wing 45cm: Root Chord | 55 |

| | |
|---|----|
| 5.22 Genmav 45cm: Root Chord | 55 |
| 5.23 Flying Wing 45cm: Sweep | 56 |
| 5.24 GenMAV 45cm: Sweep | 56 |
| 5.25 Flying Wing 45cm: C_{m_α} | 57 |
| 5.26 GenMAV 45cm: C_{m_α} | 57 |
| 5.27 Flying Wing 45cm: C_{l_β} | 57 |
| 5.28 GenMAV 45cm: C_{l_β} | 57 |
| 5.29 Flying Wing 45cm: C_{n_β} | 57 |
| 5.30 GenMAV 45cm: C_{n_β} | 57 |
| 5.31 Iteration history of the 45cm Flying Wing including GWS 5x4.3 | 59 |
| 5.32 Iteration history of the 45cm GenMAV including GWS 5x4.3 | 59 |
| 5.33 Flying Wing 45cm with 5" prop: Root Chord | 61 |
| 5.34 Genmav 45cm with 5" prop: Root Chord | 61 |
| 5.35 Flying Wing 45cm with 5" prop: Wing Sweep | 62 |
| 5.36 Genmav 45cm with 5" prop: Wing Sweep | 62 |
| 5.37 Flying Wing 45cm with 5" prop: Aspect Ratio | 62 |
| 5.38 GenMAV 45cm with 5" prop: Aspect Ratio | 62 |
| 5.39 Iteration history of the 45cm Flying Wing including APC 7x6 | 63 |
| 5.40 Iteration history of the 45cm GenMAV including APC 7x6 | 63 |
| 5.41 Flying Wing 45cm with 7" prop: Sweep | 64 |
| 5.42 GenMAV 45cm with 7" prop: Sweep | 64 |
| 5.43 Optimal (Max L/D) designs for the 45cm GenMAV class with varying propeller models. | 65 |
| 5.44 Optimal (Max L/D) designs for the 45cm Flying Wing class with varying propeller models. | 65 |
| 5.45 Iteration history of the 30cm Flying Wing including " | 66 |
| 5.46 Iteration history of the 30cm Winglets including GWS 4x4 | 66 |
| 5.47 30 cm Flying Wing with 4" prop: Sweep | 67 |
| 5.48 30 cm Winglet with 4" prop: Sweep | 67 |
| 5.49 30 cm Flying Wing with 4" prop: Dihedral | 67 |

| | | |
|------|--|----|
| 5.50 | 30 cm Winglet with 4" prop: Dihedral | 67 |
| 5.51 | Variable correlations for the 30cm Flying Wing optimisation without propeller | 69 |
| 5.52 | Variable correlations for the 30cm Flying Wing optimisation with 4" propeller | 69 |
| 5.53 | Variable correlations for the 45cm GenMAV optimisation without propeller . | 70 |
| 5.54 | Variable correlations for the 30cm GenMAV with 5" propeller | 70 |
| A.1 | Relationship between aircraft reference frames | 82 |
| A.2 | Key aircraft geometric parameters | 84 |
| A.3 | Low, medium and high aspect ratio wings with constant wing area S | 85 |
| A.4 | Example of wing dihedral angle | 86 |
| A.5 | Example of wing twist and incidence | 87 |
| A.6 | Diagram of aerodynamic forces acting on aircraft | 88 |
| A.7 | Location of centre of gravity (CG), neutral point (NP) and aerodynamic centre (AC) | 90 |
| A.8 | Pitch, yaw and roll moments | 91 |
| A.9 | Aircraft experiencing a sideslip disturbance | 91 |
| C.1 | Winglet 30cm: Taper | 98 |
| C.2 | Winglet 30cm: Winglet Volume | 98 |
| C.3 | Winglet 30cm with 4" prop: Taper | 98 |
| C.4 | Winglet 30cm with 4" prop: Winglet Volume | 98 |
| C.5 | Variable correlations for the 45cm Flying Wing optimisation without propeller | 99 |
| C.6 | Variable correlations for the 45cm Flying Wing optimisation with GWS5x4.3 | 99 |

List of Tables

| | | |
|-----|---|----|
| 3.1 | Powerplant and electrical mass breakdown for 30 cm class MAV | 25 |
| 3.2 | Powerplant and electrical weight breakdown for 45 cm class MAV | 25 |
| 4.1 | Trips (2010) validation case wing geometries | 30 |
| 4.2 | Stability derivative from AVL and VAP 3.5 | 37 |
| 4.3 | Computation times for the stability calculations including propeller (min:sec) | 38 |
| 5.1 | Optimisation variables used for all MAV configurations | 45 |
| 5.2 | Size Constraints | 47 |
| 5.3 | Trim Constraints | 47 |
| 5.4 | Stability Constraints | 47 |
| 5.5 | 30 cm span class optimal designs without propeller compared to MAVs from literature | 49 |
| 5.6 | 45 cm span class optimal designs without propeller compared to MAVs from literature | 54 |
| 5.7 | Propeller optimisations outline | 58 |
| 5.8 | 45 cm class optimal designs including propeller compared to MAVs from literature | 60 |

Acknowledgements

There are many people who have helped and supported me during my Honours year. First and foremost, I would like to thank my supervisor, Dr Dries Verstraete, who has dedicated so much of his time to guiding and helping me throughout my thesis. He has truly gone above and beyond what was required. Dries' passion for engineering sciences and dedication to his students was a constant inspiration, motivating me through the most challenging periods of the project.

To my parents Peter and Becky, as well my sister Anna, thank you for your unfaltering support, encouragement and proof reading. You have been my rock throughout my undergraduate degree and have given me the confidence to set my goals high and push myself in everything I do. I am extremely grateful to have such a loving and supportive family.

Finally, to my friends Abbey, James and Jaz, who have studied along side me for the past five years, and accompanied me through countless late nights, I truly wouldn't have been able to do it without you.

In memory of Toby, whose gentle heart always brought happiness to those around him

Chapter 1

Introduction

Over the past decade, interest in Micro Unmanned Aerial Vehicles (MAVs) has grown alongside advances in light weight battery and airframe technologies. These advancements have increased the range of applications for MAVs from primarily military to agricultural and emergency services (Mueller & DeLaurier, 2003). Until the early 2000s, systems and avionics weight limited performance significantly. However, recent technological progress has significantly expanded the MAV design envelope. With the increasing capabilities of MAVs due to miniaturization of technology, there has been increasing interest in MAV design. Traditional approaches to aircraft design, such as the conceptual methods from Raymer (2006) and Roskam (2000), are effective at producing safe and reliable designs. However, these methods struggle to create highly optimised designs with maximised performance. Furthermore, there is doubt about the accuracy of these methods at lower Reynolds numbers. Instead, numerical optimisation, including specifically designed aerodynamic solvers, is becoming more popular.

MAV optimisation differs from full scale aircraft optimisation because of the low Reynolds number aerodynamics and non-typical mission requirements. MAVs are often designed for missions requiring coordination with other MAVs as well as long endurance and large payloads compared to aircraft mass. To maximise endurance and range, a high efficiency lifting surface must be designed. However, aerodynamic force prediction of MAVs is challenging due to the low Reynolds number operating conditions. The small size and low speed of MAVs can produce aerodynamic effects such as laminar separation bubbles and non-linear lift distributions, detrimental to aircraft performance. As the demand for light-weight, high performance MAV designs increases, these challenges will need to be overcome.

Several MAV optimisation studies have been published with varying mission requirements.

Trips (2010), Bronz et al. (2009) and Hassanalian (2014)) are a few examples of recent optimisations using purpose-built optimisation algorithms and aerodynamic solvers. None of these studies include the effects of propeller slipstream on the optimisation even though the propeller slipstream can have significant impacts on aerodynamic performance and static stability. This thesis aims to investigate the feasibility and importance of including propeller slipstream effects in an MAV optimisation structure.

A Higher-Order Free Wake potential flow method is used to evaluate aerodynamic performance of MAV designs. This method was selected due to its numerical stability with unsteady wakes from propeller modelling. The static longitudinal and lateral stability characteristics are calculated using a novel numerical stability function. A Non-dominated Sorting Genetic Algorithm (NSGA-II) is used to perform multi-objective optimisation on MAV wing and tail geometries. The particular interest of this thesis is in defining the importance of propeller slipstream on the optimised MAV models.

1.1 Objectives

The primary objectives of this thesis are as follows:

- To investigate the feasibility of integrating the effects of propeller slipstream into a numerical optimisation of MAVs.
- To determine the importance of propeller slipstream effects on the optimised MAV designs.

These primary objectives will be achieved using the secondary objectives:

- To perform an in-depth literature review on the aerodynamics of MAVs and to adjust the optimiser structure based off these findings.
- To develop a longitudinal and lateral stability function to estimate the feasibility of MAV designs.
- To validate VAP 3.5 in low Reynolds number flow conditions for propeller-wing interaction.
- To integrate VAP 3.5 and the stability function into an optimisation algorithm and

determine optimal MAV geometries based on weight and performance objectives.

1.2 Relevant Theory

A summary of relevant concepts, theory and nomenclature has been provided in Appendix A. Aircraft geometry parameters and reference axes will be defined. These definitions will be used to outline the aerodynamic forces acting on an aircraft, including the longitudinal and lateral-directional stability criteria.

1.3 Thesis Structure

This thesis is structured as follows:

- **Chapter 1** provides context for the research topic as well defining the primary and secondary objectives of the thesis.
- **Chapter 2** presents a review of relevant literature. The main topics are low Reynolds number aerodynamics, propeller-wing interaction and MAV design optimisation.
- **Chapter 3** outlines the structure of the optimisation. The optimisation algorithm, MAV mass calculation and aerodynamic solver are described. The creation and integration of a static stability function are also explained.
- **Chapter 4** presents validation studies of the aerodynamic solver for a range of different configurations. The static stability function is also validated. Lastly, the convergence and time dependence of the stability function are investigated.
- **Chapter 5** outlines the optimiser set up, including the optimisation classes and variables. The results of the optimisation are then presented and discussed. Optimisations are completed with and without propeller and the results are compared.
- **Chapter 6** concludes the thesis, summarising the key findings and providing suggestions for future work.

Chapter 2

Literature Review

Wing shape design and airfoil selection are crucial design variables used to influence aircraft performance. The ultimate goal of wing design is to produce an aerodynamically stable, high efficiency lifting surface (Mueller, 2007). The lift-to-drag ratio (L/D) is a key measure of wing efficiency which should be maximised in the design process. MAV wing design is complicated by the non-linear lift distribution generated by low aspect ratio wings (Cosyn and Vierendeels, 2006). Furthermore, MAVs can experience laminar separation bubbles due to low Reynolds numbers. These low pressure cells significantly increase drag and can limit wing efficiency (Mueller, 2007). These effects cause MAV wing design to diverge substantially from two dimensional (2D) numerical results. Instead, more sophisticated solutions, which take viscous and non-linear 3D effects into account, are required.

2.1 Non-Linear Lift Distribution

MAVs are often designed for missions requiring a small size and weight. For example, the hand deployable PMAV (Pocket MAV) was designed to fit in a pocket when folded (Albertani et al, 2004). To maintain wing area with wingspan constraints, MAV design often features a low aspect ratio main wing ($AR < 3$). A major challenge in MAV design is reducing the negative effects of wingtip vortices on the lift distribution. The pressure differential between the upper and lower surface causes flow around the wing tip, generating a circulating vortex when combined with the free stream, shown in Figure 2.1. This vortex creates a low pressure cell around the wing tip that results in a deformed lift distribution (Cosyn and Vierendeels, 2006).

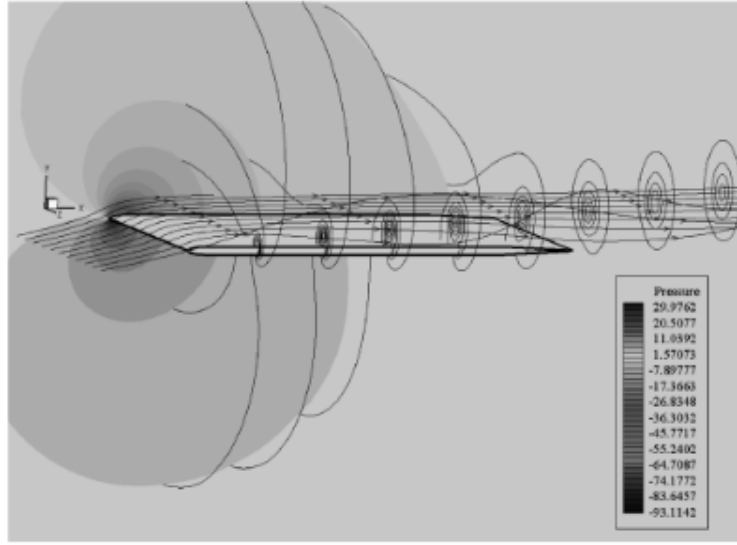


Figure 2.1: Streamlines and pressure contours of the flow around a flat plate (Cosyn and Vierendeels, 2006)

In MAVs, the low aspect ratio exposes more wing area to the low pressure cell created by the vortex than on higher aspect ratio wings. This produces a larger effect on lift distribution and drag than for high aspect ratio wings. Mueller showed that wings with an aspect ratio of less than 1.25 exhibited significantly non-linear lift distributions, characteristic of large wingtip vortices. Aspect ratios above 1.25 created more linear lift distributions (Mueller & Pelletier, 2000).

Early wind tunnel investigations into the aerodynamics of low aspect ratio wings showed that aerodynamic performance was dependent on tip geometry (Zimmerman, 1936). Zimmerman also showed that the low aspect ratio planforms required a higher angle of attack to produce the same lift coefficient compared to high aspect ratio wings (Zimmerman, 1936). The high angle of attack and large tip chord were used to explain the sensitivity of low aspect ratio wings to wingtip vortices (Hoerner & Borst, 1985).

The non-linear lift distribution has a significant effect on the chord-wise centre of lift. Mueller showed that the center of lift was more sensitive to angle of attack on low aspect ratio wings than on higher aspect ratio wings (Mueller & DeLaurier, 2003). At low angles of attack, lift is primarily generated by the free stream pressure difference which places the centre of lift at approximately the quarter chord. As angle of attack increases, the wingtip vortices

increase in strength and non-linear vortex lift dominates. This results in the centre of lift moving aft, towards the more developed low pressure vortex. This transition from linear to non-linear lift distributions was found to be more exaggerated in low aspect ratio wings (Mueller, 2007).

2.2 Low Reynolds Number Effects

Laminar separation and reattachment at low Reynolds numbers (approximately 50,000 to 300,000) is a well researched field. Schmitz measured the aerodynamic characteristics of various geometries at Reynolds numbers from 2.1×10^4 to 16.8×10^4 (Schmitz, 1970). Schmitz described in detail how the boundary layer developed and separated, creating a low pressure zone of ‘hysteresis’ where reverse flow vortices were created. This is shown in Figure 2.2.

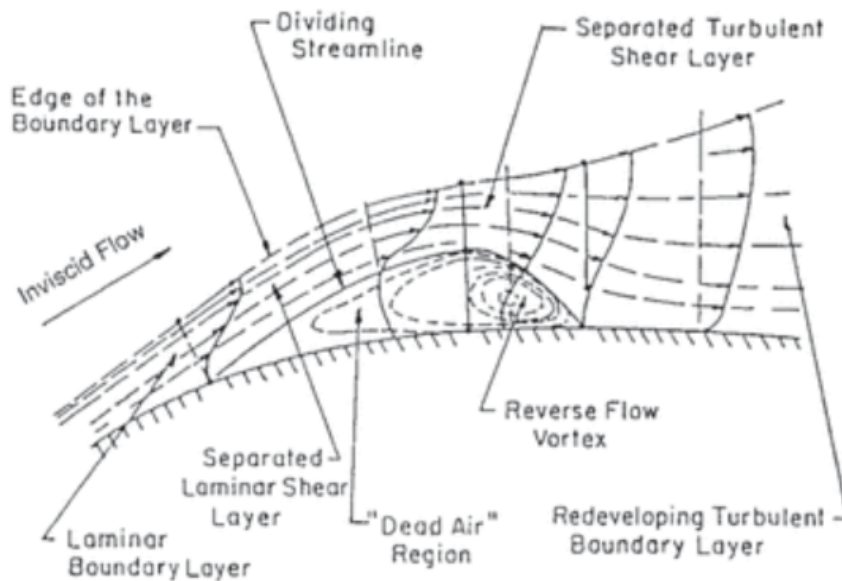


Figure 2.2: Laminar separation bubble detailing flow behaviour (Mueller & DeLaurier, 2003)

After this, extensive research (McMasters & Henderson 1980, Lissaman 1983, Mueller 1985) showed how the performance of traditional airfoils (designed for Reynolds numbers greater than 500,000) deteriorates dramatically at Reynolds number lower than 200,000 because of laminar boundary-layer separation. These effects are a critical consideration for MAV wing

design which can experience Reynolds numbers as low as 30,000.

The discussion on low Reynolds number aerodynamics will begin with results from Carmichael (1981) and Mueller (1985) who made general observations on flow behaviour for Reynolds numbers from 10^3 to 10^9 . This discussion is supported by Figure 2.3 which shows how flow fields develop with Reynolds number.

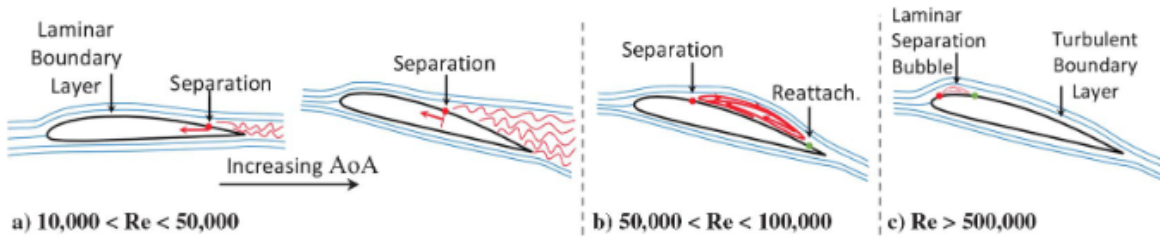


Figure 2.3: Flow field around an airfoil at various Reynolds numbers (Winslow et al, 2018)

MAV wing design focuses on Reynolds numbers from 30,000 to 200,000 (Mueller, 1985). Despite the relatively small Reynolds number range experienced by MAV's, there are distinct flow regimes that create unique effects on airfoils:

- **Re 10,000 to 30,000**

Very low Reynolds numbers produce laminar flow regimes where streamlines are aligned and there is little turbulence. In this regime, the flow is resistant to transitioning into turbulent flow. However, the flow is sensitive to pressure gradients such as those created by the camber of an airfoil. As the angle of attack increases, laminar flow separation occurs from the trailing edge first, moving towards the leading edge. The detached flow does not have enough energy to transition and reattach to the airfoil. As a result airfoils in this regime produce very high drag and will stall at very low angles of attack as shown in Figure 2.3 a. Maximum lift coefficients before stall are approximately 0.5 for regular airfoils (Mueller, 1985). This flow regime is generally lower than operating conditions for MAV's. Paper planes and small birds experience this range of Reynolds numbers most commonly.

- **Re 30,000 to 70,000**

In this range the flow becomes more energized however maintains sensitivity to the

adverse pressure gradient created by the cambered upper surface of the airfoil. With the increased energy, the flow is less resistant to flow transition and separates from the airfoil upper surface earlier than at very low Reynolds numbers. The separated shear layer gains momentum from the free-stream and can reattach to the airfoil near the trailing edge. This separation and reattachment is known as a Laminar Separation Bubble (LSB), shown in Figure 2.3b. Inside the separation bubble a low pressure reverse flow vortex is generated. This low pressure zone increases pressure drag. The LSB effect on drag increases with angle of attack until full separation occurs and the airfoil stalls. At angles of attack close to stall the flow will oscillate between fully detached flow and large separation bubbles. This oscillation is known as hysteresis and produces unpredictable performance. This is the lower end of operating Reynolds numbers for MAV's. In this range airfoil selection is critical as thick airfoils (6% and above) create larger pressure gradients on the upper surface and can risk generating large LSBs which substantially increase drag (Mueller, 1985).

- **Re 70,000 to 200,000**

Flow reattachment occurs closer towards the leading edge in this range of Reynolds numbers. The free stream now energizes the detached flow enough to reattach shortly after detachment, producing smaller separation bubbles. As a result airfoils in this regime experience increased laminar flow with a turbulent boundary layer. In this range airfoil performance increases proportionally with Reynolds number and the reduction of separation bubble size. Large LSBs can still occur at high angles of attack for thick airfoils. Most MAVs will operate in this range (Cosyn and Vierendeels, 2007).

- **Above Re 200,000**

Airfoil performance improves drastically above a Reynolds number of 200,000. On the upper airfoil surface the laminar boundary layer separates into a shear layer which is reattached as a turbulent boundary layer. The free stream momentum is normally sufficient to maintain attachment of the boundary layer until the trailing edge. However at sufficiently high angles of attack the turbulent boundary layer will separate from the trailing edge first. This separation will propagate towards the leading edge with

increased angle of attack leading to a complete stall of the airfoil. Airfoil stall creates huge increases in drag and decreases in lift.

The key Reynolds number range for MAV design is from 30,000 to 200,000 (Mueller, 2007). In this range LSBs are very common. Roberts (1980) associated the drag rise seen when the detached shear layer fails to reattach, known as ‘bursting’ of the bubble, to the sharp drop in low pressure peak near the leading edge. Trips (2010) investigated the drag increase found with increasing LSB size. His findings suggested that the increase in drag is caused by the generation of the low pressure cell, causing increased lift induced drag in accordance with Mueller and Roberts’ findings. Interestingly Trips showed that an increase in LSB size also causes an increase in profile drag. Trips explained this by showing how there was a large momentum loss in the boundary layer at the point of transition.

Investigations have been made into the artificial tripping of the laminar separation bubble. These methods often involve material strips or varying surface roughness to stimulate transition to turbulent flow. Trips (2010) showed that a turbulator strip could successfully transition the boundary layer to turbulent flow before the natural LSB occurred. The turbulator was placed at 5 % of the airfoil chord, before laminar separation occurred, and prevented the creation of a separation bubble. As a result the airfoil performance improved. These results are shown in Figures 2.4 and 2.5.

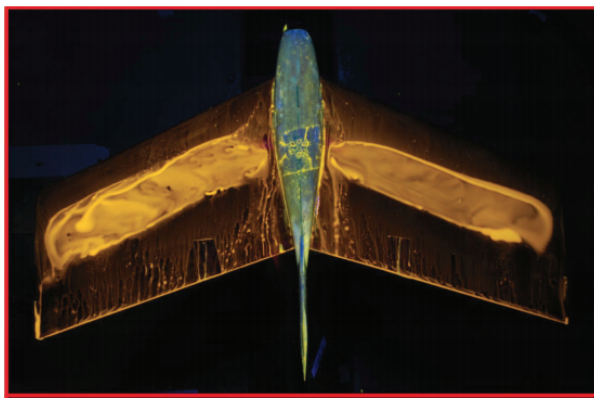


Figure 2.4: Boundary layer visualisation showing laminar separation bubble with no turbulator strip (Trips, 2010)

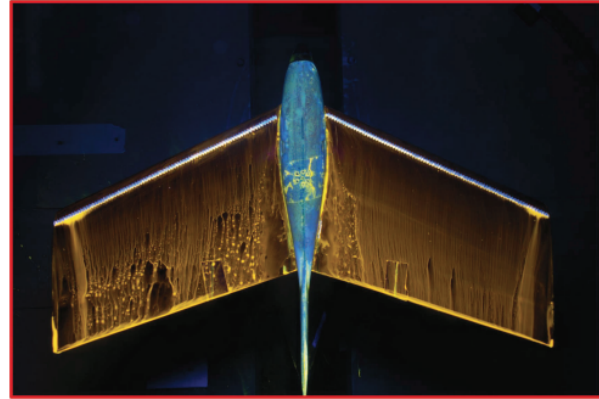


Figure 2.5: Boundary layer visualisation with turbulator strip generates no separation bubble (Trips, 2010)

This investigation built on the work of Drela (1988) and Wortmann (1974) who both experimented with transition devices. Drela found that artificial transition devices were effective at reducing LSB size and improving airfoil performance at Reynolds numbers below 200,000. Wortmann looked at more gradual generation of adverse pressure gradients on the upper airfoil surface. Wortmann successfully amplified airfoil performance by inflecting the laminar boundary layers (Wortmann, 1974).

2.3 Propeller Wing Interaction

Propellers generate swirl velocities and higher dynamic pressure downstream. For propellers mounted on a wing, this altered flow field can deform the local lift distribution on the wing. The unsteady wake and complex swirl patterns turbulence generated by propellers make modelling the propeller-wing interaction challenging. High fidelity numerical solutions such as Reynolds Averaged Navier Stokes (RANS) CFD methods are effective, however, they are computationally expensive. The wing also affects the upstream flow which causes an induced angle of attack on the propeller blades. As an alternative to two way coupled RANS CFD, a number of one way and pseudo two-way coupled methods for modelling propeller wing interactions have been developed recently. Most of these methods focus on producing reasonably accurate results as fast as possible, used for preliminary design analysis. The investigation of propeller-wing interaction will begin with high Reynolds number flows. Propeller-wing interaction at low Reynolds numbers, an area of growing research, will then be discussed.

2.3.1 High Reynolds Numbers

The high disc loading of large modern tractor propeller aircraft, such as the C-130 Hercules and M-28, produces a significant change in flow conditions in the propeller wake. The swirl velocities and increased dynamic pressure experienced by the wing aft of propeller deform the lift distribution and affect overall wing performance. Just as the propeller wake influences the wing loading, the wing airfoil can influence the flow conditions in the propeller. Despite this, many propeller-wing interaction studies ignore the wing effect on the propeller and accept

a one way coupled method. This is because two-way coupling makes accurate modelling of propeller-wing interaction more challenging, often requiring significantly more computation power.

The propeller generates an increased axial velocity distribution along the propeller blade. The higher axial velocities are seen near the blade tip (Velduis, 2004). Furthermore tangential components of velocity due to the propeller rotation generate strong swirl vortices and uneven pressure distributions. Figure 2.6 shows the regions of influence of the propeller on the wing.

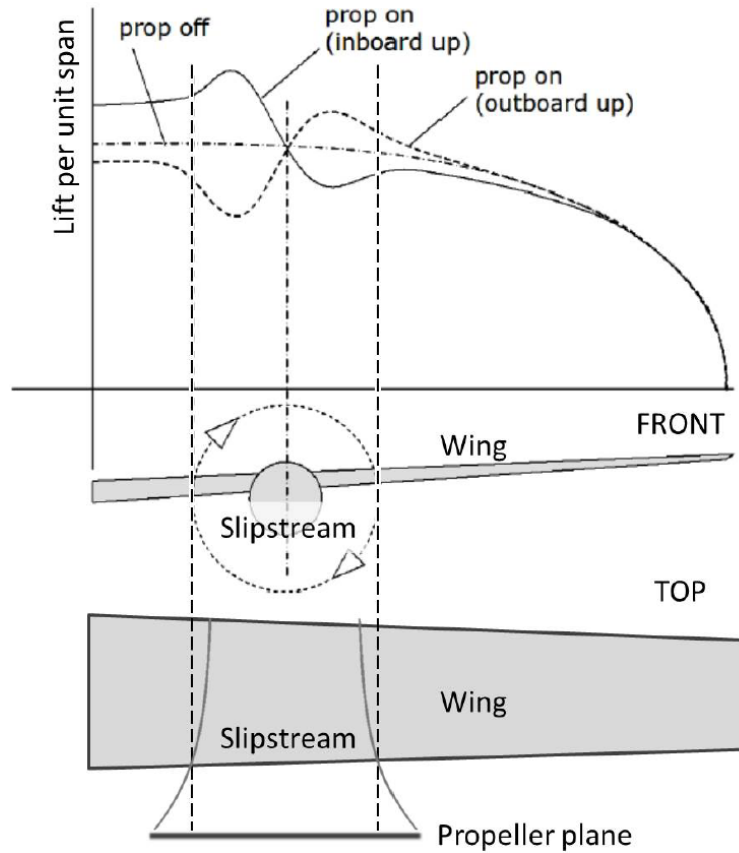


Figure 2.6: Influence areas of the propeller wing interaction varies with propeller spin direction (Velduis, 2004)

The swirl velocity in the propeller slipstream generates an induced angle of attack on the wing. Considering the example shown in Figure 2.6, the inboard wing experiences a higher angle of attack induced by the up-wash of the propeller wake. This increases the wing loading and sectional lift coefficient for this wing region. Conversely, the outboard wing

region experiences a reduced angle of attack from the down-wash of the propeller wake. This wing region experiences lower wing loading and a reduced sectional lift coefficient. This change in angle of attack is enhanced by the increased dynamic pressure in the propeller wake. In the case of the inboard wing region, the wing loading is increased further whereas the increased dynamic pressure serves to reduce the induced angle of attack on the outboard wing region. These effects can extend past the propeller diameter and deform a large part of the wing distribution.

Numerous numerical methods have been developed to estimate the effect of propeller slipstream on the wing. Franke & Weinig (1939) were one of the first to model the rotational velocity and its effect on the wing lift distribution. His analytical method used lifting line theory to account for the increased dynamic pressure and change in flow angle. Kleinstein & Liue (1972) built upon these results, integrating non-uniformities due to sectional characteristics of propeller in the slipstream. His results showed that lifting line theory alone was too coarse to predict the flow characteristics and would overestimate total wing lift. More recently Veldhuis (2004) conducted a comprehensive study into propeller location with respect to the wing and its effect on wing performance. Veldhuis formalised the difference between Single Interaction Mode (SIM) and Full Interaction Mode (FIM). He concluded that an accurate representation of propeller wing interaction can only be achieved through FIM. A number of vortex lattice method (VLM) programs coupled with blade element method (BEM) codes have been presented as SIM methods for fast estimations of propeller-wing interaction. Ferraro et al (2014) used a Truckenbrodt 3D lifting surface method coupled with VLM and BEM programs to predict propeller-wing effects for early design. Ferraro found that this method overestimated wing performance but provided a good estimate for preliminary design due to its low computational costs. Cole (2016) developed a higher-order free-wake (HOFW) method to accurately model the highly unstable propeller wake. This method used higher order vorticity elements to model propeller and wing geometries, allowing for more numerically stable wake models. When compared to full RANS CFD results, the HOFW method is accurate to within 6%.

The propeller experiences the greatest effect from the wing when parallel to the wing span.

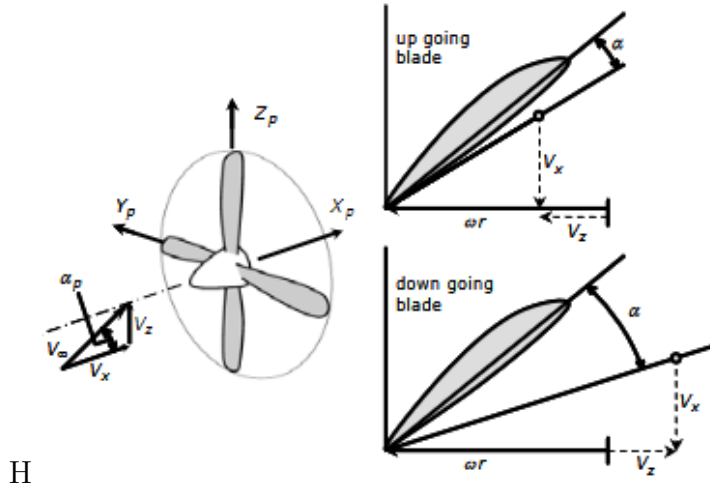


Figure 2.7: Induced angle of attack on propeller blade by leading edge upwash (Veldhuis, 2004)

This occurs in two instances, with the blade pointing directly inboard and outboard. The upwash generated by the leading edge of the wing induces an altered angle of attack on the propeller blade. As shown in Figure 2.7 the up-going blade will experience a reduced angle of attack whereas the down-going blade experiences an increased angle of attack.

Wind tunnel studies have observed that the total rotational velocity of the propeller wake reduces with the presence of a wing (Witkowski et al, 2012 and Johnson et al, 1991). The reduction of the rotational velocity has shown to increase propulsive efficiency by up to 6 % (Kroo, 1986). The degree to which swirl relaxation occurs depends on propeller position, wing loading and free stream conditions (Veldhuis, 2004). More recently Veldhuis simulated these effects with high fidelity CFD (Veldhuis et al, 2016). This numerical study suggested that the reduction in rotational flow velocity was due to the reduction in helix angle as opposed to viscous effects from the wing surface.

2.3.2 Low Reynolds Numbers

A number of wind tunnel studies have suggested that the propeller-on-wing at low Reynolds numbers improves the performance of the wing at high angles of attack. Null et al (2005) studied the effect of a tractor mounted propeller on low aspect ratio ($AR \leq 2$) MAV wings. The experiment found that from Re 50,000 to 100,000, the propeller slipstream delayed

separation due to the increased dynamic pressure. These results were later confirmed by Sudhakar et al (2013) who visualised the delay in separation. Ananda and colleagues studied both tractor and pusher configurations in a series of wind tunnel studies (Ananda et al, 2018). These found that considerable increases in lift can be found for a wing in tractor configuration from the increased dynamic pressure behind the propeller. Oil flow visualisations highlighted how the propeller slip stream induces early transition to turbulent flow and reduces the size of LSBs as shown in Figure 2.8. This resulted in a reduction in pressure drag and increase in lift-to-drag ratio (up to 70% increase compared to clean wing). The performance benefits were not found for the pusher configuration. The results of Ananda and colleagues results suggest that performance benefits from tractor propeller configurations are more significant at lower Reynolds numbers compared to high Reynolds number (greater than 100,000). This is because the propeller slipstream diminishes the negative effect of LSBs and other low Reynolds number effects. At Reynolds numbers higher than 100,000, the propeller slipstream has been shown to reduce the overall lift to drag ratio, as shown by Null et al (2005) and Shkarayev et al (2008). Although the propeller increases the local lift, it also increases drag. The net result is a 20-40% decrease in lift-to-drag ratio, depending on configuration (Null et al, 2005). Thipyopas & Moschetta (2006) also found up to a 50% reduction in maximum L/D with propeller slipstream.

Some investigations have also been made on the wing influence on propeller at low Reynolds numbers. Chen & Hubner (2021) investigated wing-on-rotor effects at low Reynolds number and disk loading. Chen & Hubner modelled the rotor effect with a wing perpendicular to the rotor thrust, simulating vertical take off and landing (VTOL) UAVs. The results suggest that the rotor thrust increases as the distance between rotor and wing decreases.

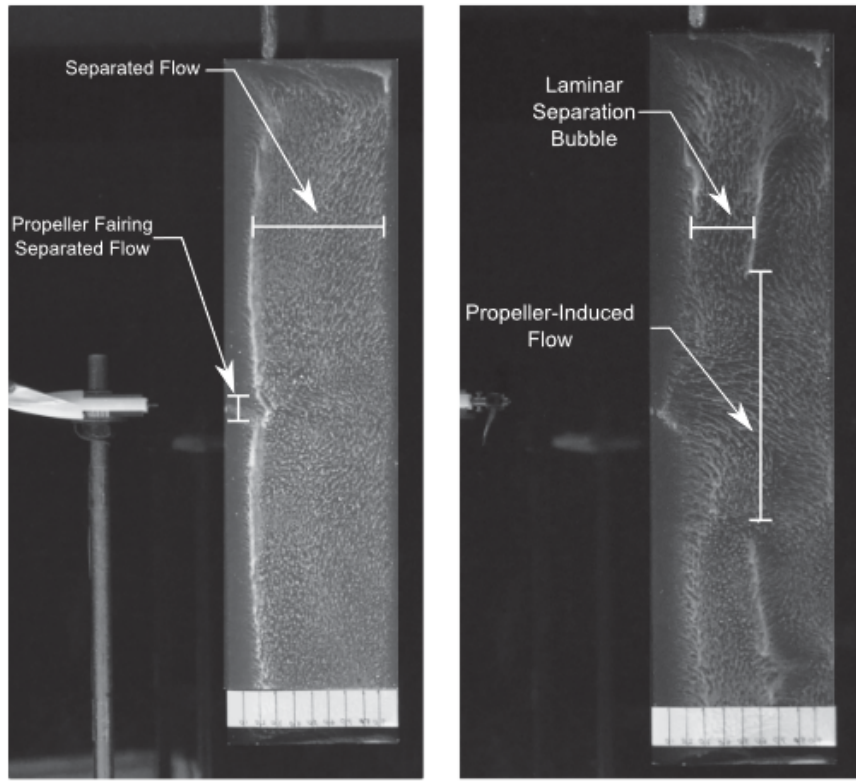


Figure 2.8: The difference in flow behaviour can be seen with propeller turned off on left and on in the right image. At 9 degrees angle of attack the flow is almost fully separated with propeller disabled. With the tractor propeller turned on the slipstream maintains attachment until the trailing edge. Outside of the slipstream the flow reattaches forming a laminar separation bubble (Ananda et al, 2018)

2.3.3 Stability Effects of Propeller Slipstream

As the wing and tail lift distributions are deformed by the propeller slipstream, the static longitudinal and lateral stability will inevitably be affected. Experimental studies have concluded that the inclusion of a tractor propeller decreases the longitudinal stability (Shams et al, 2020). The propeller slipstream increases the local lift near the wing root, shifting the aerodynamic centre forward. Furthermore, Shams et al. found that increasing the propeller diameter and RPM increased the pitching moment further (decreasing longitudinal stability), as shown in Figure 2.9.

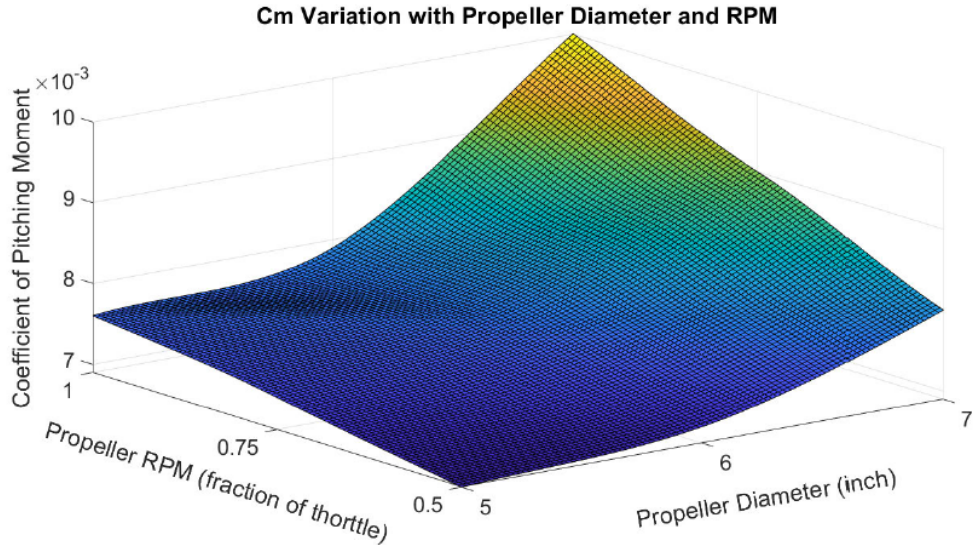


Figure 2.9: Variation of pitching moment with propeller size and rpm (Shams et al, 2020)

The reduction of pitch stiffness with propeller wash is due to an increase in main wing lift curve slope $C_{L\alpha}$ and forward shift of the aerodynamic centre (Shams et al, 2020). The size of the propeller slipstream effect on longitudinal stability varies between studies. Null et al(2005) found a 0.016 rad^{-1} increase in $C_{L\alpha}$, Chinwicharnam & Thipyopas (2016) found a 0.023 rad^{-1} increase and Thipyopas & Moschetta (2006) found an increase of 0.08 rad^{-1} , all from experimental wind testing on MAVs. The propeller has also been found to affect lateral and directional stability to a lesser degree. Shams et al (2020) found an increase in rolling and small increase in yaw moment from a tractor propeller. Again these changes were maximised by increasing propeller RPM and diameter. The propeller RPM also applies other non-aerodynamic forces to the aircraft. The two primary examples of this are the propeller torque effect, causing asymmetric roll instability based on propeller rotation direction, and gyroscopic precessional motion.

2.4 MAV Optimisation

MAV design using multi-objective optimisation algorithms has become popular, due to the multi-disciplinary requirements of MAV design. For this method, performance prediction that is accurate and computationally fast is the main challenge (Bronz et al, 2009). Trips

(2010) developed an quasi-3D aerodynamic solver with viscous corrections and low Reynolds number approximations provided by Xfoil. This purpose built solver was integrated to a sequential quadratic optimisation program and was used to design a long endurance Mini-UAV ($\text{Re} < 2.5 \times 10^5$). The final design had a lift-to-drag ratio of 11.8 (Trips, 2010). Bronz et al (2009) used a vortex lattice method with viscous corrections to create a multidisciplinary optimisation program. This was used to design multiple highly optimised micro and mini UAV designs. One design, *Eternity* shown in Figure 2.10, powered by a hybrid solar engine, had a maximum range of 200 km (Bronz et al, 2009). Hassanalian et al (2014) presented a comprehensive structure for rapid MAV design. This process involved some late stage optimisation using XFLR5, a viscous coupled VLM solver. The optimised MAV developed by Hassanalian featured a L/D ratio of 10.8 with a wingspan of 43.2 cm. Finally, Xue & Zhou (2020) used a genetic algorithm and Kriging surrogate model to optimise the propeller slipstream across a propeller-wing system for higher wing lift-to-drag ratios. The results, using RANS CFD, suggest that slipstreams with more axial velocity near the propeller hub were more desirable. By optimising the slipstream velocity distribution, an 18% increase in lift-to-drag ratio could be achieved (Xue & Zhou, 2020).

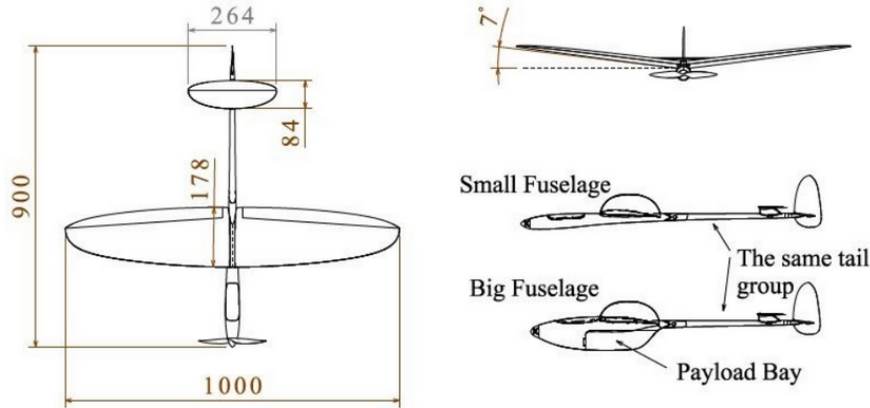


Figure 2.10: The long range Mini-UAV *Eternity* with two fuselage configurations (Bronz et al, 2009)

Chapter 3

Theory and Methodology

This thesis involves the integration of multiple complex programs. Figure 3.1 highlights the macro structure of the optimisation process. This chapter outlines the theory and methodology for each of these systems within the optimisation loop.

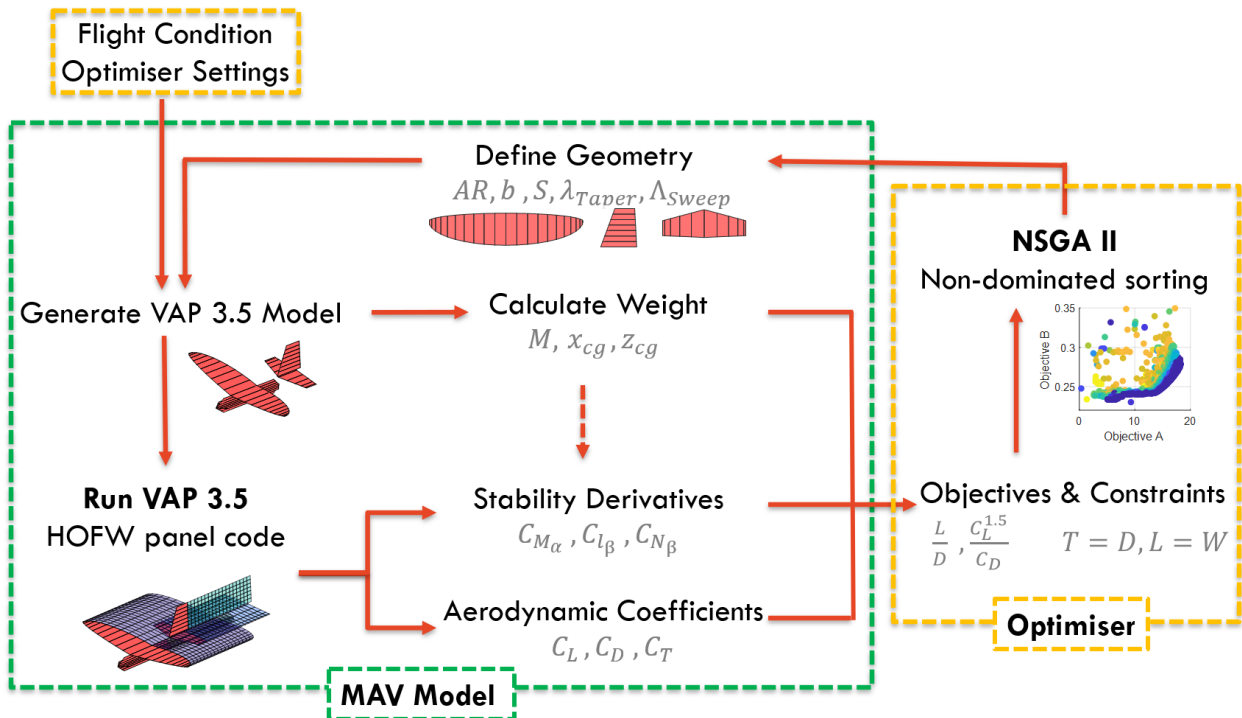


Figure 3.1: Optimisation structure including evaluation in VAP 3.5 and objective handling with NSGA-II

After the flight conditions and optimiser settings are defined, the optimiser generates an initial population of MAV geometries and the optimisation loop begins. A potential flow method, VAP 3.5, is used to calculate the aerodynamic performance of MAV designs (Sec 3.1). The weight and CG location is estimated from the MAV geometry (Sec 3.2). Using the CG location and lift distribution calculated from the potential flow method, the stability

derivatives are numerically estimated using a novel function (Sec 3.3). These stability derivatives, as well the aircraft mass and aerodynamic performance are passed into a genetic algorithm (NSGA-II) and converted into objectives and constraints. The NSGA-II performs non-dominated sorting based on predefined objectives and constraints (Sec 3.4). A new population of MAV designs is created by mutating the best performing designs in the previous iteration. These designs are defined based geometric parameters which are handled as optimisation variables. The new population of MAV is evaluated and the loop continues until highly optimised MAV designs are found.

3.1 High-Order Free Wake Method

The Higher-Order Free Wake (HOFW) method was first developed by Bramesfeld (2006) to meet the need for a fast and accurate potential flow solver for propeller-wing interaction. This method uses elements with a distributed vorticity, reducing the number of required elements and increasing the numerical stability with a relaxed wake model. The numerical robustness of the method with unsteady wake models makes this solver suitable for the highly unsteady aerodynamics of propeller wing interaction. The reduced panel density required also reduces the computation time, whilst maintaining accurate force prediction. This section will briefly outline the theory behind the HOFW method before discussing the HOFW program used, VAP 3.5. Finally, the time dependency of the unsteady propeller-wing interaction modelling will be discussed.

First order vortex lattice methods use elements with a constant vorticity across each element edge. This means that many elements are required to model non-linear lift distributions and to accurately predict aerodynamic forces. Although these methods can be very accurate, they often require long computation times, especially when unsteady and relaxed wake models are included. The HOFW method uses a non-linear vorticity distribution across streamwise and transverse edges of the Distributed Vortex Element (DVE). The streamwise (ζ axis) vorticity varies linearly and the transverse (ξ axis) vorticity is distributed using a quadratic function, as shown in Figure 3.2. This allows complex vorticity distributions to be modelled with very few DVEs, a simple example of this is shown in Figure 3.3.

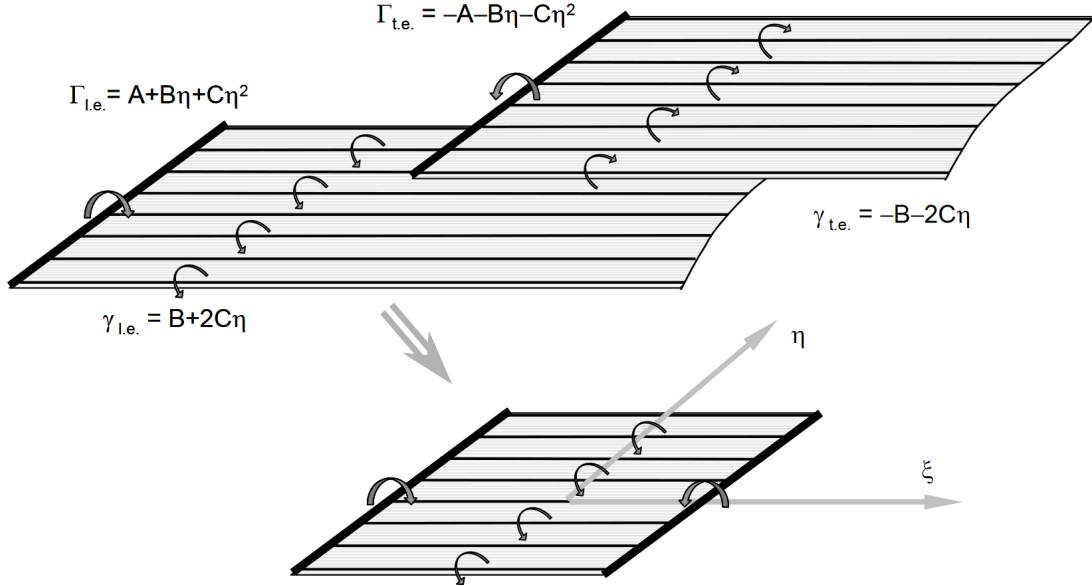


Figure 3.2: Higher-order vorticity distribution across the DVE streamwise and transverse directions (Cole, 2016)

The vorticity of the leading and trailing edge of the DVE are equal and opposite to meet the irrotationality boundary condition. Using these vortex-ring singularities, the induced vorticity at any point can be analytically calculated. The wake shape is calculated from a time stepping method. Each time step, a row of wake DVEs are produced from the trailing edge. The vorticity of these DVEs depends on the vorticity at the trailing edge. The free wake model displaces the wake DVEs based on the induced velocities from the freestream and other DVEs. Consequently, the trailing free wake aligns with the free stream and interacts with other wakes and DVE bodies (such as propeller wake on wing DVEs) as shown in Figure 3.4.

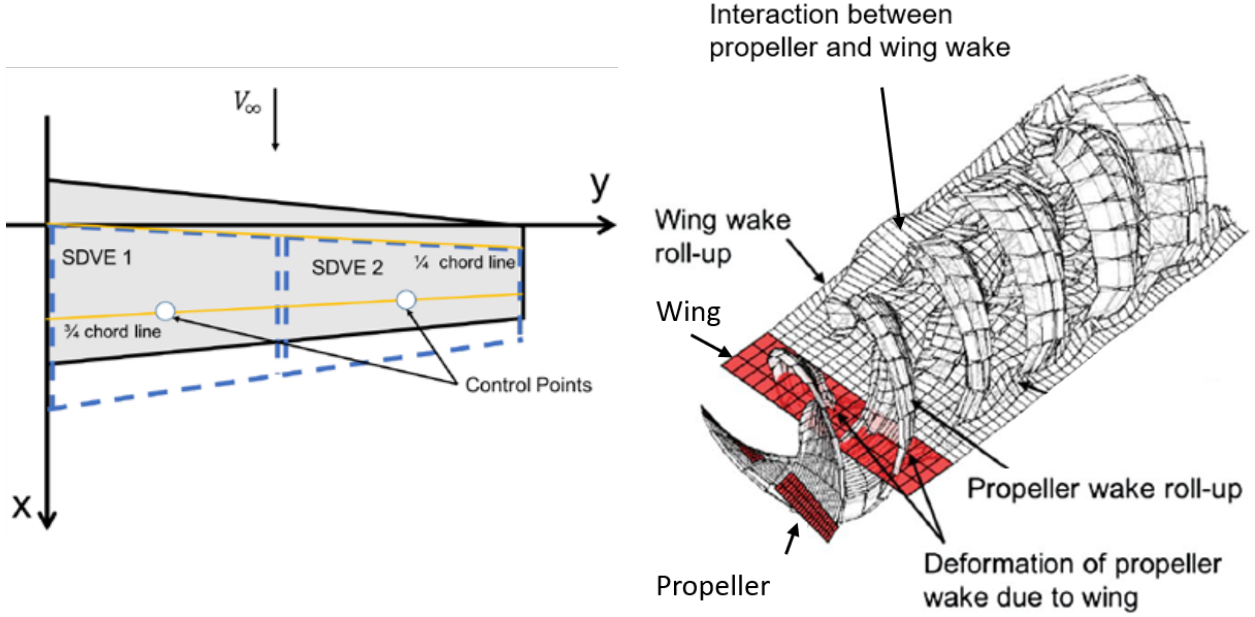


Figure 3.3: Discretisation of rectangular wing into two DVEs (Cole, 2016)

Figure 3.4: Example of wake relaxation in a propeller-wing system (Cole et al, 2019)

The HOFW method calculates aerodynamic forces based off the free stream and induced velocities. For a wing with $m \times n$ DVEs, the total kinematic normal force from the freestream V_∞ can be calculated as a function of vorticity Γ and position (in ξ and η axes), as shown in Equation 3.1 (Bramsfeld, 2006).

$$\bar{F}_k = \rho \sum_{i=1}^m \sum_{j=1}^n \left[\int_{-\eta_{i,j}}^{\eta_{i,j}} |\bar{V}_\infty \times \hat{s}| (\Gamma_{i,j} - \Gamma_{i-1,j}) d\eta + \int_{-\eta_{i,j}}^{\tau_{i,j}} \frac{\partial \Gamma(\xi, \eta, t)}{\partial t} (2\xi_{i,j}) d\eta \right] \left(\frac{V_\infty \times \hat{s}}{|\bar{V}_\infty \times \hat{s}|} \right) \quad (3.1)$$

Where \hat{s} is the unit vector along the leading edge bound vortex of the DVE. The total kinematic normal force due to the induced velocities V_{ind} from DVEs is expressed in Equation 3.2 (Bramsfeld, 2006).

$$\bar{F}_{ind} = \rho \sum_{i=1}^m \sum_{j=1}^n \int_{-\eta_{i,j}}^{\eta_{i,j}} |\bar{V}_{ind} \times \hat{s}| (\Gamma_{i,j} - \Gamma_{i-1,j}) d\eta \cdot \left(\frac{\bar{V}_{ind} \times \hat{s}}{|\bar{V}_{ind} \times \hat{s}|} \right) \cdot \left(\frac{\bar{V}_\infty \times \hat{s}}{|\bar{V}_\infty \times \hat{s}|} \right) \quad (3.2)$$

The total kinematic aerodynamic normal force is the sum of Equations 3.1 and 3.2.

$$\bar{F} = \bar{F}_k + \bar{F}_{ind} \quad (3.3)$$

The projection of \bar{F} in the x_a axis accounts for the lift-induced drag. Additional viscous corrections are required to estimate profile drag.

3.1.1 VAP 3

VAP 3 is an open source potential flow code created by Cole (2016). VAP 3.5 is the latest version, released in June 2019. It uses the HOFW potential flow method described above, adding viscous corrections using Xfoil data. Xfoil is a 2D viscous solver developed by Drela (1989). Xfoil calculates the boundary layer thickness and estimates viscous drag. VAP also uses the 2D Xfoil data to predict airfoil stall. If C_L exceeds $C_{L_{max,2D}}$ for a given DVE panel, VAP multiplies the local lift by 0.825 to estimate the performance reduction due to airfoil stall. This is by no means an accurate method for simulating stall. However, for use in the optimiser loop, it effectively penalises designs which exceed the stall limit of the airfoil. VAP also features various visualisation and analysis tools, such as fixed-lift analysis, gust disturbance modelling and GIF generation. However, VAP includes no stability derivative calculation. VAP takes a .xml file input which includes all geometric parameters and condition settings. A summary of these input settings are supplied in Appendix B.

3.1.2 Time Dependence of Propeller-Wing Interaction

As discussed above the propeller wake DVEs influence the wing and wing wake DVEs downstream. With the propeller rotation, DVE wake rows are shed in a spiral helical shape as shown in Figure 3.4. Due to this shape, the wing and empennage structure experience a variable influence from the propeller wake depending on the propeller position. This means the propeller-wing interaction is highly time dependant. This time dependency is shown by Cole (2016), modelling the propeller-wing interaction experiment of Dunsby et al. (1959), as shown in Figure 3.5.

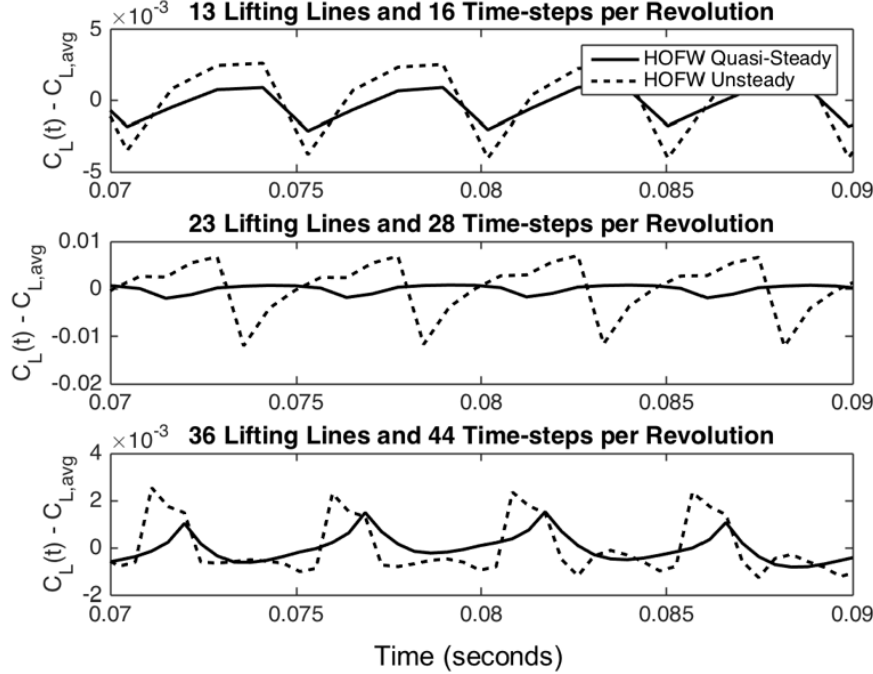


Figure 3.5: Comparison between time accurate and time averaged lift predictions for varying panel densities and timesteps (Cole, 2016)

Figure 3.5 shows how the lift coefficient C_{L_t} oscillates around the time averaged lift coefficient $C_{L_{avg}}$ at the propeller RPM frequency. The quasi-steady solver predicted smaller oscillations compared to the full unsteady solver, as expected. Decreasing the time step increases the oscillation resolution but does not affect the oscillation magnitude. This time dependence means that time the number of iterations and time steps need to be carefully selected to give accurate results for propeller-wing interaction, as discussed in Section 4.5.

3.2 Mass Calculation

The MAV mass is calculated based off a balsa surface and foam core model as outlined in Hassanalian et al (2018). This model is altered to incorporate a variable powerplant and electrical weight to model different size classes of UAVs. The total weight of the MAV is the sum of structural, powerplant and electrical weights as shown in Equation 3.4.

$$m_{total} = m_{str} + m_{power} + m_{electrical} \quad (3.4)$$

This section will briefly outline the primary relationships used to estimate MAV weight. The wing weight was calculated based off wing area, shown in Equation 3.5

$$m_{wing} = S(\rho_{foam}t_{mac} + 2\rho_{balsa}t_{skin}) \quad (3.5)$$

Where t_{mac} is the airfoil thickness at the mean aerodynamic chord and ρ is the material density. Both the horizontal and vertical tail mass were calculated similarly, shown in Equations 3.6 and 3.7.

$$m_{VT} = \frac{S_{VT}}{S} m_{wing} \quad (3.6)$$

$$m_{HT} = \frac{S_{HT}}{S} m_{wing} \quad (3.7)$$

Where S is the wing area, S_{HT} is the horizontal tail area and S_{VT} is the vertical tail area. The fuselage mass was calculated based on a cylindrical outer balsa structure with an inner reinforcing structure as shown in Equation 3.8.

$$m_{fuse} = \rho_{balsa}t_{skin}(2h_{fuse}(l_{fuse} + w_{fuse}) + l_{fuse}w_{fuse}) \quad (3.8)$$

Where h_{fuse} , l_{fuse} and w_{fuse} are the height, length and width of the fuselage structure. The wing, fuselage and empennage weights form the structural weight of the aircraft.

$$m_{str} = m_{wing} + m_{VT} + m_{HT} + m_{fuse} \quad (3.9)$$

The powerplant and electrical masses for both MAV classes were estimated based on MAV models of a similar size from literature. The 30 cm class electrical and powerplant mass was taken from Van Magil (2016) with a total mass of 80 grams, shown in Table 3.1. The larger 45 cm class electrical and powerplant weight was taken from Hassanalian & Adbelkefi (2017) shown in Table 3.2, featuring a total mass of 225 grams. For the 7 inch propeller optimisation of the 45 cm class, the weight is increased by 3 grams.

Table 3.1: Powerplant and electrical mass breakdown for 30 cm class MAV

| Component | Mass [g] |
|---------------------------|----------------|
| Flight Control | |
| Pixfalcon Autopilot | 7.91 |
| Mini PX GPS Module | 5.3 |
| ORX Satellite Receiver | 2.3 |
| 3DR 915MHz Telemetry | 2.65 |
| Propulsion | |
| ESC (DYS Opto BLHeli) | 5.45 |
| Propeller (GWS 4x4) | 1.3 |
| Turnigy 1811 - 2000 kV | 10.5 |
| Actuation | |
| Micro Digital Servos | 5.7 |
| Power | |
| 7.4V 490mah Lipo Battery | 28.25 |
| Wiring | 6 |
| Matek 5v Switch mode reg. | 1 |
| Extra | |
| TOTAL | 80.36 g |

Table 3.2: Powerplant and electrical weight breakdown for 45 cm class MAV

| Component | Mass [g] |
|-----------------------|----------------|
| Flight Control | |
| Speed Controller | 22.8 |
| GPS air | 17 |
| Autopilot board | 12 |
| Reciever | 8 |
| IR Sensor | 4 |
| Drop Sensor | 2 |
| Propulsion | |
| Motor | 39 |
| Propeller (GWS 5x4.3) | 6 |
| Actuation | |
| Servo Motors | 13 |
| Power | |
| Battery | 90 |
| Wiring | 6 |
| Extra | |
| TOTAL | 224.8 g |

3.3 Stability Calculation

A novel numerical stability analysis function has been developed to estimate the lateral and longitudinal stability characteristics of optimised UAV designs. The stability derivatives were calculated around the stability axes. The function summed the contribution of the

DVE normal force to the pitching M , yawing n and rolling l moments. The contribution of the viscous correction drag vector and moment about the quarter chord, both from an Xfoil data lookup, were also included. The contribution of the $m \times n$ main wing DVEs to the pitching moment is shown below as an example.

$$M_{wing} = Q_\infty \sum_{i=1}^m \sum_{j=1}^n A_{i,j} (M_{aci,j} \cos \phi_{i,j} \bar{c} + C_{N_{i,j}} \sin \theta_{i,j} \cos \phi_{i,j} (d_x \sin \alpha + d_z \cos \alpha) + C_{Dv_{i,j}} (d_x \sin \alpha + d_z \cos \alpha))$$

Where M_{ac} is the moment about the airfoil quarter chord and C_{Dv} is the viscous drag correction (C_{Di} component is included in C_N) . The distances from the panel aerodynamic centre to aircraft centre of gravity are denoted by d_x and d_z , in the stability axis reference frame. The angles $\phi_{i,j}$ and $\theta_{i,j}$ represent the DVE roll and pitch angles with respect to the stability axes. For more information on the coordinate axis and angle definitions refer to Appendix A.1. For more details on the longitudinal and lateral stability derivatives and criteria, refer to Appendix A.4 and A.5. The moment coefficients about each of the three axes were found by normalising the moment force by the dynamic pressure and characteristic length as shown in Equations 3.10 to 3.12.

$$C_M = \frac{M_{wing} + M_{HT} + M_{VT} + M_{fuselage}}{\frac{1}{2} \rho V_\infty^2 S \bar{c}} \quad (3.10)$$

$$C_n = \frac{N_{wing} + N_{HT} + N_{VT} + N_{fuselage}}{\frac{1}{2} \rho V_\infty^2 S b} \quad (3.11)$$

$$C_l = \frac{l_{wing} + l_{HT} + l_{VT} + l_{fuselage}}{\frac{1}{2} \rho V_\infty^2 S b} \quad (3.12)$$

The stability function calculated these moment coefficients at two angles of attack (α_i and α_{i+1}) and sideslip angles (β_i and β_{i+1}). The stability derivatives were then estimated numerically as shown in Equations 3.13 to 3.15

$$C_{M_\alpha}(\alpha_i) = \frac{C_M(\alpha_i) - C_M(\alpha_{i+1})}{\alpha_i - \alpha_{i+1}} \quad (3.13)$$

$$C_{n_\beta}(\beta_i) = \frac{C_n(\beta_i) - C_n(\beta_{i+1})}{\beta_i - \beta_{i+1}} \quad (3.14)$$

$$C_{l_\beta}(\beta_i) = \frac{C_l(\beta_i) - C_l(\beta_{i+1})}{\beta_i - \beta_{i+1}} \quad (3.15)$$

A difference in angle of one degree was chosen to avoid inaccuracies caused by local high frequency variation in moment across α/β . The stability function is inaccurate at high angles of attack due to a low fidelity airfoil stall model. The stall model used in VAP 3.5 is mainly to detect when airfoils exceed $C_{L_{max}}$ rather than to accurately model of partial or fully separated flow. For this reason the second angle $\alpha_{i+1}, \beta_{i+1}$ was chosen to be lower than the first α_i, β_i to reduce airfoil chance of reaching stall. This method assumes an airfoil aerodynamic centre at 0.25 c . For highly cambered airfoils, this assumption will lose accuracy. However, as shown in Section 4.4 the novel numerical stability derivative calculator was able to accurately estimate stability derivatives of a MAV model.

The MAV fuselage also will affect the aerodynamic performance and stability derivatives. As VAP 3.5 does not include any fuselage specific models, the MAV fuselage was modelled using two perpendicular lifting surfaces. These lifting surfaces produce wake DVEs and will also be influenced by induced velocities from the propeller wake. The fuselage design includes a vertical and a horizontal lifting surface to model forces from disturbances in both v (y_a axis) and w (z_a axis). This aerodynamic fuselage model has been shown to accurately predict fuselage influence on aerodynamic forces and moments (Kuzmina et al. 2018). For the MAV designs in this thesis, a NACA0012 airfoil was used to produce symmetric forces in y_b and z_b axes. Furthermore the 12% c max thickness will effectively model the viscous drag effect from the fuselage.

3.4 Optimiser Algorithm

A Non-dominated Sorting Genetic Algorithm (NSGA-II) was used. This algorithm mimics Darwinian natural selection to perform multi-objective optimisation. The optimiser generates progressively more optimised design populations until highly optimised designs are found. The most optimised solutions are shown in the Pareto front, as shown in Figure 3.6.

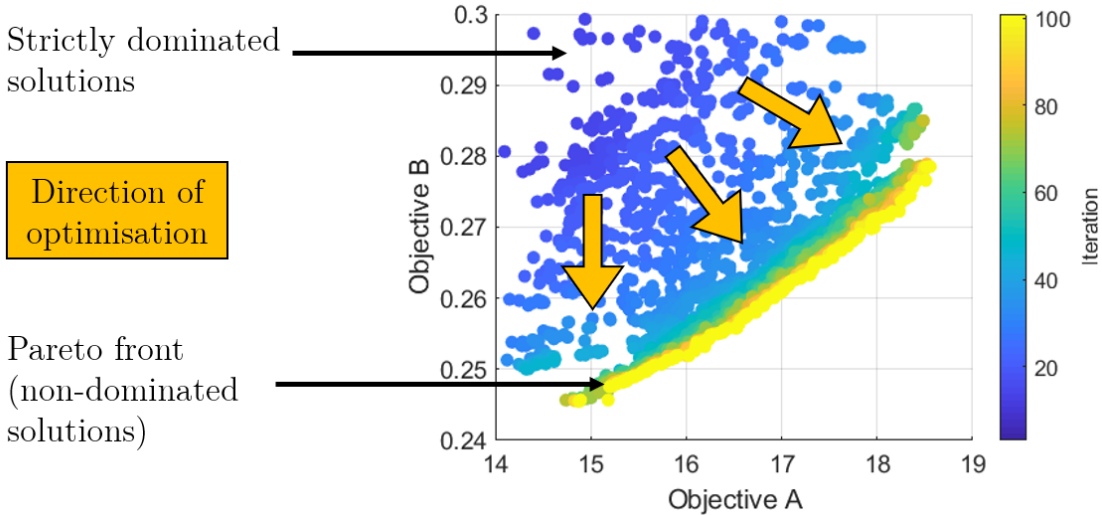


Figure 3.6: Example of dominated and non-dominated solutions (Pareto front)

The Pareto front is a selection of models that represent the non-dominated solutions of objectives A and B. This means that models in this group cannot be changed to improve one objective without decreasing another objective. The group of models behind the Pareto front are strictly dominated, meaning that another model has been created which improves one objective whilst at least keeping all other objectives constant. For each iteration of the optimiser, five key steps are performed as described below (Yosoff et al., 2011):

1. **Initialisation:** The first iteration of designs are quasi-randomly generated using a Latin Hypercube Sample (LHS) model. Using the LHS model, fewer design duplicates are generated compared to a uniform random sample, increasing the overall efficiency of the optimisation (Chen, 2016).
2. **Evaluation:** The objectives and constraints for each design in the iteration population are evaluated. For this thesis, the evaluation function uses the VAP 3 potential flow method to calculate aerodynamic performance and weight objectives. Constraints are also applied to the designs, limiting the feasible population .
3. **Non-Dominated Sorting:** The population is sorted with respect to the defined optimisation objectives. Any model that does not meet constraint criteria is considered not feasible. The population is ordered based on the level of domination compared to

other designs. All non-dominated solutions are separated and dominated designs are ordinally sorted based on the number of other designs which strictly dominate them.

4. **Crowding Distance:** All but the top performing solutions will be rejected. However, in the case where there are too few non-dominated solutions, the optimiser accepts designs from the second least dominated front. The crowding distance provides a secondary selection criterion. It measures the density of designs in the objective space. Designs with the highest crowding distance (lower density) are selected, improving the spread of the Pareto front.
5. **Mutation:** The final step is mutating the non-dominated solutions, to create optimisation progress and find the most optimal designs. The new iteration population is found by first crossing over variables between the best performing designs of the previous iteration. A random mutation is then also applied to the new population. This new population is then used in Step 2 and the cycle repeats.

A diagram of this process is shown in Figure 3.7.

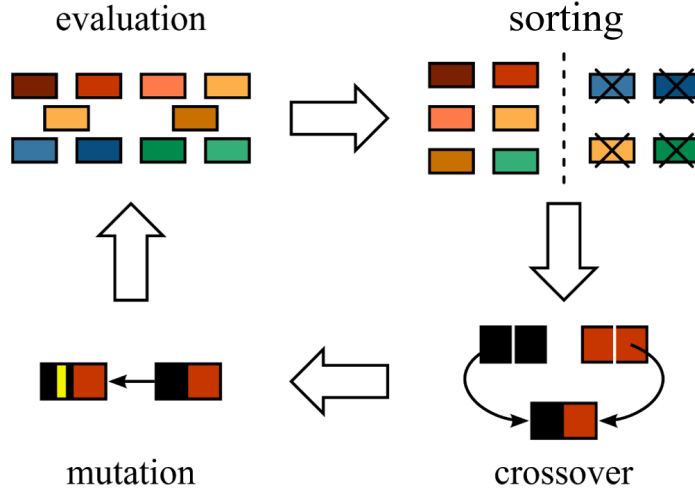


Figure 3.7: Iteration process of the NSGA-II algorithm including evaluation, sorting, crossover and mutation (Chen, 2016)

The level of optimisation depends on the maximum number of iterations and the population size for each iteration. A larger population size allows the optimiser to evaluate more designs and select for optimal designs faster. However, this comes at the cost of computational time.

Chapter 4

Validation and Calibration of VAP 3

Low Reynolds number aerodynamics can be difficult to model accurately due to complex flow phenomena as discussed earlier. A number of validation studies were completed, focused on validating VAP 3.5 in low Reynolds number conditions. A range of wing and propeller validations showed highly accurate results compared to experimental testing, as shown in Sections 4.1 and 4.2. VAP 3.5 also predicts experimental propeller-wing interaction results well, presented in Section 4.3. A validation of the novel stability function is presented in Section 4.4. Finally, in Section 4.5, a convergence study is performed to determine the most time efficient optimiser set up. The validation studies completed show that VAP 3.5 is an accurate aerodynamic solver at low Reynolds numbers.

4.1 Wing Validation

VAP 3.5 was validated against Fluent CFD results performed by Trips (2010). The validation cases consisted of rectangular wing models at a Reynolds number of 2.32×10^5 . An outline of the wing models used is presented in Table 4.1. The free stream velocity was 20 m/s and density was set to 1.225 kg/m^3 .

Table 4.1: Trips (2010) validation case wing geometries

| Case | Wing Shape | Airfoil | Root Chord | AR | Taper | Span |
|------------|-------------|---------|------------|----|-------|-------|
| WING000300 | Rectangular | S5010 | 0.17 m | 3 | 0.3 | 0.332 |
| WING000500 | Rectangular | S5010 | 0.17 m | 3 | 0.5 | 0.383 |
| WING001000 | Rectangular | S5010 | 0.17m | 3 | 1 | 0.51 |

Figures 4.1 to 4.6 show VAP 3.5 modelling of Trips (2010) validation cases. For all validation cases VAP 3.5 models the lift and drag characteristics of the tapered wings accurately. The maximum L/D ratios calculated by VAP 3.5 diverged by a maximum of 5.7 % in Figure 4.6.

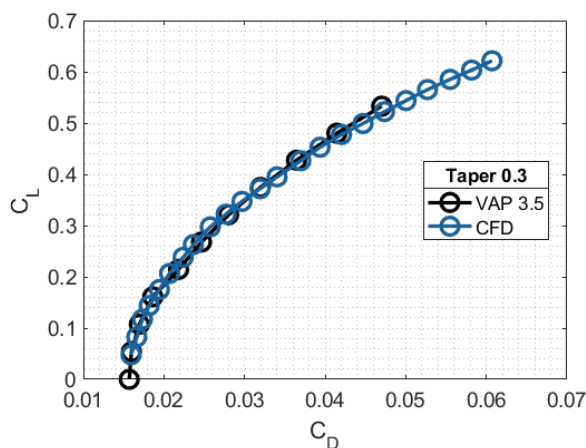


Figure 4.1: WING000300: C_L vs C_D

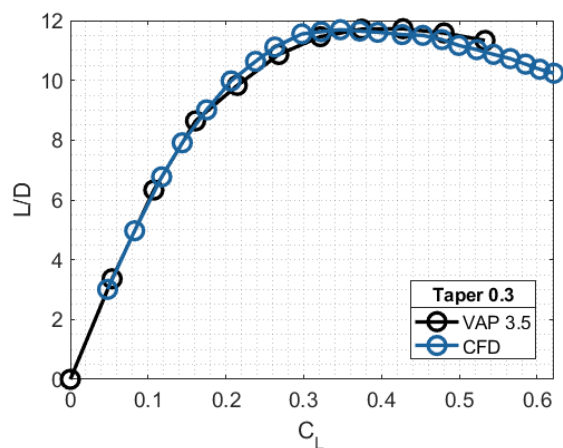


Figure 4.2: WING000300: L/D vs C_L

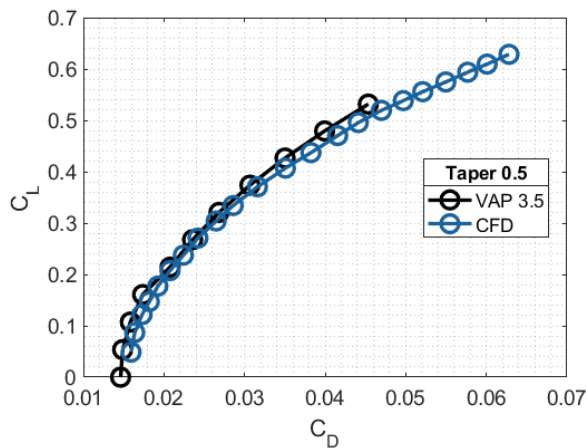


Figure 4.3: WING000500: C_L vs C_D

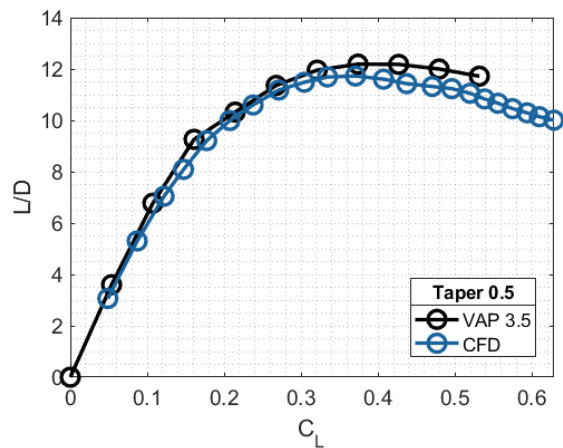


Figure 4.4: WING000500: L/D vs C_L

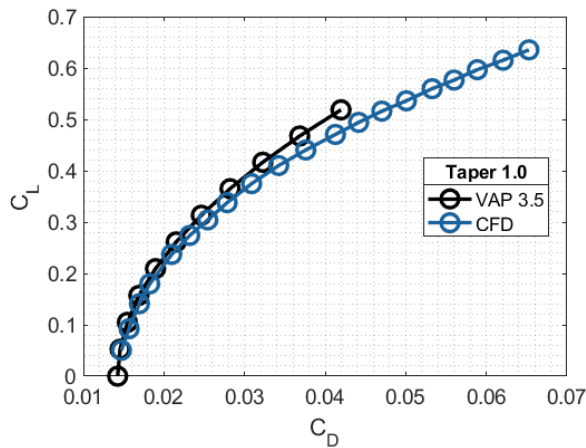


Figure 4.5: WING001000: C_L vs C_D

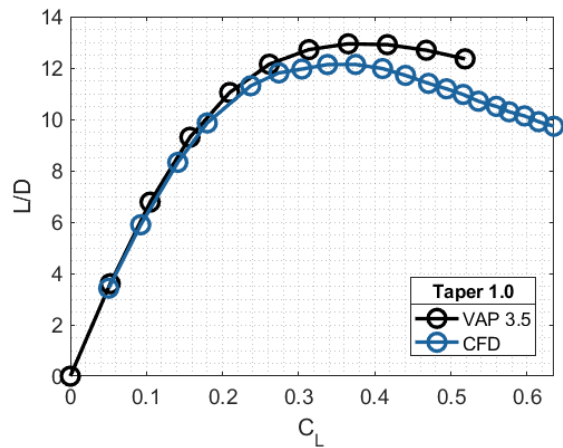


Figure 4.6: WING001000: L/D vs C_L

4.2 Propeller Validation

A number of low Reynolds number propeller validations were performed in VAP 3.5 to verify the thrust predictions used in the optimisation. Several propeller validations were performed by Coles (2016), using larger propellers at much higher Reynolds numbers. New validation studies are required to demonstrate the force prediction accuracy of VAP 3.5 at lower Reynolds numbers. Three propellers were selected based on the optimisation classes discussed in Section 5.1. The three propellers analysed were the GWS Direct Drive 4×4 (4 inch), GWS Direct Drive 5×4.3 (5 inch) and APC Sport 7×6 (7 inch), shown in Figure 4.7. The VAP 3.5 modelling of these propellers was compared against wind tunnel data from Brandt (2005) and Deters (2014). The propellers were modelled using 8 DVEs per blade, run for 40 iterations per operating point and using a timestep of 0.0005 s.

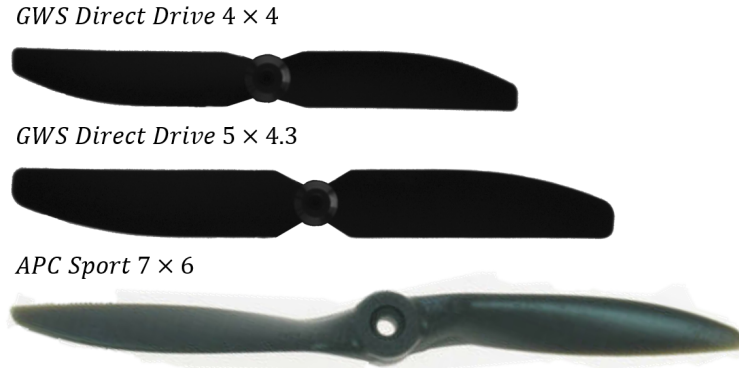


Figure 4.7: Front view of propellers used in validation study. Not to scale

Figures 4.8 to 4.13 show the VAP 3.5 performance results compared to experimental data. Overall, VAP 3.5 accurately predicts force and torque coefficients after a pitch shift adjustment was applied. For both GWS propellers a collective pitch shift of 2 degrees was applied. For the APC 7x6, a pitch shift of 4 degree was applied. For both GWS propellers, the thrust and torque measurements are highly accurate. At lower advance ratios, the APC propeller is less accurate. With the lower advance ratios, the propeller blade experiences a higher angle of attack. As discussed in Section 3.1.1, VAP becomes inaccurate near stall and hence, the divergence seen in Figure 4.12 is to be expected. With these results in mind, the optimisation will use advance ratios $0.6 > J > 1.0$.

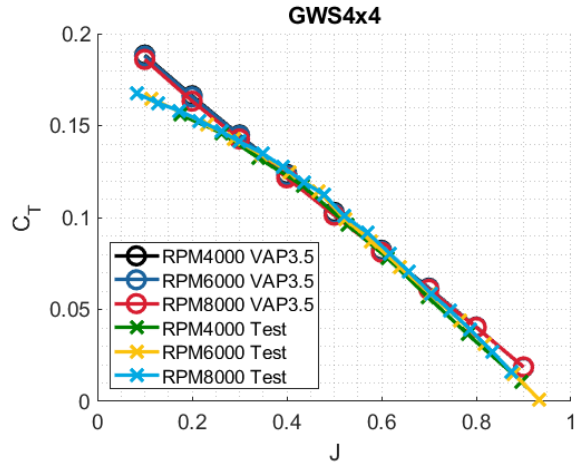


Figure 4.8: GWS4x4 Thrust Coefficient

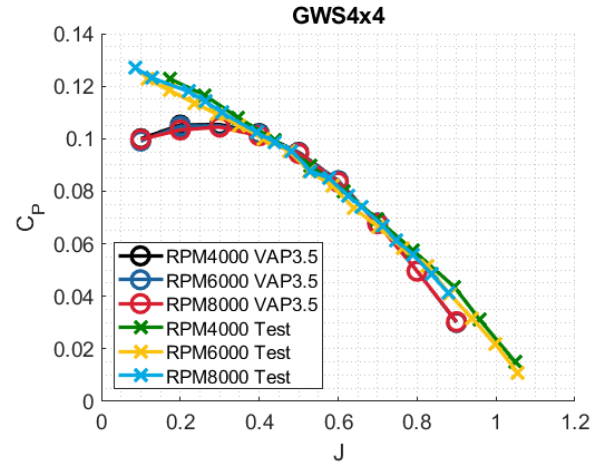


Figure 4.9: GWS4x4 Torque Coefficient

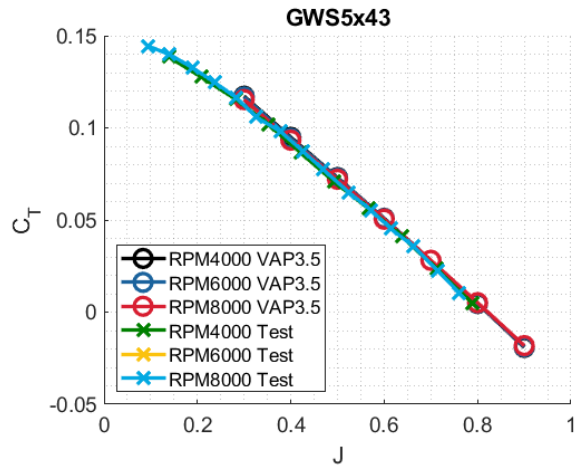


Figure 4.10: GWS5x43 Thrust Coefficient

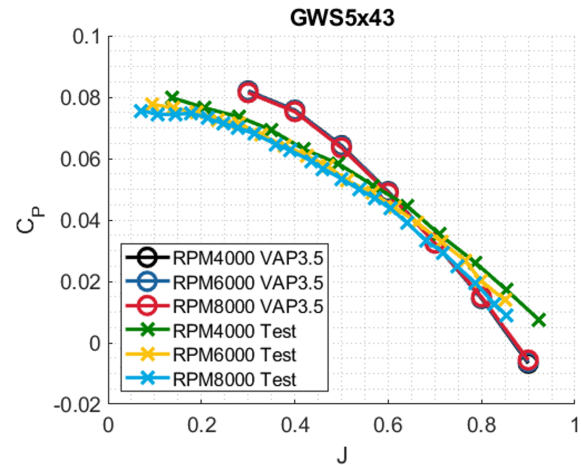


Figure 4.11: GWS5x43 Torque Coefficient

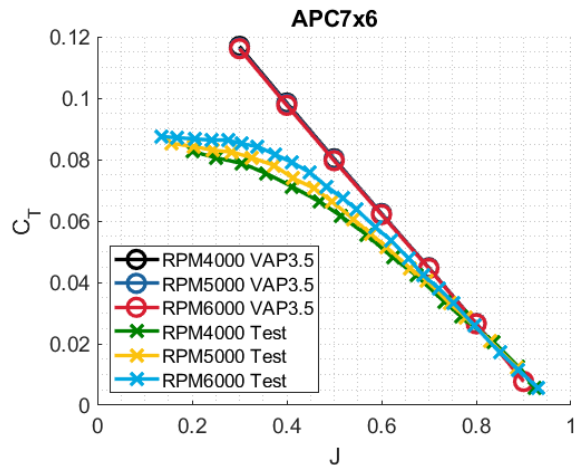


Figure 4.12: APC7x6 Thrust Coefficient

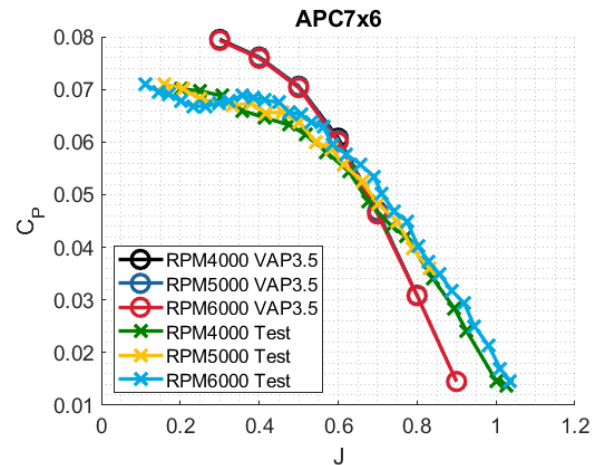


Figure 4.13: APC7x6 Torque Coefficient

4.3 Propeller-Wing Interaction

To validate the interaction between the propeller wake and wing, a propeller-wing system was modelled in VAP 3. The PROWIM (Propeller Wing Interference Model) features a rectangular wing with a half span of 0.64 m and a constant airfoil section (NACA 64₂-a015). PROWIM uses a 4 blade NACA-5868 propeller with a diameter of 0.236 m. A diagram of the PROWIM set up is shown in Figure 4.14. The free stream was 49.25 m/s with a density of 1.225 kg/m³.

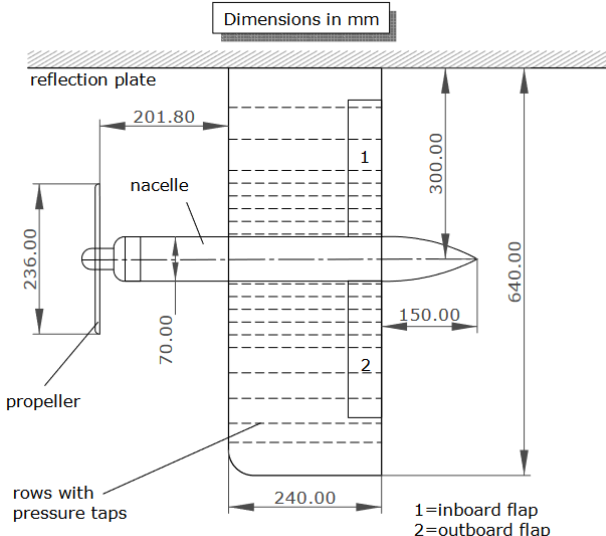


Figure 4.14: Dimensions and layout of the PROWIM model (Veldhuis, 2004)

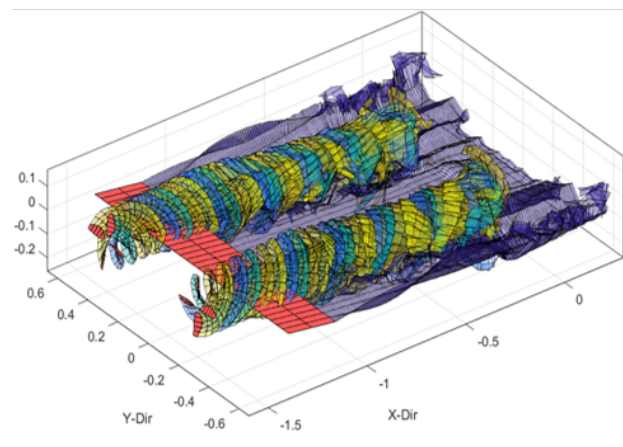


Figure 4.15: VAP model of the PROWIM system

Figure 4.16 shows the wing normal force distribution with propeller rotating inboard-up for the PROWIM model. The VAP predictions are compared against experimental wind tunnel results from Veldhuis (2004). The predicted normal force distribution from VAP matches the experimental results for all angles of attack. As expected, the inboard wing experiences a higher normal force due to the propeller up-wash. The outboard section experiences a reduced angle of attack from propeller down-wash, reducing the local normal force (Veldhuis, 2004). The VAP force prediction loses accuracy at higher angles of attack. Higher angles of attack are more challenging to model as the induced forces from propeller wash are combined with larger normal forces from the free stream.

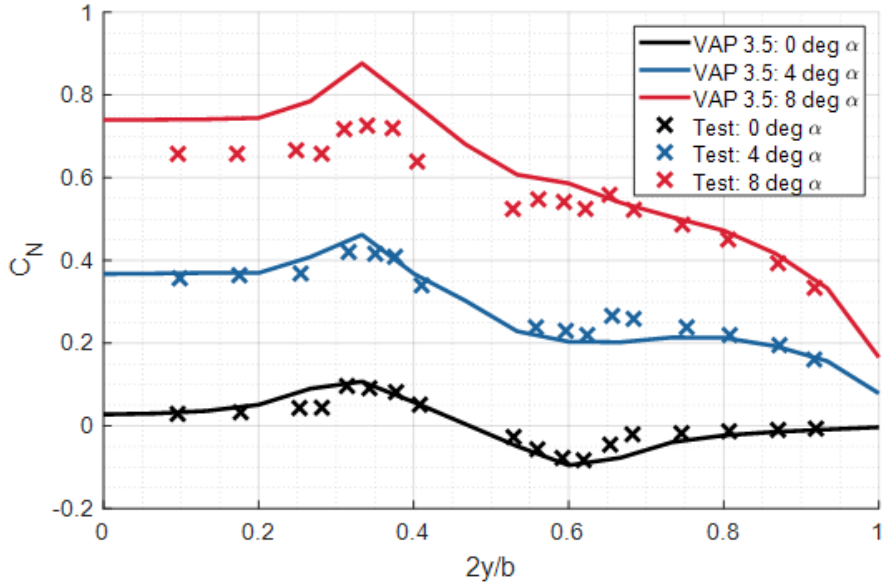


Figure 4.16: Wing normal force distribution for the PROWIM validation model

4.4 Stability Validation

The stability function was validated against numerical results from Stewart et al. (2007). This study investigated the stability of GenMAV ('Generic MAV'), a baseline MAV design used to baseline future design. GenMAV features a conventional wing and empennage configuration. A thin cambered plate airfoil is used on GenMAV. However, this was unable to be used for the VAP model because of Xfoils inaccuracy with thin airoils. Instead, an Eppler E387 airfoil was selected because of its similar camber profile to the GenMAV airfoil. A diagram of GenMAV is shown in Figures 4.17 and 4.18. Stewart et al (2007) used Athena Vortex Lattice (AVL) to numerically estimate stability derivatives and moments. The M , n and l moment predictions from VAP and Stewart et al. (2007) are presented in Figure 4.19

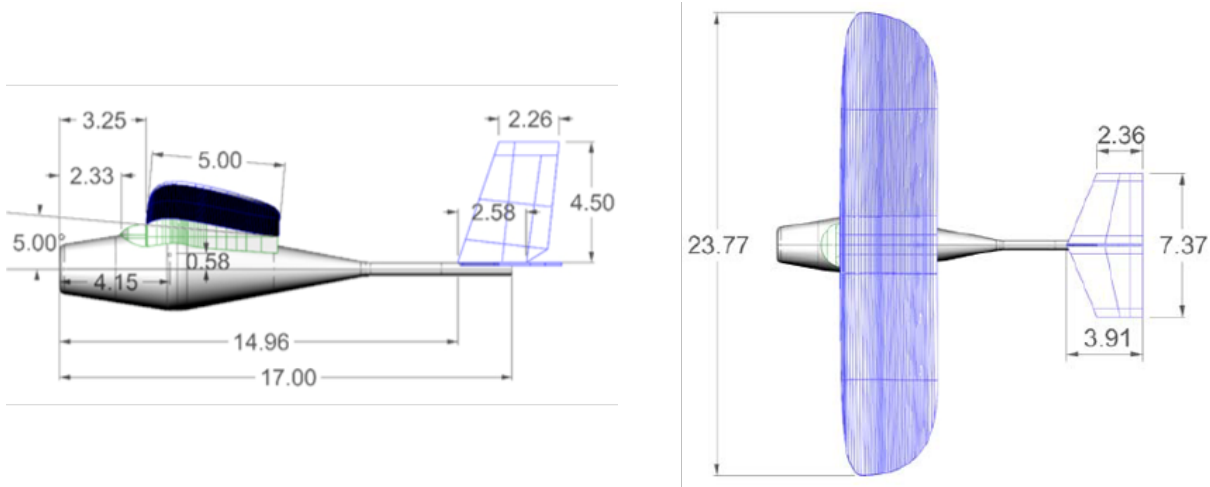


Figure 4.17: GenMAV side view. Values in inches (Stewart et al, 2007)

Figure 4.18: GenMAV top view. Values in inches (Stewart et al, 2007)

The novel stability function estimates aircraft moments accurately, as shown in Figure 4.19. When the pitching moment becomes non-linear, at negative angles of attack, the stability function becomes less accurate. These inaccuracies may be caused by inaccurate force prediction from VAP 3 or the differences in airfoil geometry. Table 4.2 shows the stability derivatives of the GenMAV model calculated from AVL and from the novel stability function.

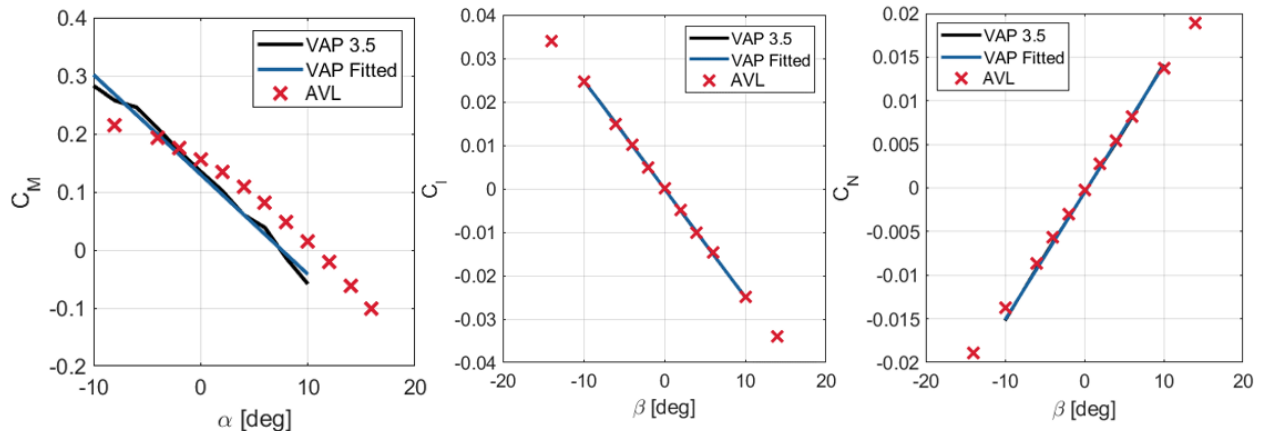


Figure 4.19: Pitch, roll and yaw moment coefficients calculated in VAP 3 compared to AVL results

Table 4.2: Stability derivative from AVL and VAP 3.5

| Source | C_{m_α} | C_{l_β} | C_{n_β} |
|---------------------|----------------|---------------|---------------|
| AVL (Stewart, 2007) | -1.45 | -0.162 | 0.287 |
| VAP 3.5 | -1.53 | -0.142 | 0.356 |
| % Difference | 5.5 | -12.0 | 24.0 |

The stability derivatives calculated using VAP 3.5 are relatively accurate compared to those from AVL. The pitch and roll derivatives C_{m_α} and C_{l_β} are accurate to within 15% of the AVL calculations while the yaw derivative C_{n_β} is less accurate. These inaccuracies are also likely due to the geometry differences between AVL and VAP models. The function is highly sensitive to CG placement and hence any inaccuracies in the VAP geometry can lead to large changes in results. Although the stability function does not replicate AVL results exactly, it is accurate enough to constrain non-feasible designs in the optimisation process.

4.5 Convergence and Time Dependency

The time dependency of propeller-wing interaction poses a challenge for this thesis as it is not feasible to run every model for four full propeller revolutions as shown above (Figure 4.15). With a large population size, the computation time would be too large for the computing power available. A method is required to determine the minimum feasible number of iterations to run each model such that stability derivative estimations converge. For the no propeller case, the stability derivatives converged quickly after 20-30 iterations as shown in Figures 4.22, 4.24 and 4.26. For simulations without propeller, convergence is not affected by varying timestep. On the other hand the stability convergence including propeller effects strongly depends on both timestep and final propeller rotation position. For the stability derivatives to converge, the normal force across all lifting surfaces needs to stabilise. As shown in Figure 4.20 the wing C_N with propeller stabilises quickly, at around 20-30 iterations. However, the tail C_N distribution convergence takes much longer, requiring at least 30-40 iterations, as shown in Figure 4.21. The required time can be reduced by increasing the timestep size. However, propeller modelling is very sensitive to timestep size

and large timesteps can quickly cause numerical instability (Cole, 2016). As recommended by Cole (2016) at least 20 iterations are required per propeller revolution (18° propeller rotation per iteration).

The stability derivative convergence including propeller is shown in Figures 4.23, 4.25 and 4.27, where red markers represent full revolutions of the propeller. From these figures it is clear that the final propeller position strongly influences on the stability derivatives. If we only consider the full revolution data points (shown in red), we see that stability derivatives converge well. It is clear that at least two full iterations are required for accurate stability derivatives. The maximum iterations and time step need to be set for exactly two propeller rotations. Runs that do not complete exactly on full revolutions experience asymmetric loading from the propeller wake DVEs, creating inaccuracies in stability derivatives. With propeller, VAP 3 is estimating a reduction of 0.048 rad^{-1} in $C_{m\alpha}$, within the range from experimental results in Null et al (2005), Chinwicharnam & Thipyopas (2016) and Thipyopas and Moschetta (2006). These differences are most likely due to differences in MAV size and configuration. The numerical stability estimation and idealised potential flow method are also expected give slightly idealised results as shown in Section 4. However, it is clear that the effect of propeller slipstream on stability derivatives is reasonable and follows trends published in literature.

The computation time increases rapidly with maximum iteration. The inclusion of propeller also significantly slows down the computation. A full 40 iteration propeller run including stability calculation takes 5 min and 42 seconds on a 6 core i5 processor. Table 4.3 shows the increase in computation time as the max iteration increases.

Table 4.3: Computation times for the stability calculations including propeller (min:sec)

| Max Iterations | 5 | 10 | 15 | 20 | 30 | 40 | 50 | 60 | 70 | 80 |
|------------------|------|------|------|------|------|------|-------|-------|-------|-------|
| Computation Time | 0:06 | 0:17 | 0:35 | 1:06 | 2:57 | 5:42 | 11:55 | 25:03 | 38:20 | 57:16 |

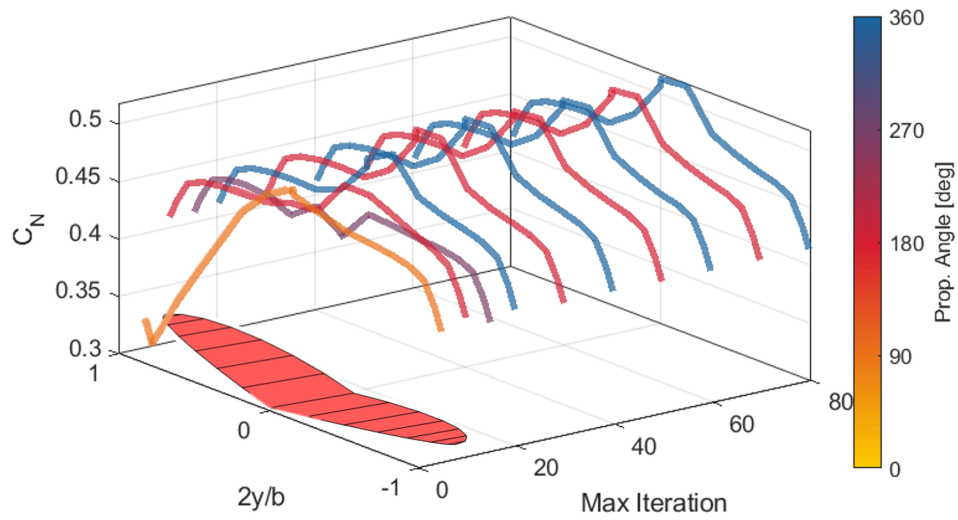


Figure 4.20: Main wing normal force convergence under the influence of propeller slipstream

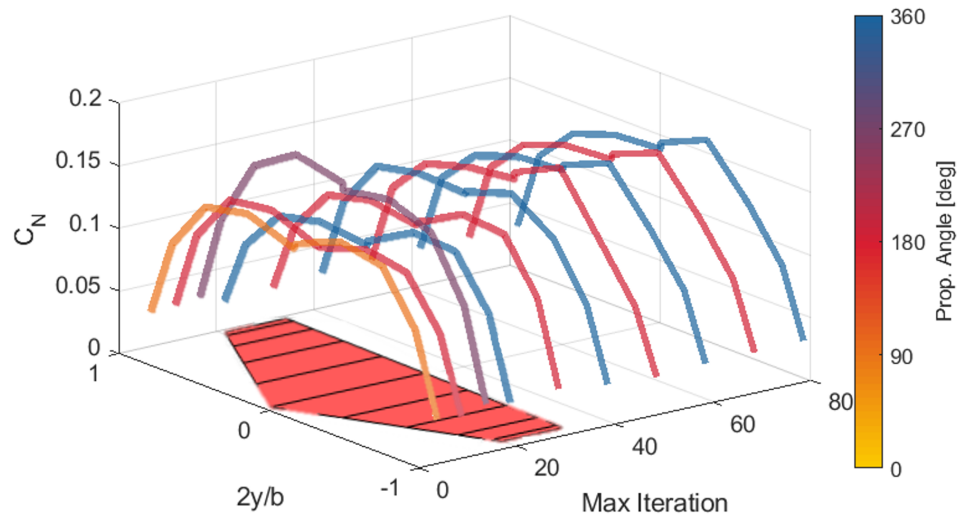


Figure 4.21: Horizontal tail normal force convergence under the influence of propeller slipstream

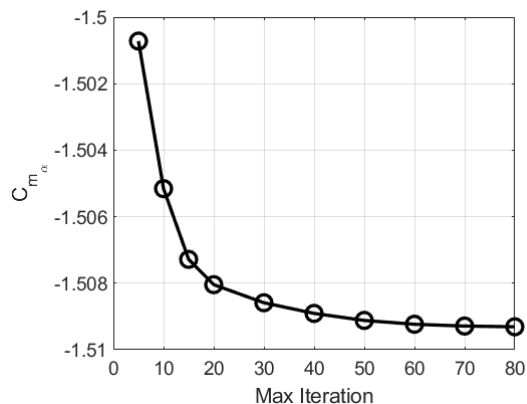


Figure 4.22: C_{m_α} convergence with no propeller

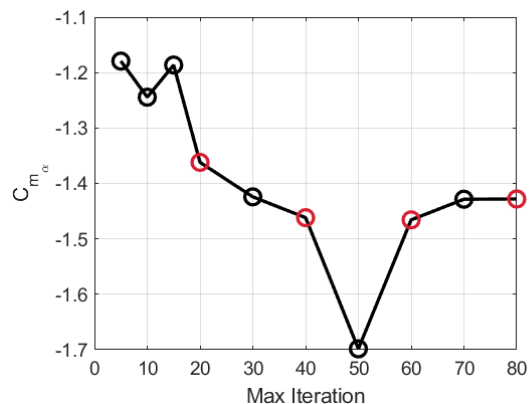


Figure 4.23: C_{m_α} convergence including propeller

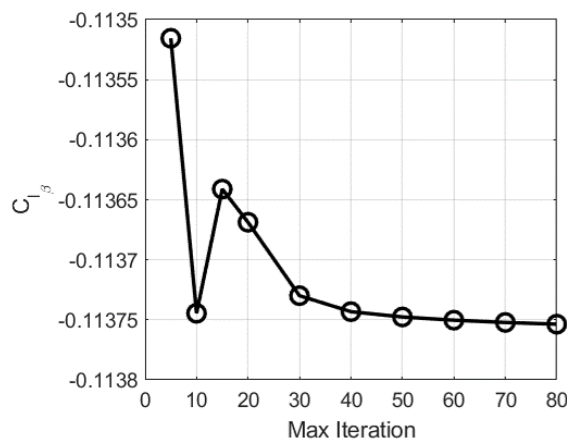


Figure 4.24: C_{l_β} convergence with no propeller

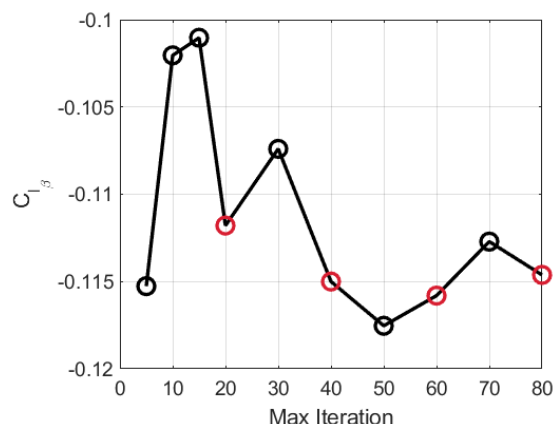


Figure 4.25: C_{l_β} convergence including propeller

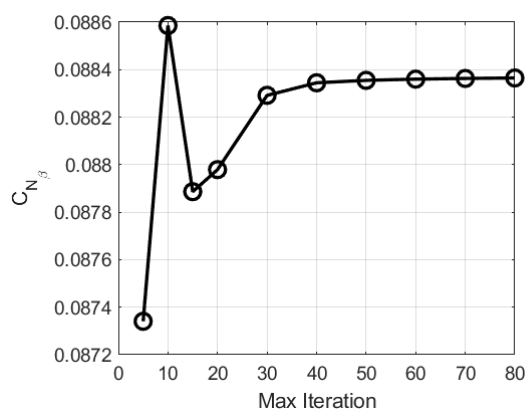


Figure 4.26: C_{n_β} convergence with no propeller

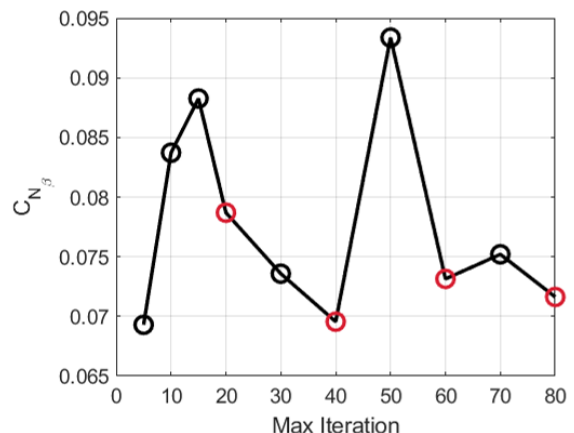


Figure 4.27: C_{n_β} convergence including propeller

Chapter 5

Optimisation Results and Discussion

This chapter outlines the optimiser settings, presents optimisation results, and discusses these results in the context of relevant literature. Section 5.1 outlines the three MAV configurations investigated in the optimisation. This is followed by a description of the optimiser set up and variable inputs in Section 5.2. Sections 5.3 and 5.4 present the optimisation results with and without propeller. The optimised MAV designs are compared against MAV designs from literature and the effect of propeller slipstream on the MAV optimisation is discussed. Finally, the high level optimisation trends with and without propeller are analysed in Section 5.5.

5.1 MAV Classes

Three separate MAV configurations were studied. In addition to these three configurations, two size classes were also tested. The term 'classes' will be used to refer to the MAV configuration including size (e.g Winglet 30cm span classss) and the term 'configuration' as the three distinct MAV geometries (e.g Flying Wing, GenMAV, etc). Each MAV configuration was based off existing MAV designs from literature. By studying the optimisation of a range

of configurations, we can develop a better understanding of the optimal MAV design space. Furthermore, as the Reynolds number is sensitive to aircraft size, investigating a range of MAV size classes allows us to better understand the effects of low Reynolds numbers on MAV design.

5.1.1 GenMAV

The GenMAV model, as outlined in Section 4.4, is a baseline MAV model developed by the Air Force Research Laboratory Munitions Directorate (AFRL/MD) to serve as a reference for future research (Stewart et al, 2007). GenMAV features an elliptical wing shape with a cylindrical fuselage, as shown in Figure 5.2. The empennage consists of both a horizontal and vertical stabilizer, fixed at $1.6 c_r$ behind the trailing edge. The vertical tail extends above the fuselage reference line. The GenMAV span and length is limited to 45 cm in line with the model from Stewart (2007). An Eppler E387 airfoil was used for the main wing with Ht-08 airfoils for horizontal and vertical tails.

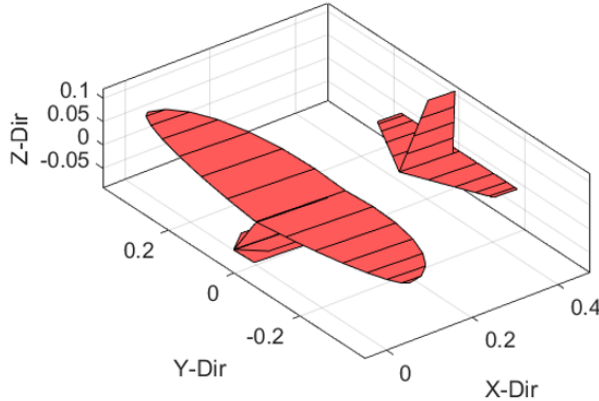


Figure 5.1: VAP 3.5 model of the GenMAV class

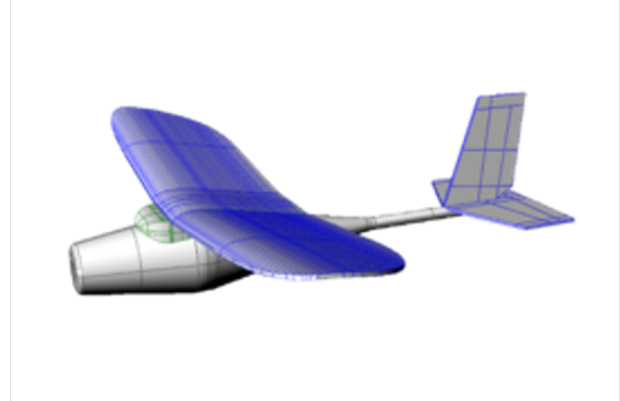


Figure 5.2: GenMAV model (Stewart et al, 2007)

5.1.2 Flying Wing

The flying wing configuration is commonly seen in MAVs. The specific configuration was based on the Pocket MAV (PMAV) model developed by Albertani et al. (2004). Shown in Figure 5.4, this configuration features an elliptical wing with a single vertical tail extending

above and below the fuselage, fixed to the trailing edge of the root chord. The lack of horizontal tail requires the use of a reflex airfoil¹. The Phoenix airfoil was chosen due to its high lift-to-drag ratio in low Reynolds numbers compared to other reflex airfoils (Campbell, 2020). A Ht-08 airfoil was used for the vertical stabiliser. The flying wing class was investigated with both 30 cm and 45 cm span constraints.

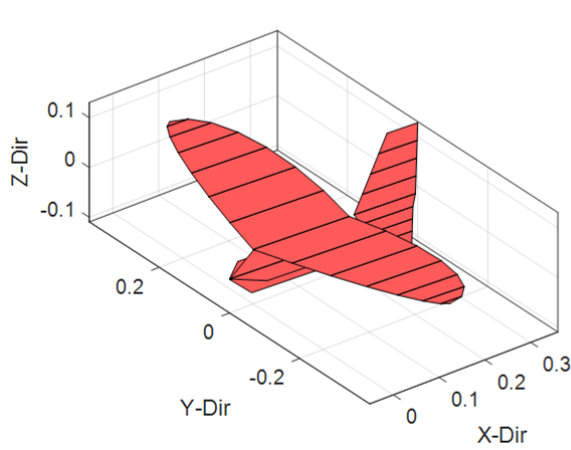


Figure 5.3: VAP 3.5 model of the Flying Wing class



Figure 5.4: PMAV model (Albertani et al, 2004)

5.1.3 Winglet Class

The final class features a rectangular tapered wing with wingtip vertical stabilizers. A small fuselage is also included. This configuration is also common for MAVS as shown in Van Magill (2016) and Shams et al (2020). The span constraint for this model was limited to 30 cm. Again a Phoenix airfoil is used for the main wing with Ht-08 airfoils for the wingtip vertical stabilizers. The Winglet class configuration is shown in Figures 5.5 and 5.6.

¹Reflex airfoils feature an inflected camber line to reduce the pitching moment

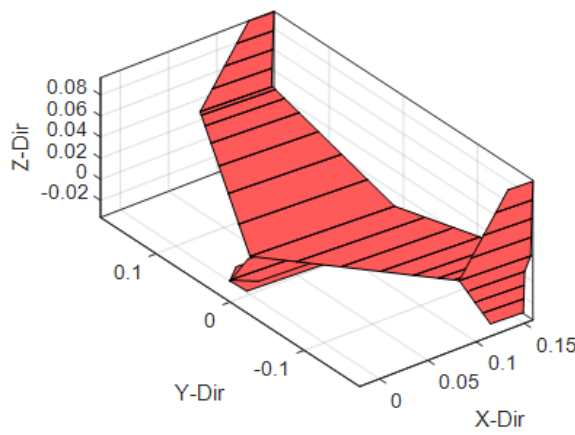


Figure 5.5: VAP 3.5 model of the Winglet class



Figure 5.6: Winglet model (Van Magill, 2016)

5.2 Optimiser Set Up

The optimiser settings can be split into variables, objectives, constraints. For this thesis, variables consist mainly of geometric parameters, used to define wing and empennage structures as discussed in Section 5.2.1. Objectives refer to the performance evaluations of the MAV designs, presented in Sections 5.2.2. Finally Section 5.2.3 outlines the constraint settings for the optimiser. These consist of trim, size and stability constraints.

5.2.1 Variables

The variables given to the optimiser are presented in Table 5.1. The selection of variables depended upon the MAV configuration, as shown in the second column. The aim in selecting the variable limits was to give the optimiser as much design authority as possible. The variable limits are chosen outside of common values seen in MAV design to ensure that the optimisation is not restricted by the author's conception of the optimised solution. This allows the optimisation algorithm to find irregular designs that would not be considered by human design. VT_{top} and VT_{bot} refer to the upper and lower areas of the vertical tail in the Flying Wing and Wingtips configurations.

Table 5.1: Optimisation variables used for all MAV configurations

| Variable | Configuration* | Min | Max | Units |
|--------------------------------|----------------|-------------------|------|-------------------|
| Conditions | | | | |
| Angle of Attack | All | 2 | 10 | deg |
| Main Wing | | | | |
| Aspect Ratio | A, B | 0.2 | 7 | - |
| Span | C | 0.05 | 0.45 | m |
| Root Chord | All | 0.05 | 0.45 | m |
| Sweep | All | -20 | 60 | deg |
| Taper Ratio | C | 0.01 | 1 | - |
| Twist | All | -5 | 5 | deg |
| Dihedral | All | -15 | 15 | deg |
| Horizontal Tail | | | | |
| HT Aspect Ratio | B | 0.5 | 4 | - |
| HT Volume Coeff. | B | 0.1 | 0.8 | - |
| HT Taper Ratio | B | 0.01 | 1 | - |
| Vertical Tail | | | | |
| VT _{top} Aspect Ratio | All | 0.5 | 2 | - |
| VT _{top} Volume Coeff | All | 0.01 | 0.25 | - |
| VT _{top} Taper Ratio | All | 0.01 | 1 | - |
| VT _{bot} Aspect Ratio | A, C | 0.5 | 2 | - |
| VT _{bot} Volume Coeff | A, C | 0.01 | 0.25 | - |
| VT _{bot} Taper Ratio | A, C | 0.01 | 1 | - |
| *Config A: | | *Config B: | | *Config C: |
| FlyingWing | | GenMAV | | Winglets |

5.2.2 Objectives

The two optimisation objectives used were the MAV mass and lift-to-drag ratio. The optimiser aimed to minimise MAV mass whilst maximising lift-to-drag ratio.

MAV Mass

Minimising the MAV mass reduces the lift and propulsive force required to cruise, potentially increasing range of the MAV. Furthermore, weight reduction increases the ease of MAV transportation and hence, improves its operational capabilities. As all MAVs investigated are battery powered, the mass calculated in Section 3.2 approximates the Maximum Take Off Weight (MTOW) as no mass is lost during flight.

Lift-to-drag Ratio

The lift-to-drag ratio (L/D) is a measure of aerodynamic efficiency. A high lift-to-drag ratio means that the aircraft is creating a large amount of lift relative to the drag generated. The lift-to-drag ratio is directly proportional to the MAV range, as increasing L/D reduces amount of propulsive power to overcome drag at a cruising lift coefficient ($L = W$).

5.2.3 Constraints

The optimisation constraints limit the design population to only feasible MAV designs. The MAV classes are set up by size and length constraints. Cruise condition trim constraints are also applied to optimise the MAV at the cruise flight condition. Static stability constraints limit the optimiser to generate only stable and controllable MAV designs.

Size Constraints

Two size classes were used to investigate the effect of low Reynolds number flow on aerodynamics. The MAVs were limited in both span and overall length as shown in Table 5.2.

Trim Constraints

The MAV designs were optimised at a cruise condition. In cruise all forces on the aircraft are in equilibrium. Only a minimum lift constraint was set because increasing lift further than required for cruise produces less optimal designs. Any increase in lift over the maximum L/D lift coefficient will result in a larger increase in drag. Therefore, the optimiser will steer away from designs with too much lift, making an upper lift constraint unnecessary.

For the propeller cases, a propulsive trim was also included. However, the propeller RPM was

kept constant for all models. A variable RPM means that the convergence of the forces on the empennage is not guaranteed (for a fixed VAP iteration limit and timestep within feasible computational time limits). Furthermore, the final propeller position will vary with RPM. As discussed in Section 4.5, the stability derivatives are very sensitive to final propeller location. Instead, the RPM was set to produce enough thrust to overcome drag for the estimated largest model. The iteration and timestep were defined to ensure the propeller completed two full revolutions. This means that the smaller models will be overpowered for cruise. However, this simplification is expected to not affect the overall propeller-wing interaction significantly. The trim constraints are presented in Table 5.3

Table 5.2: Size Constraints

| Constraint | Small Class | Large Class |
|------------|-------------|-------------|
| Max Span | 30 cm | 45 cm |
| Max Length | 30 cm | 45 cm |

Table 5.3: Trim Constraints

| Constraint | No Prop. | Prop. |
|------------|----------|---------|
| Lift | $L > D$ | $L > D$ |
| Thrust | None | $T > D$ |

Stability Constraints

Static longitudinal, lateral and directional stability constraints were applied to limit the optimiser to stable and controllable MAV designs as outlined in Table 5.4. These constraints are applied using the numerical stability derivatives calculated as described in Section 3.3. The requirements for static stability are outlined in Appendix A.4 and A.5. Controllability limits were also applied to the stability derivatives based off results from the GenMAV model (Stewart et al, 2007). A Dutch Roll constraint is also applied to reduce dynamic lateral instability taken from Ryder (2020).

Table 5.4: Stability Constraints

| State | Derivative | Min | Max |
|-----------------|--|---------------|---------------|
| Pitch | C_{m_α} | -1.6 | -0.05 |
| Yaw | C_{n_β} | 0.05 | 0.6 |
| Roll | C_{l_β} | -0.3 | 0 |
| Dutch Roll Mode | $\left \frac{C_{n_\beta}}{C_{l_\beta}} \right $ | $\frac{1}{3}$ | $\frac{2}{3}$ |

5.3 Optimisation Without Propeller

This section outlines the optimisation results without propeller. Each optimisation was run for 100 iterations with 8 designs per optimisation variable (88 total population size). The smaller 30 cm class was set to a cruise velocity of 18 m/s while the larger 45 cm class cruises at 22 m/s, based off performance of similar models (Hassanalian et al, 2017). The small and large MAV class optimisation results are presented in Sections 5.3.1 and 5.3.2 respectively.

5.3.1 30 cm Class

Figures 5.7 and 5.8 show the optimisation history for the Flying Wing and Winglet configurations with 30 cm size constraints. Each dot represents a feasible MAV design, plotted against the two optimisation objectives, mass and L/D .

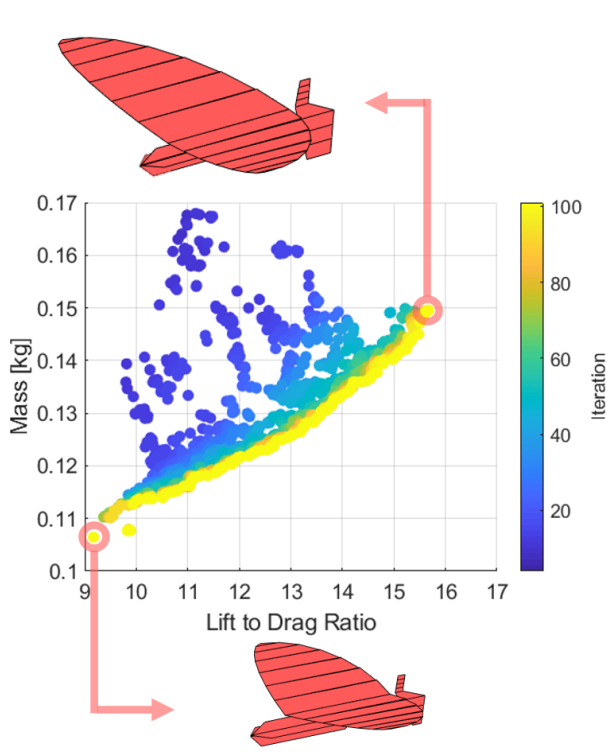


Figure 5.7: Iteration history of Flying Wing 30cm class

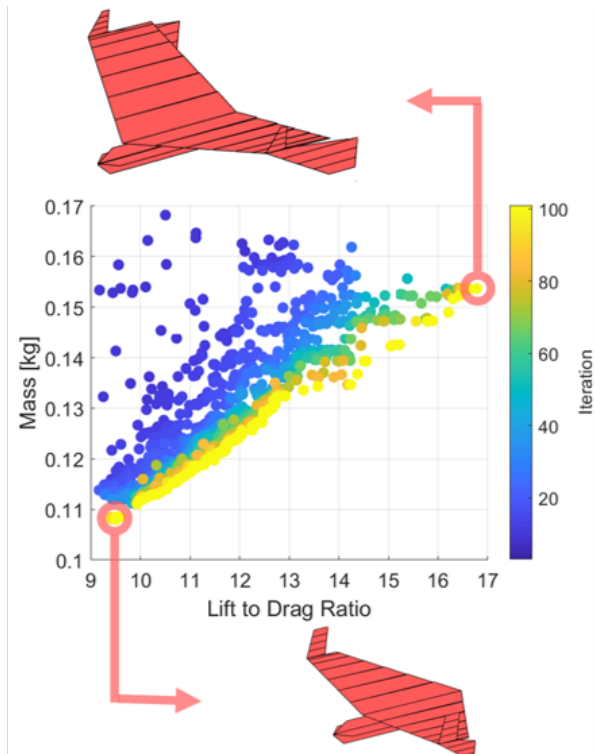


Figure 5.8: Iteration history of Winglet 30cm class

For both the Flying Wing and Winglet class the optimisation algorithm progressively finds better designs as the optimisation proceeds. We can see a Pareto front developed in the final iterations, representing the optimised design trade off between L/D and mass. To generate a higher L/D the optimiser increases the wing size, increasing the aircraft mass and visa versa. The optimiser produces a relatively large range of feasible designs compared to Ryder (2020), who found a max variation in mass and L/D of 20% across the Pareto front. A 40 to 50 g (50%) change in mass is seen across the Pareto front for both configurations. This correlates with a L/D difference of 9 to 10 (80%) across the Pareto front.

The maximum L/D and minimum mass VAP models are highlighted. The minimum mass design features a smaller wing area and lower aspect ratio. The max L/D and min mass models are compared against existing MAV models from literature in Table 5.5.

Table 5.5: 30 cm span class optimal designs without propeller compared to MAVs from literature

| Model / Reference | Configuration | Span | Mass | Max L/D |
|---------------------------|---------------|-------|-------|---------|
| Novel Designs | | | | |
| Min Mass | Flying Wing | 17 cm | 106 g | 9.2 |
| Min Mass | Winglets | 18 cm | 108 g | 9.4 |
| Max L/D | Flying Wing | 30 cm | 150 g | 15.7 |
| Max L/D | Winglets | 30 cm | 154 g | 16.8 |
| Published MAVs | | | | |
| Chen & Qin, 2013 | Flying Wing | 35 cm | 200 g | 7.4 |
| Van Magill , 2016 | Winglets | 30 cm | 99 g | 11 |
| Cosyn & Vierendeels, 2007 | Flying Wing | 25 cm | 58 g | 5 - 7* |
| Jana et al, 2017 | Biplane | 15 cm | 40 g | 3 |

*estimated from MAV drag polar

Compared to published MAVs the maximum L/D models for both Flying Wing and Winglet configurations have higher max L/D ratios. However, the max L/D models also have a mass at least 50% higher. The minimum mass models are closer to the Van Magill (2016) and Cosyn (2007) MAVs featuring a similar L/D and slightly higher mass. This difference in

mass is to be expected as the MAV mass is calculated based off a balsa wood skin and foam core (Hassanalian et al, 2017). The Van Magill (2016) and Cosyn & Vierendeels (2007) designs are constructed with a fibreglass skin, not balsa. Despite the differences in mass, the novel MAV designs highlight the potential performance improvements from optimisation of wing and tail geometries.

Figures 5.9 to 5.10 highlight the effect of root chord on the optimisation objectives. In line with results from Ryder (2020), Campbell (2020) and Farah (2019), the optimiser finds minimising root chord most desirable. However, for these results, the root chord influences the aircraft stability much more, as no horizontal stabilizer is included unlike Ryder (2020) and Farah (2019). A smaller root chord shifts the aerodynamic centre forwards, increasing longitudinal stability. As a result the optimisation cannot reduce the root chord to the lower bound (0.05). The optimiser balances the mass reduction from reducing root chord with the increased lift and stability improvements of a larger root chord. For both configurations, a root chord of 13-16 cm is most desirable across the entire Pareto front.

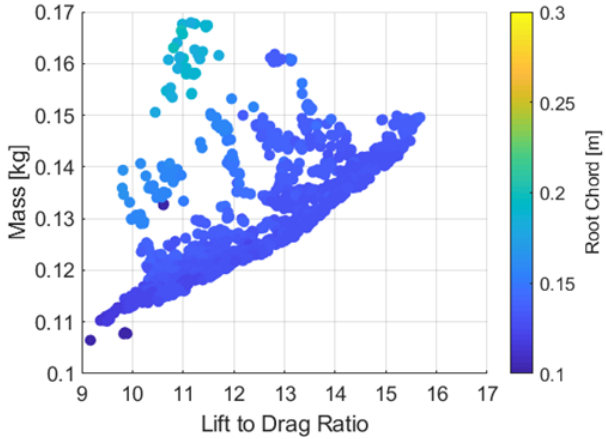


Figure 5.9: Flying Wing 30cm: Root Chord

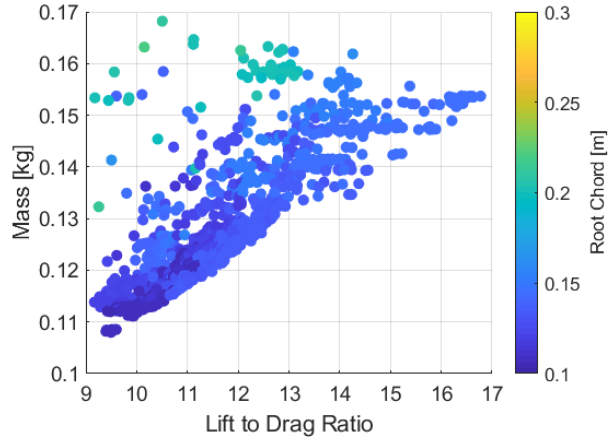


Figure 5.10: Winglet 30cm: Root Chrod

Figures 5.11 and 5.12 show how increasing wing aspect ratio increases lift-to-drag ratio. High aspect ratio wings produce less lift induced drag and are generally more aerodynamically efficient. However, as the span increases, so does the aircraft mass. Hence, the minimum weight models feature a lower aspect ratio wing. The aspect ratio is limited by the span constraint, reaching a maximum of 2.5 for the Flying Wing and 3 for the Winglet configuration.

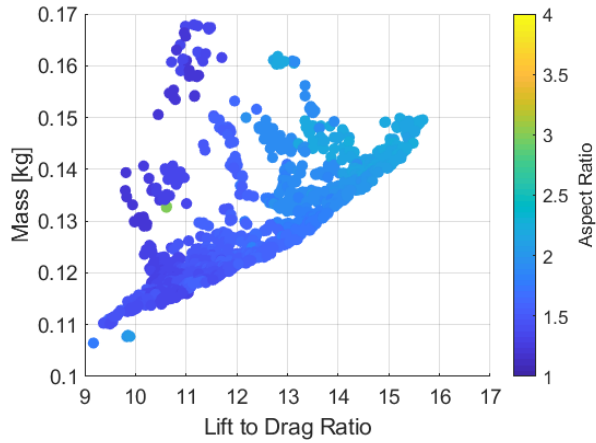


Figure 5.11: Flying Wing 30cm: Aspect Ratio

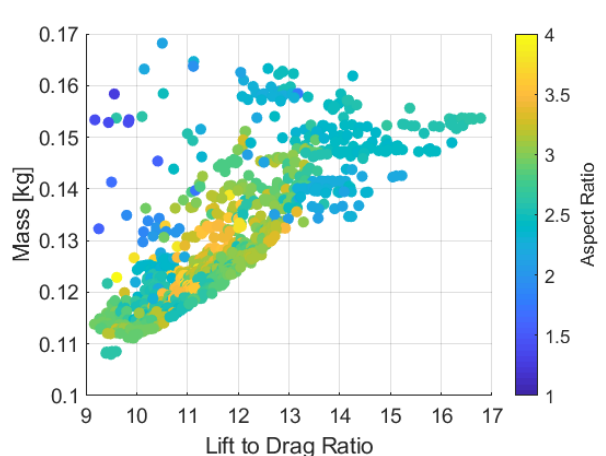


Figure 5.12: Winglet 30cm: Aspect Ratio

Figures 5.13 and 5.14 show the influence of leading edge sweep on the optimised designs. For the Flying Wing configuration the forward sweep angle² produces higher lift-to-drag ratios. Forward sweep can generate inboard spanwise flow, generating more lift near the wing root and improving the lift-to-drag ratio (Traub and Lawrence, 2009). The downside is that the aircraft becomes less directionally stable, as gust disturbances will generate a negative yawing moment as the forward swept wings are in front of the aircraft CG. The Flying Wing configuration can get away with this because of the vertical stabiliser anchored at the root chord trailing edge. However, in the Winglet configuration, the vertical stabilisers move with the wing tip, meaning they need to remain behind the CG for directional stability. The results of the Winglet case show this, featuring swept back wings as shown in Figure 5.14.

The effect of dihedral is shown in Figures 5.15 and 5.16. The Flying Wing optimisation finds a large dihedral to be the best across the entire Pareto front. The Winglet optimisation shows two distinct optimisation paths featuring large and small dihedral angle. The large dihedral designs feature higher L/D ratios and masses. It is interesting to note the correlation between sweep and dihedral for the Winglet model. Large dihedral angles are correlated with swept back wings and visa versa. This relationship is caused by the lateral stability C_{l_β} lower

²Forward sweep defined by negative angles.

bound. The dihedral effect³ is reduced with sweep, as the induced wing angle of attack with a sideslip disturbance is decreased. Hence, wings with low sweep and large dihedral angles will produce the largest C_{l_β} , exceeding the controllability limit ($C_{l_\beta} > -0.3$) while swept back wings require higher dihedral to reach the same C_{l_β} .

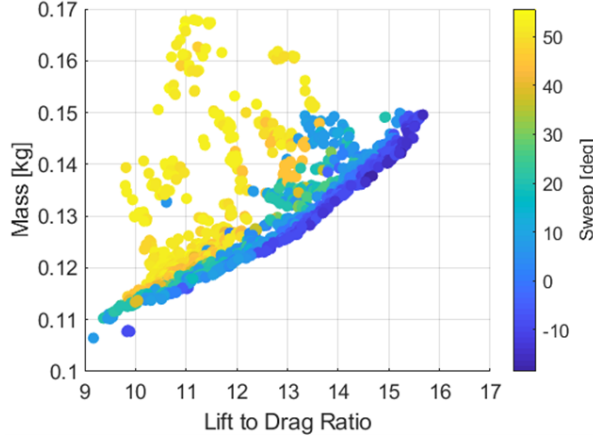


Figure 5.13: Flying Wing 30cm: Sweep

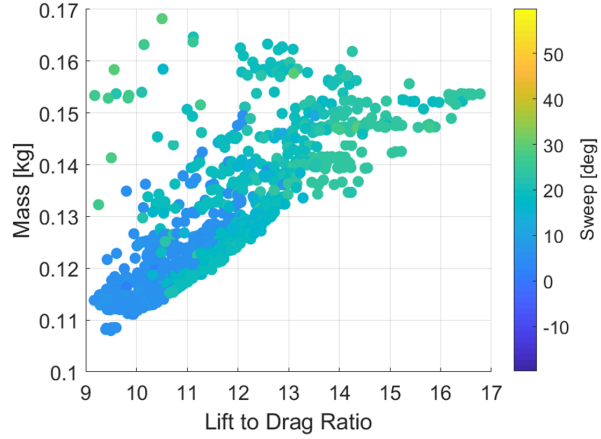


Figure 5.14: Winglet 30cm: Sweep

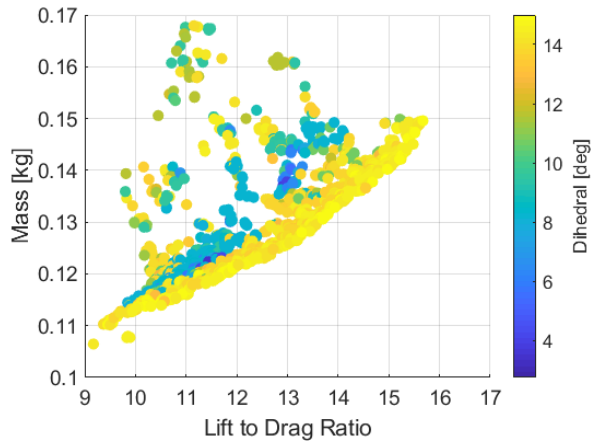


Figure 5.15: Flying Wing 30cm: Dihedral

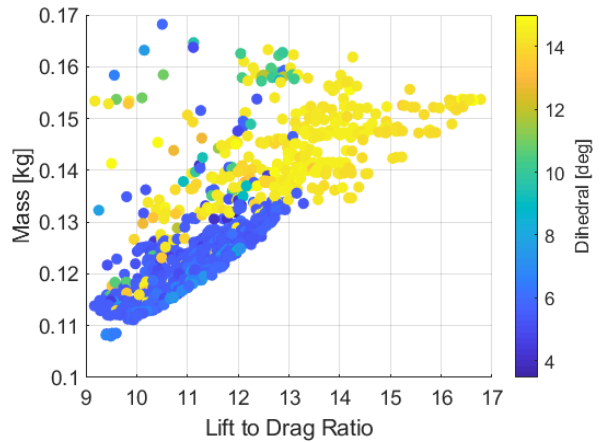


Figure 5.16: Winglet 30cm: Dihedral

The Winglet taper ratio and vertical stabiliser size are also correlated with the wing sweep and dihedral, shown in Figures C.1 and C.2, in Appendix C. As the wings are swept back, the moment arm from the wingtips to CG increases. The larger moment arm and higher

³Dihedral effect refers to the redirection of wing lift laterally by a wing dihedral Angle

dihedral with swept wings reduces the tail size in order remain within $C_{l\beta}$ limits. Increased wing sweep is also correlated with a less tapered wing.

5.3.2 45 cm Class

The optimisation history for the 45 cm class are shown in Figures 5.17 and 5.18. The 45 cm class includes Flying Wing and GenMAV configurations.

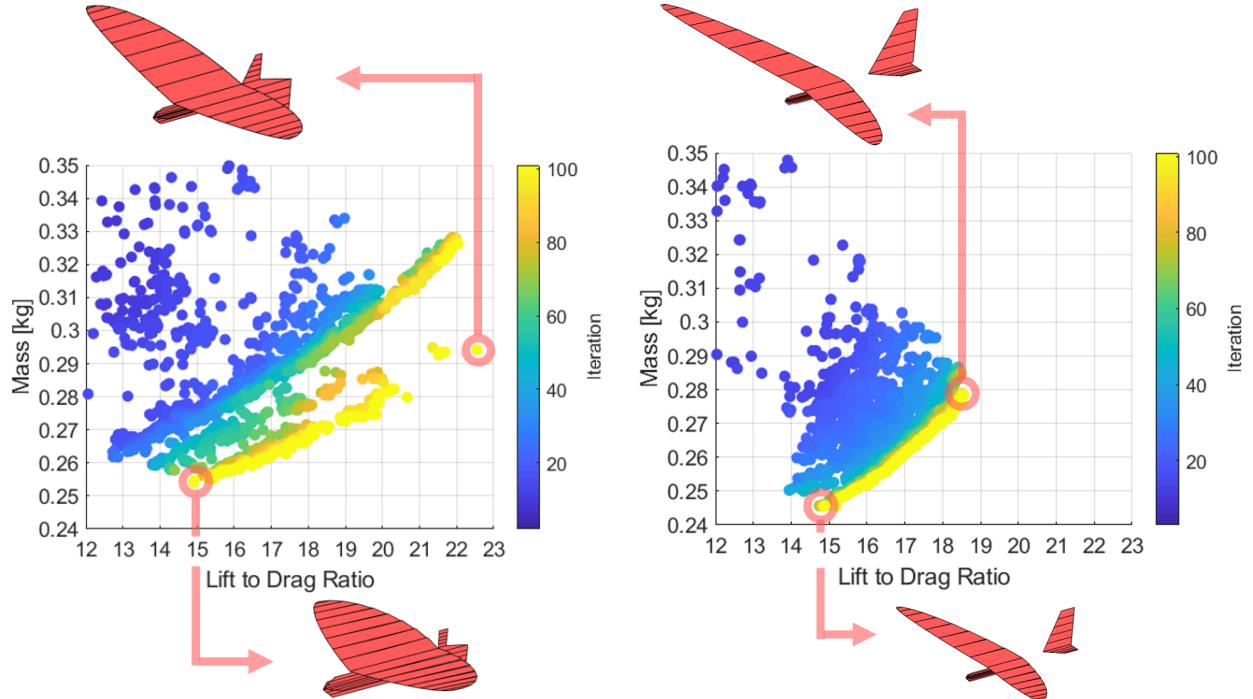


Figure 5.17: Iteration history of Flying Wing 45cm class

Figure 5.18: Iteration history of GenMAV 45cm class

The Reynolds number increases from approximately 1.0×10^5 for the 30 cm class, to approximately 1.6×10^5 in the 45cm class. As predicted by Mueller (1985), aerodynamic performance improves with increased Reynolds number. A L/D increase of 20-30% is observed in the 45cm class compared to 30cm class. Again the optimiser finds a wide range of feasible solutions with a large Pareto front developed in both configuration optimisations. The GenMAV models featured slightly lower L/D ratios due to the extra drag generated from the horizontal stabilizer. Despite this both Flying Wing and GenMAV classes reached very high maximum L/D ratios of 22.5 and 18.6 respectively.

The minimum weight and maximum L/D models are compared against MAVs from literature in Table 5.6

Table 5.6: 45 cm span class optimal designs without propeller compared to MAVs from literature

| Model / Reference | Configuration | Span | Mass | Max L/D |
|-----------------------|---------------|---------|-------|---------|
| Novel Designs | | | | |
| Min Mass | FlyingWing | 25 cm | 254 g | 14.9 |
| Min Mass | GenMAV | 36 cm | 246 g | 14.8 |
| Max L/D | FlyingWing | 45 cm | 294 g | 22.5 |
| Max L/D | GenMAV | 45 cm | 279 g | 18.6 |
| Published MAVs | | | | |
| Bronz, 2009 | GenMAV | 50 cm | 300 g | 16-18* |
| Hassanalian, 2014 | Flying Wing | 43.2 cm | 430 g | 10.8 |
| Shams, 2020 | Winglets | 50 cm | 200 g | 8.5 |
| Stewart, 2006 | GenMAV | 58 cm | 530 g | 8.4 |
| Chen, 2004 | Flying Wing | 35 cm | 200 g | 7.4 |

*estimated from MAV drag polar

Both the minimum mass and max L/D novel designs have a higher L/D than published MAVs of a similar mass. Notably, the max L/D GenMAV novel design is very similar to the MAV from Bronz et al (2009). Comparing the optimised designs to MAVs from literature suggests that the novel designs are feasible and realistic. Furthermore, the optimiser finds MAV designs which outperform published MAV designs.

For the 45cm class the main wing aspect ratio was proportional to L/D as found in the 30cm class, shown in Figures 5.19 and 5.20. With the horizontal tail to control longitudinal stability, the GenMAV main wing can be designed purely for efficiency. As a result the GenMAV case features a shorter root chord as shown in Figures 5.21 and 5.22, as well as much higher aspect ratios.

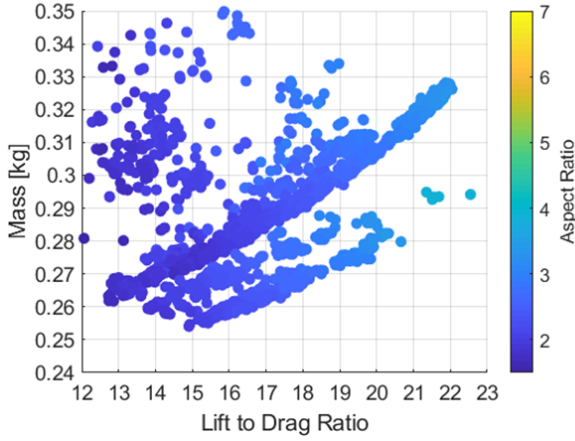


Figure 5.19: Flying Wing 45cm: Aspect Ratio

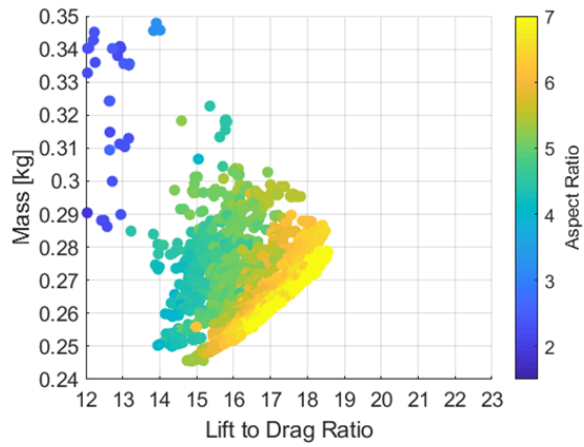


Figure 5.20: Genmav 45cm: Aspect Ratio

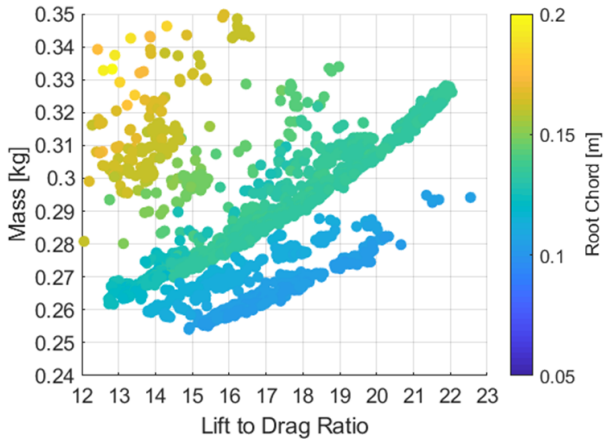


Figure 5.21: Flying Wing 45cm: Root Chord

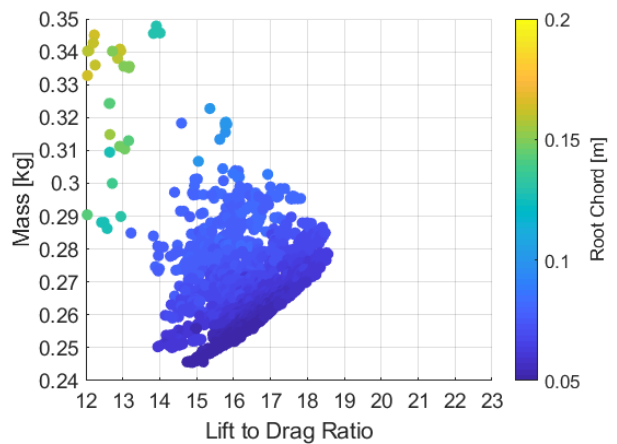


Figure 5.22: Genmav 45cm: Root Chord

The fixed horizontal tail on the GenMAV draws the neutral point aft of the centre of gravity, meaning that the GenMAV configuration can have forward sweep without becoming longitudinally unstable. The vertical stabiliser on the GenMAV class also counteracts the negative directional stability effects of forwards sweep. As a result, the optimised GenMAV designs feature a large forward wing sweep as shown in Figure 5.24. The effect of sweep for the Flying Wing configuration is presented in Figure 5.23. Interestingly, the optimiser now finds swept back wings more desirable; opposite of the smaller class. This is likely caused by the increased Reynolds number increasing the lift distribution near the wing tip. The

outboard wing has the shortest chord and experiences the lowest Reynolds number flow. For the 30cm class, the wingtips may experience reduced lift due to laminar separation bubbles (Mueller, 1985). The reduced lift reduces the outboard wing influence on the aerodynamic centre of lift. As the Reynolds number increases, the local lift in the outboard wing increases and shifts the aerodynamic centre forward (for forward swept wings), causing longitudinal instability. This effect is compounded by the higher aspect ratio wing of the 45 cm class, meaning the centre of gravity is more sensitive to sweep. Hence, forward sweep designs are not feasible at higher Reynolds numbers and a swept back wing is required.

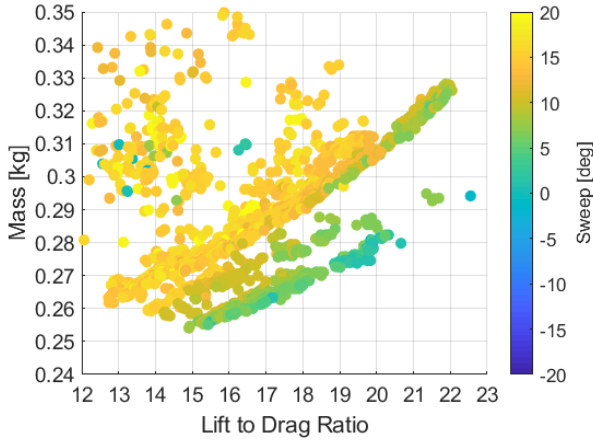


Figure 5.23: Flying Wing 45cm: Sweep

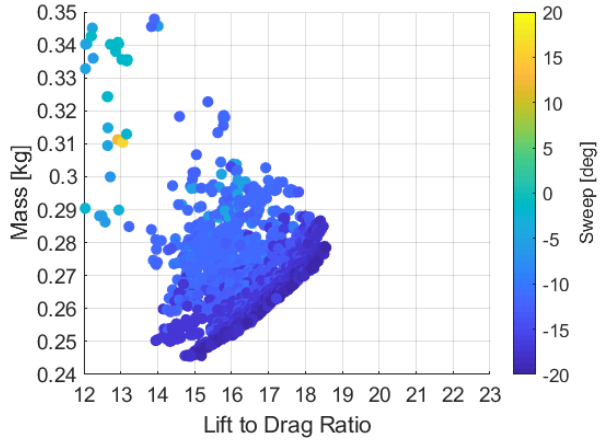


Figure 5.24: GenMAV 45cm: Sweep

Finally, the variation of the stability derivatives C_{m_α} , C_{l_β} and C_{n_β} are presented in Figures 5.25 to 5.30. The optimiser finds a small C_{m_α} most desirable for the Flying Wing configuration. A small pitch stiffness means less aerodynamic correctional force, resulting in lower drag and a higher overall aerodynamic efficiency. The GenMAV configuration has a much larger pitch stiffness due to the horizontal stabiliser. C_{m_α} also increases with higher L/D models due to the increased tail size and moment arm. The optimiser finds that a large roll stability derivative C_{l_β} is best, converging to the lower bound ($C_{l_\beta} > -0.3$). The directional stability derivative C_{n_β} is maximised to the upper bound ($C_{n_\beta} < 0.6$).

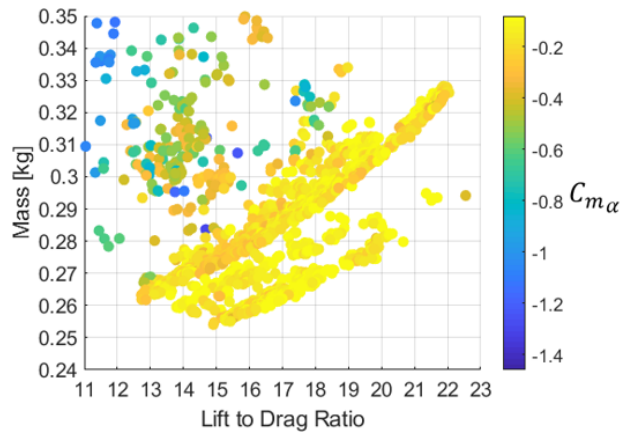


Figure 5.25: Flying Wing 45cm: C_{m_α}

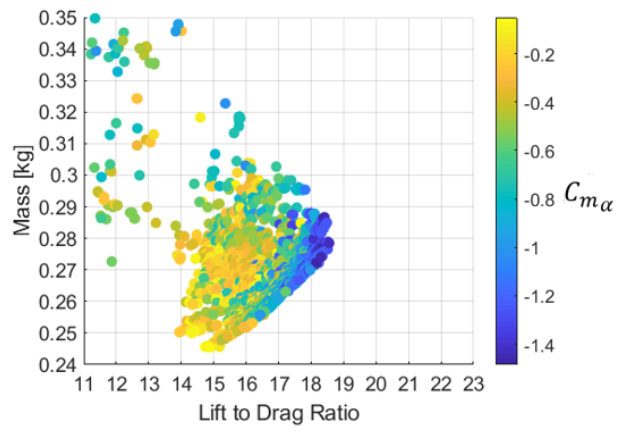


Figure 5.26: GenMAV 45cm: C_{m_α}

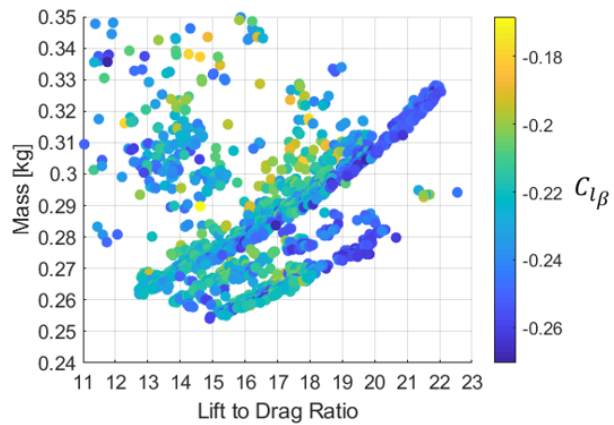


Figure 5.27: Flying Wing 45cm: C_{l_β}

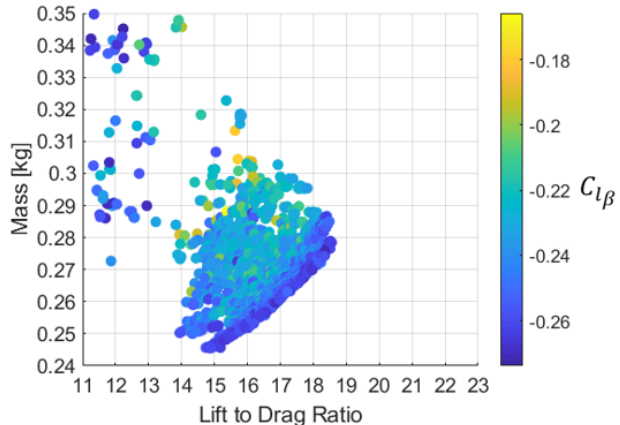


Figure 5.28: GenMAV 45cm: C_{l_β}

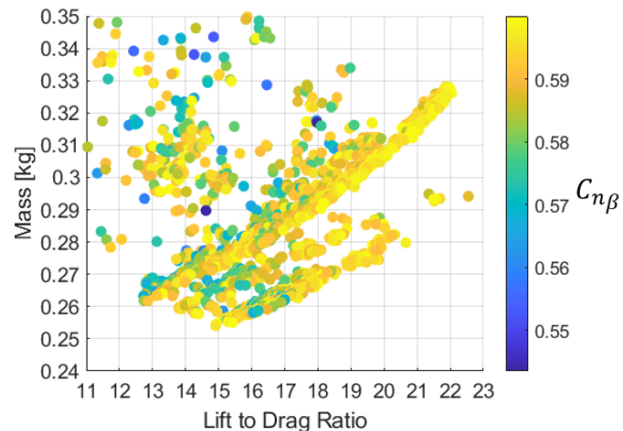


Figure 5.29: Flying Wing 45cm: C_{n_β}

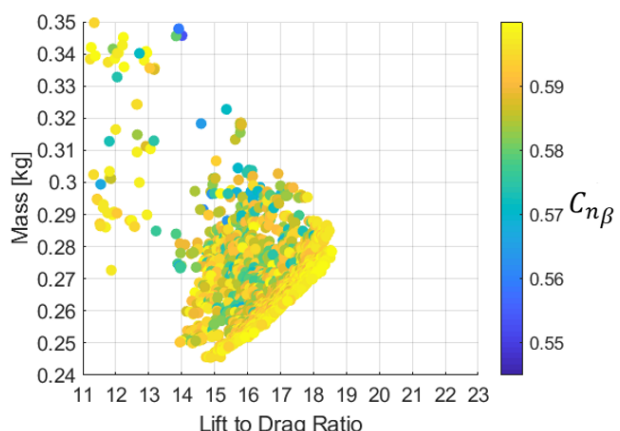


Figure 5.30: GenMAV 45cm: C_{n_β}

5.4 Optimisation With Propeller

This section presents the results of the MAV optimisations including propeller. Three propellers were selected based off MAV models from literature with similar size and weight (Hassanalian et al, 2017 and Shams et al, 2020). The 45cm class was optimised with two sizes of propeller to investigate the propulsive trim effects on the optimal MAV designs. An outline of the optimisation runs including propellers is presented in Table 5.7.

Table 5.7: Propeller optimisations outline

| MAV Size | Configurations | Propeller | Section |
|----------|-----------------------|------------------------|---------|
| 45 cm | Flying Wing, GenMAV | GWS Direct Drive 5×4.3 | 5.4.1 |
| 45 cm | Flying Wing, GenMAV | APC Sport 7×6 | 5.4.2 |
| 30 cm | Flying Wing, Winglets | GWS Direct Drive 4×4 | 5.4.3 |

The propeller optimisation results are compared against the optimisation without propeller as well as relevant literature. The results show that including propeller effects in MAV design optimisation produces significantly different optimal designs.

5.4.1 45cm Class with 5 inch propeller

The optimisation history of the 45 cm class using a GWS 5x4.3 propeller is presented in Figures 5.31 and 5.32. This is the smaller of the two propellers tested on this size class. Due to the added propulsive trim constraint and added complexity from propeller modelling, the optimiser produces a less dense point cloud and incomplete Pareto front. Nevertheless, the optimisation is sufficiently developed to identify trends in the optimal MAV designs.

The lift-to-drag ratios of the best designs are significantly reduced compared to the results without propeller. For the Flying Wing configuration, the maximum L/D is reduced from 22.5 without propeller to 14.5 including a 5 inch propeller (35% reduction). A similar reduction is seen in the GenMAV class, reducing from 18.6 to 13.9 (25% reduction).

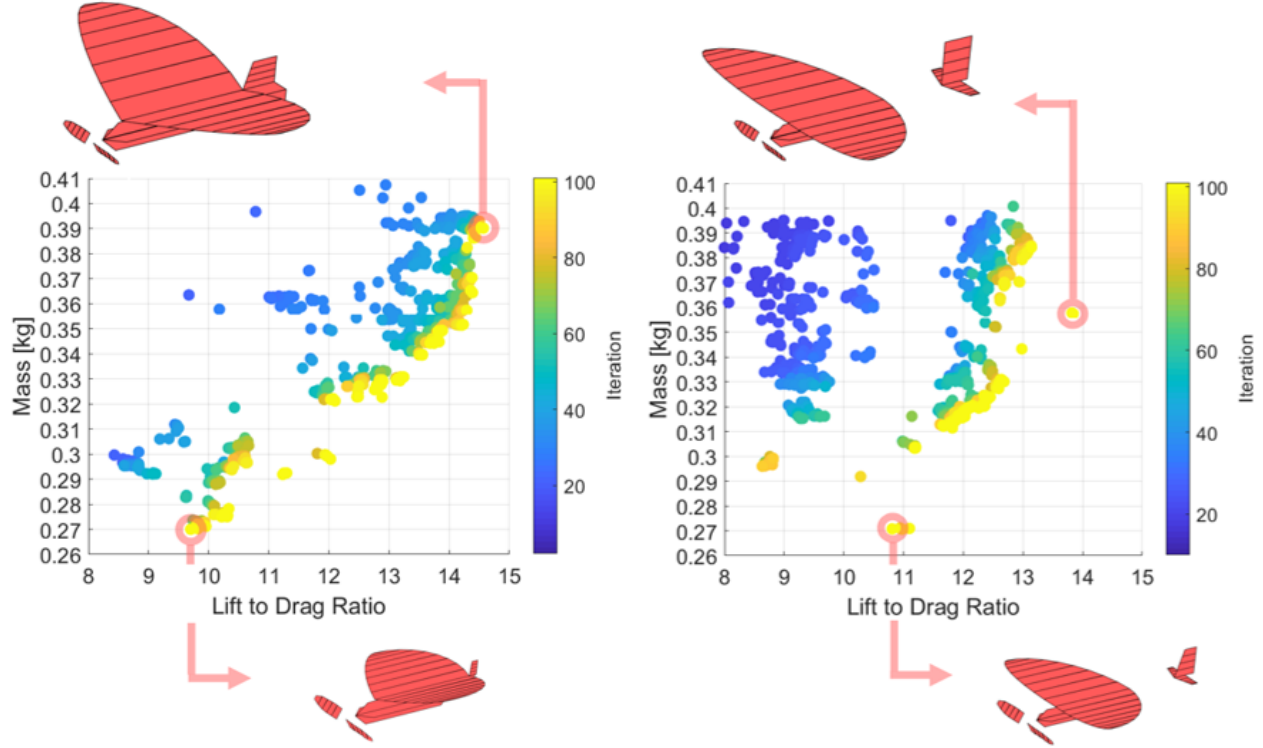


Figure 5.31: Iteration history of the 45cm Flying Wing including GWS 5x4.3

Figure 5.32: Iteration history of the 45cm GenMAV including GWS 5x4.3

This L/D reduction is within the range predicted by experimental studies from Null et al (2005). Shkarayev et al (2008) attributes this decrease in L/D to the disproportionate drag increase with the inclusion of propeller slipstream. Furthermore, the reduction L/D is likely also due to the propellers effect on longitudinal stability. As shown in Section 4.5, propeller wash reduces the pitch stiffness of the aircraft. With the optimiser finding low pitch stiffness to be most desirable (Figures 5.25 and 5.26), the effect of propeller on the optimised designs is likely to cause longitudinal instability. As a result the optimiser is required to sacrifice wing performance for longitudinal stability. Comparing the optimised designs to MAVs from literature, which include propeller effects in performance, is presented in Table 5.8. It is worth reiterating that there is a lack of optimised MAV designs which include the effect of propeller. Instead, most MAV performance data including propeller effects are either baseline MAVs or non-flying test structures.

Table 5.8: 45 cm class optimal designs including propeller compared to MAVs from literature

| Model / Reference | Configuration | Span | Mass | Max L/D |
|-----------------------|--|---------|-------|---------|
| Novel Designs | | | | |
| Min Mass | FlyingWing | 18 cm | 270 g | 9.7 |
| Min Mass | GenMAV | 23 cm | 272 g | 10.9 |
| Max L/D | FlyingWing | 45 cm | 390 g | 14.5 |
| Max L/D | GenMAV | 40 cm | 357 g | 13.8 |
| Published MAVs | | | | |
| Shkarayev, 2008 | Flying Wing (VTOL) | 30 cm | 173 g | 11.9 |
| Thipyopas, 2005 | Inverse Zimmerman wing test structure | 19.5 cm | N/A | 5.43 |
| Durai, 2011 | Flying Wing test structure | 30 cm | N/A | 5.7 |

The optimised designs produce significantly higher L/D ratios compared to the designs from literature. The VTOL Flying Wing model from Shkarayev et al (2008) has similar performance to the minimum mass optimal designs. It is clear that the optimiser is generating better MAV designs compared to models from literature which include propeller effects.

As shown in Figures 5.33 and 5.34 the propeller optimised designs feature a higher root chord compared to the cases without propeller. A 40% increase in root chord is seen for the Flying Wing case and a 200% increase for the GenMAV optimisation without propeller. This is likely to counteract the negative stability effects of the propeller slipstream. The larger root chord shifts the aerodynamic centre aft increasing longitudinal stability. The higher root chord is the reason why the designs with propeller have higher estimated masses than the optimal designs without propeller.

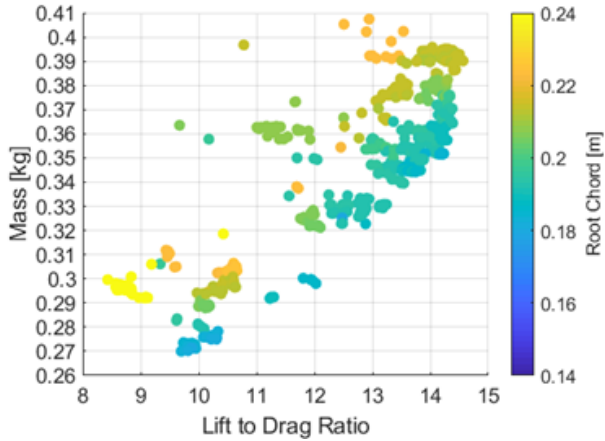


Figure 5.33: Flying Wing 45cm with 5" prop: Root Chord

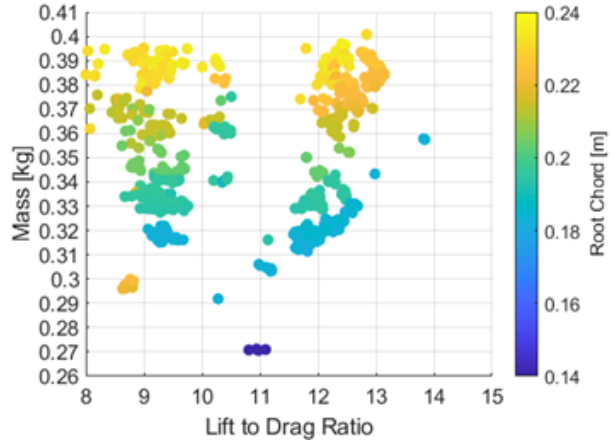


Figure 5.34: GenMAV 45cm with 5" prop: Root Chord

The wing sweep for both configurations is shown in Figures 5.35 and 5.36. Similar to the 45 cm optimisations without propeller, the Flying Wing requires sweptback wings for longitudinal stability. The GenMAV configuration is free to sweep the wings forward because of the horizontal stabilizer. With the inclusion of the propeller, the optimal designs have increased sweep (swept back) compared to the optimisation without propeller (5-10 degree change for the Flying Wing and a 4-8 degree change for GenMAV designs). This is again likely due to the instability effects of the propeller wash. The optimisation requires wing sweep to shift the aerodynamic centre aft, correcting for the reduction in longitudinal stability from the propeller slipstream.

Because of the increased root chord, the aspect ratios of the designs including propeller are lower, shown in Figures 5.37 and 5.38. In particular the GenMAV design aspect ratio is particularly restricted, reducing from a maximum of 7 without propeller to 2.2 with propeller. This reduction is likely also due to the models failing to meet the propulsive trim constraint. For the models featuring the highest L/D ratios, the 5 inch GWS 5x43 propeller is under powered at max RPM. This limits the GenMAV max L/D model to a max span of 40 cm. In Section 5.4.2 the effect of propulsive trim is investigated using a larger propeller.

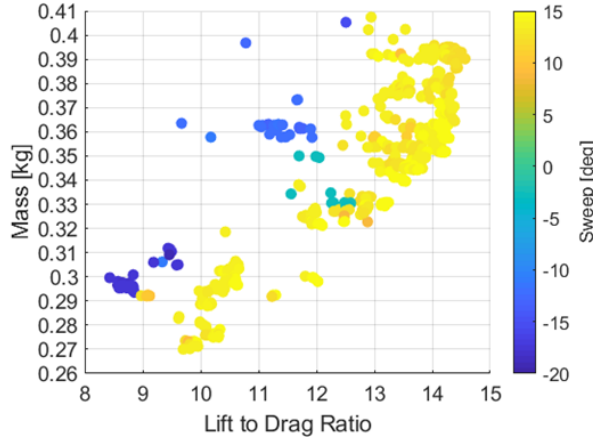


Figure 5.35: Flying Wing 45cm with 5" prop: Wing Sweep

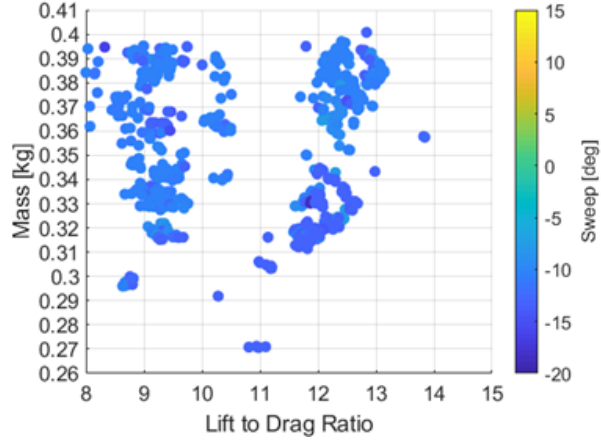


Figure 5.36: GenMAV 45cm with 5" prop: Wing Sweep

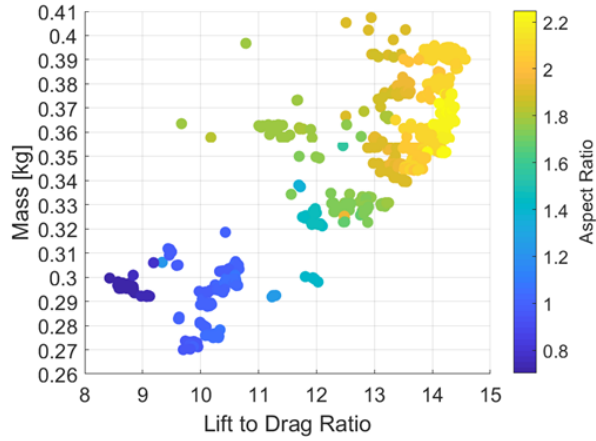


Figure 5.37: Flying Wing 45cm with 5" prop: Aspect Ratio

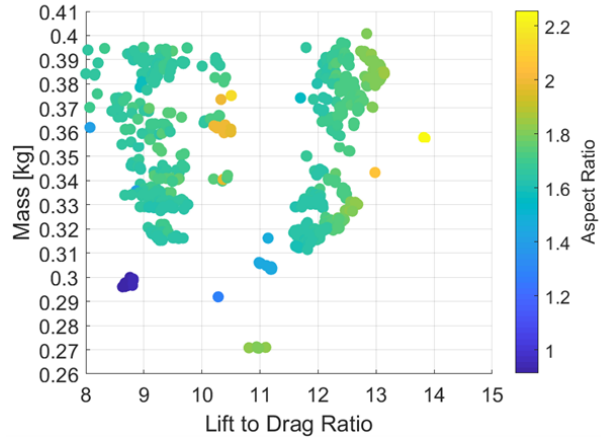


Figure 5.38: GenMAV 45cm with 5" prop: Aspect Ratio

5.4.2 45 cm Class with 7 inch propeller

The 45cm configurations were optimised using a larger 7 inch propeller to investigate the effect of increased thrust on the optimisation. The optimisation histories for these runs are presented in Figures 5.39 and 5.40. The larger propeller produces a higher thrust and increases the area of influence of the propeller slipstream on the wing. The smaller propeller required a lower advance ratio ($J = 0.5$) to meet trim constraints. The larger propeller was able to be run at a higher advance ratio ($J = 0.7$), whilst meeting thrust requirements.

The higher advance ratio reduces the helical angle of the propeller wash and decreases the induced angle of attack on the wing, potentially reducing the asymmetric lift deformation.

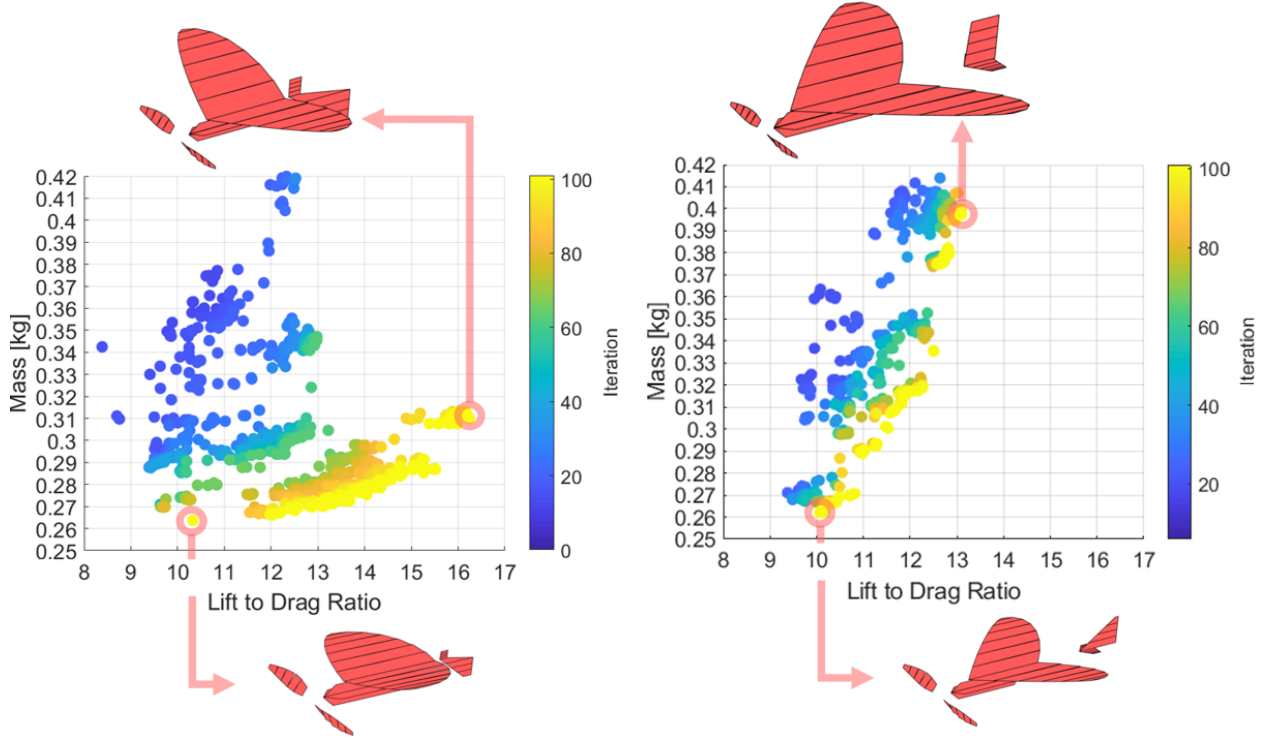


Figure 5.39: Iteration history of the 45cm Flying Wing including APC 7x6

Figure 5.40: Iteration history of the 45cm GenMAV including APC 7x6

The larger propeller increases the maximum lift-to-drag by 10-15% percent for the Flying Wing model compared to the 5 inch propeller. The GenMAV optimisation showed a similar Pareto front compared to the 5 inch propeller optimisation. The larger propeller produced optimal designs with 5-8% lower L/D ratios for similar MAV masses. The GenMAV optimisation Pareto front is much steeper than the Flying Wing, meaning a larger mass penalty is incurred to increase L/D . The extra drag from the GenMAV empennage, increased further by the propeller slipstream, requires larger changes in wing area to increase L/D compared to the Flying Wing configuration. It appears that the extra lifting surfaces in propeller slipstream cause large increases in drag. For the Flying Wing configuration, the optimiser minimises the upper vertical tail area, instead controlling C_{l_β} with the wing dihedral. A larger underside vertical stabiliser is included to increase C_{l_β} above the lower controllability limit ($C_{l_\beta} > -0.3$).

The main effect of the larger propeller is the increased wing sweep compared to the 5 inch propeller optimisation. Figures 5.41 and 5.42 highlight the effect of sweep angle. Note the scale difference between Figures 5.41 and 5.42, and the 5 inch propeller optimisation figures.

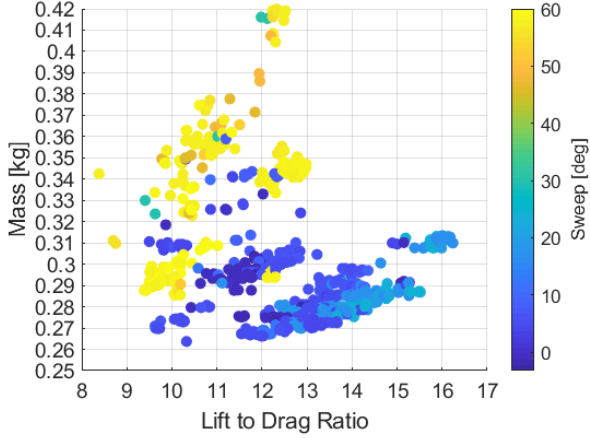


Figure 5.41: Flying Wing 45cm with 7" prop: Sweep

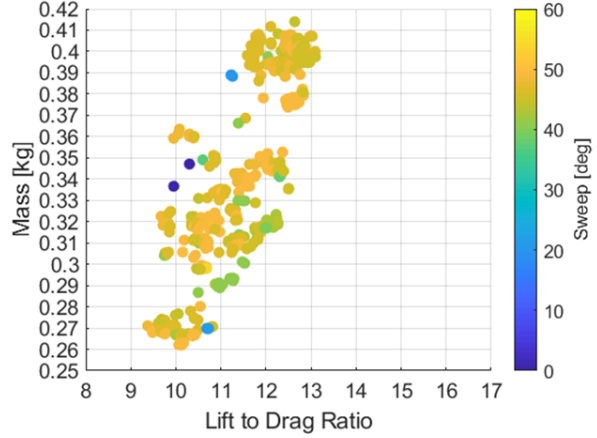


Figure 5.42: GenMAV 45cm with 7" prop: Sweep

The larger propeller increases the slipstream size and strength, deforming the lift distribution further towards the wing root. This requires the optimal MAV designs to have larger sweep to force the aerodynamic centre aft for stability. With the larger propeller, the Flying Model optimal designs featured a 10-25% increase in wing sweep compared to the smaller propeller. The larger propeller had a drastic effect on the GenMAV wing sweep, increasing from a 10 degree forward sweep with the 5 inch propeller to a 40-50 degree backwards sweep (change of 500-600%). The maximum L/D GenMAV and Flying Wing models with varying propellers are presented in Figures 5.43 and 5.44. As shown, increasing the slipstream strength and size corresponds to significant changes in optimal wing sweep and root chord size. A larger propeller creates a stronger slipstream which results in a larger wing sweep to maintain longitudinal stability. The GenMAV models also featured smaller horizontal and vertical stabiliser with propeller effects.

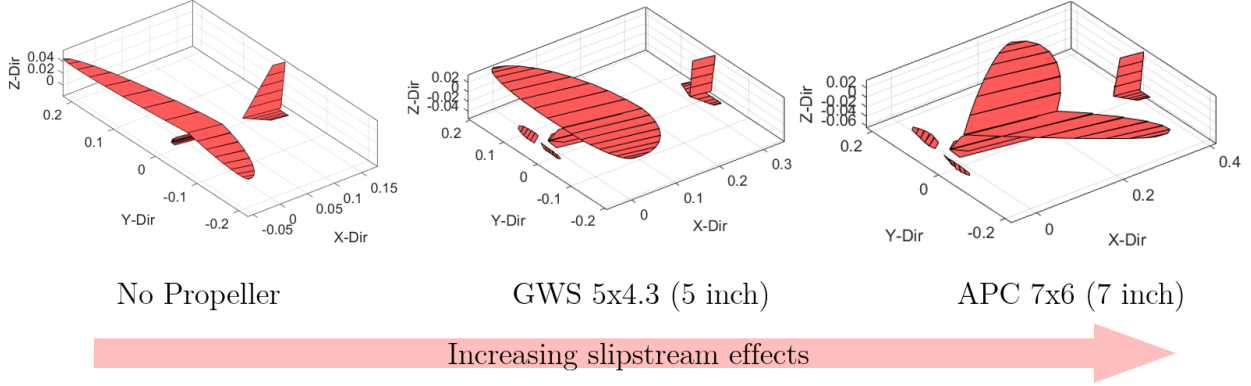


Figure 5.43: Optimal (Max L/D) designs for the 45cm GenMAV class with varying propeller models.

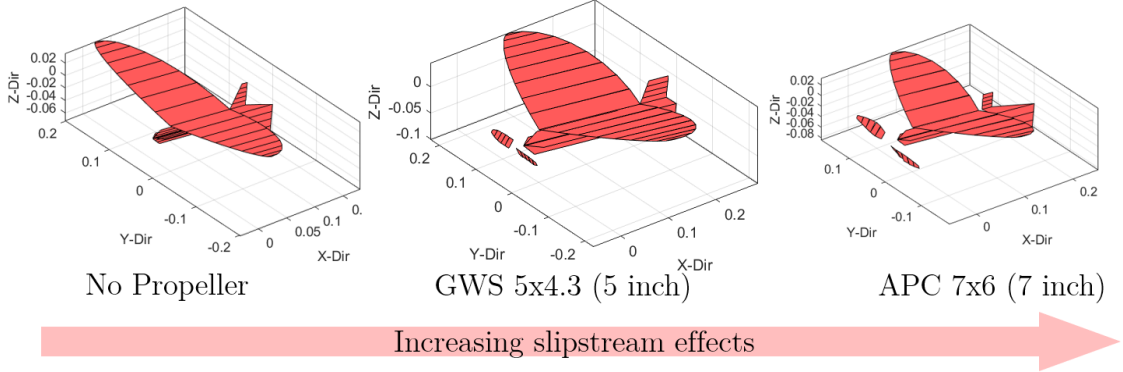


Figure 5.44: Optimal (Max L/D) designs for the 45cm Flying Wing class with varying propeller models.

5.4.3 30 cm Class with 4 inch propeller

The 30 cm size class was optimised with a 4 inch GWS4x4 propeller as shown in Figures 5.45 and 5.46. For this class, optimising including propeller effects produces optimal designs with L/D ratios 10% lower for the Flying Wing design and 20% lower for the Winglets configuration, compared to the optimal designs not including propeller. The reduction in maximum L/D with the addition of propeller is 25% less for the 30cm class than it is for the 45 cm class. This can be attributed to the propeller wash increasing the local Reynolds number and improving wing performance. Results from Ananda et al (2018) suggest that performance benefits can be gained in propeller-wing systems at $\text{Re} < 10^5$ due to the propeller wash diminishing detrimental low Reynolds number effects. These results are confirmed here.

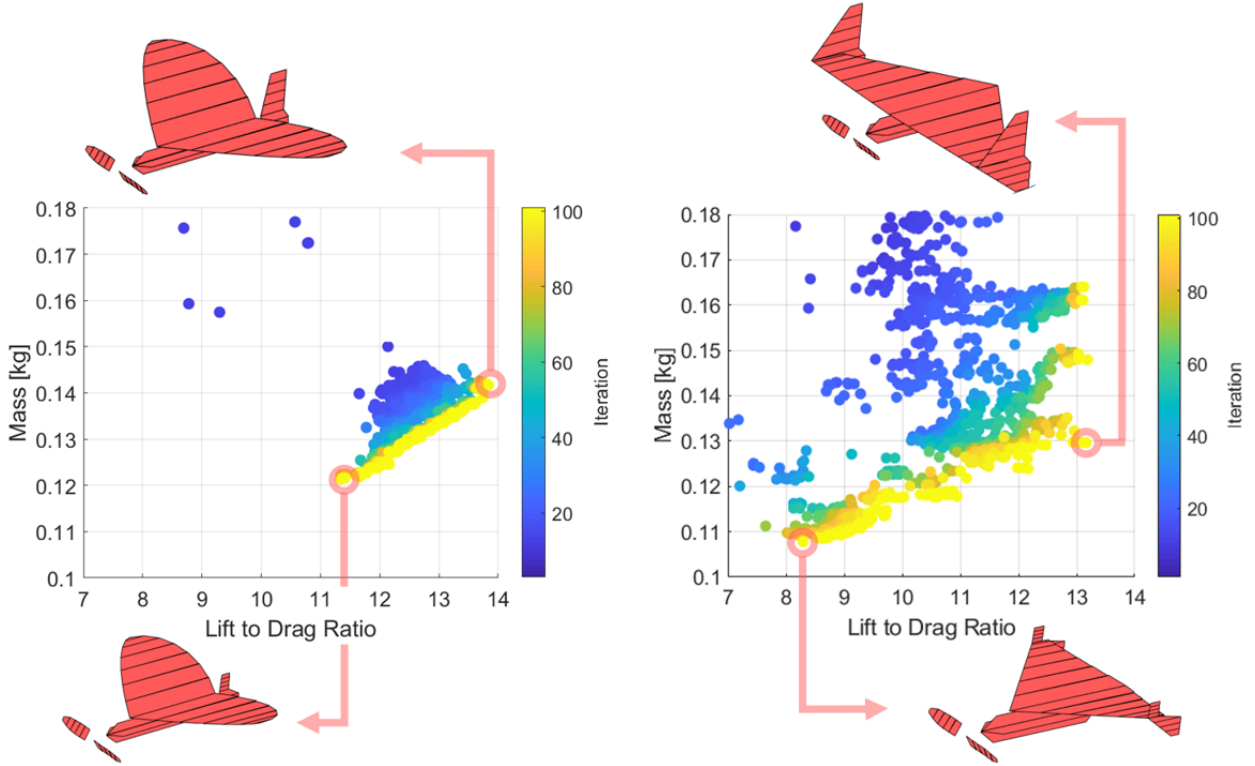


Figure 5.45: Iteration history of the 30cm Flying Wing including propeller.

Figure 5.46: Iteration history of the 30cm Winglets including GWS 4x4

The minimum mass model experiences the lowest Reynolds numbers and benefits the most from the propeller wash. The minimum mass model for the Flying Wing showed a 24% increase in L/D with the inclusion of propeller. Overall, the Winglet configuration performs well with propeller effects, featuring a flatter Pareto front, meaning a smaller mass penalty is incurred for increases in L/D . With the vertical stabiliser moved to the wingtips, out of the propeller wash influence, the Winglet configuration incurs a smaller drag increase with the addition of propeller. The maximum L/D Winglet model produces a higher L/D than the Flying Wing design of the same weight. Optimisation without propeller suggests that the Flying Wing and Winglet designs perform equally. However, with the addition of propeller slipstream in the optimisation, it is clear the Winglet configuration is more desirable.

Unlike the Flying Wing case, the Winglets optimisation features four main optimisation pathways, each defined by a relatively constant wing sweep, as shown in Figures 5.13 and 5.48. In the top right of Figure 5.48 is the high sweep designs with high L/D . This

is the design space that most of the propeller optimisations find optimal. The Winglets optimisation finds an optimisation pathway with low wing sweep, shown in the dark blue. These models produce similar L/D as the high sweep designs, except with a lower wing area and mass. The lowest mass models featured the highest sweep, shown in yellow. The fourth design group was a compromise between the small, high sweep models and the maximum L/D models, shown in the medium blue. These distinct design pathways are also shown in the wing dihedral shown in Figures 5.49 and 5.50.

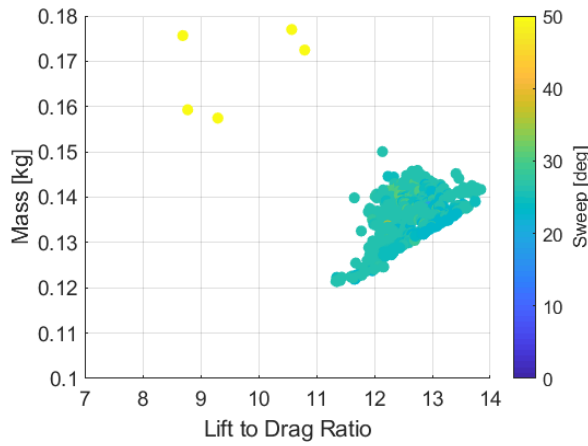


Figure 5.47: 30 cm Flying Wing with 4" prop: Sweep

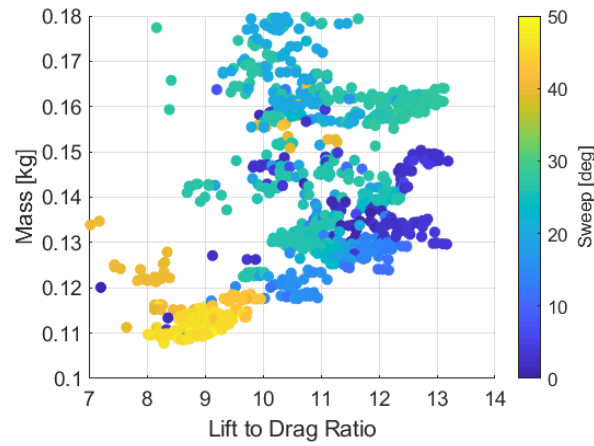


Figure 5.48: 30 cm Winglet with 4" prop: Sweep

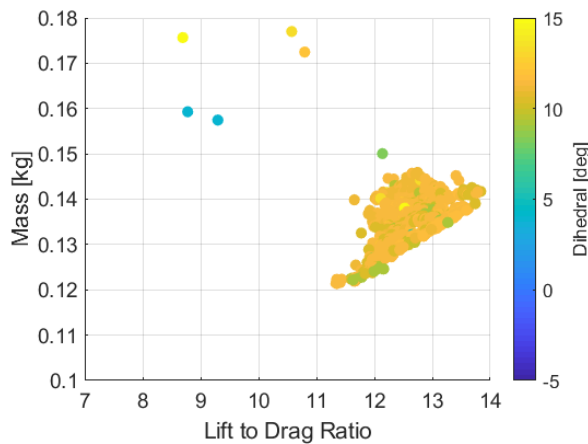


Figure 5.49: 30 cm Flying Wing with 4" prop: Dihedral

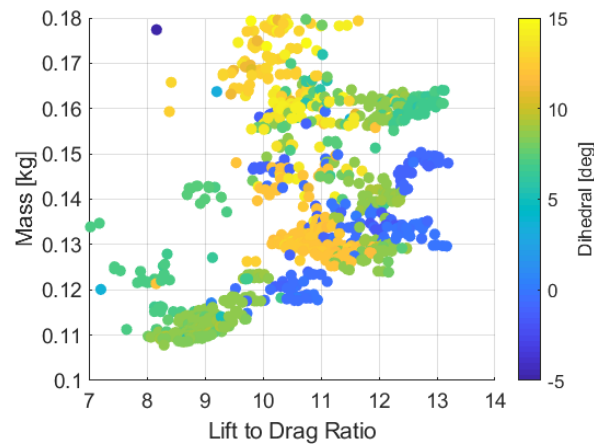


Figure 5.50: 30 cm Winglet with 4" prop: Dihedral

The FlyingWing optimisation found a dihedral of 11-12 degrees most optimal, a 2-3 degree

decrease compared to the optimisation without propeller. The Winglets configuration dihedral angle varied with the wing sweep. In general, higher dihedral angles were found desirable with larger wing sweep, similar to the optimisation without propeller. Wing taper was not correlated with sweep unlike the optimisation with propeller as shown in Appendix C, Figure C.3. Higher aspect ratios produced higher L/D ratios shown in Figure C.4.

5.5 Variable Correlation

By studying the correlation of variables with objectives, we can investigate the high-level design trends in the optimisation. Comparing the variable correlations with and without propeller included in the optimisation will give us an understanding of the importance of including propeller effects in MAV optimisation. Figures 5.51 to 5.54 present the Pearson correlation coefficients of optimisation variables with L/D , mass and stability derivatives. A coefficient of +1 refers to a perfectly positive linear relationship and -1 refers to a perfectly negative correlation. Values in between indicate the level of correlation, with a value of 0 indicating no correlation. The coefficients were calculated from the final five generations of the 30cm Flying Wing and 45cm GenMAV optimisations with and without propeller. Some correlations remain constant throughout all optimisations. For example, the aspect ratio and root chord remain highly correlated with both MAV mass and L/D .

With the addition of propeller into the optimisation, the variable correlations are altered, especially the correlations with stability derivatives. Without propeller, both the Flying Wing and GenMAV configurations show positive correlations between wing sweep and pitch stiffness C_{m_α} . However, when optimised with propeller, this correlation changes (From +0.88 to +0.05 for Flying Wing and +0.28 to -0.27 for GenMAV). As well as this, the correlations of sweep with L/D , mass and C_{l_β} are all altered with the inclusion of propeller in the optimisation. Furthermore, after including propeller, the strong negative correlation between root chord and C_{m_α} is removed.

The multi-variate, multi-objective nature of the optimisation means that these correlations values need to be considered carefully, as not all variables have been presented. However,

across all configurations and size classes (see Appendix C for the 45cm Flying Wing correlations) there are clear effects on variable correlation when including propeller slipstream in the optimisation. These changes appear to be particularly strong in the static stability correlations.

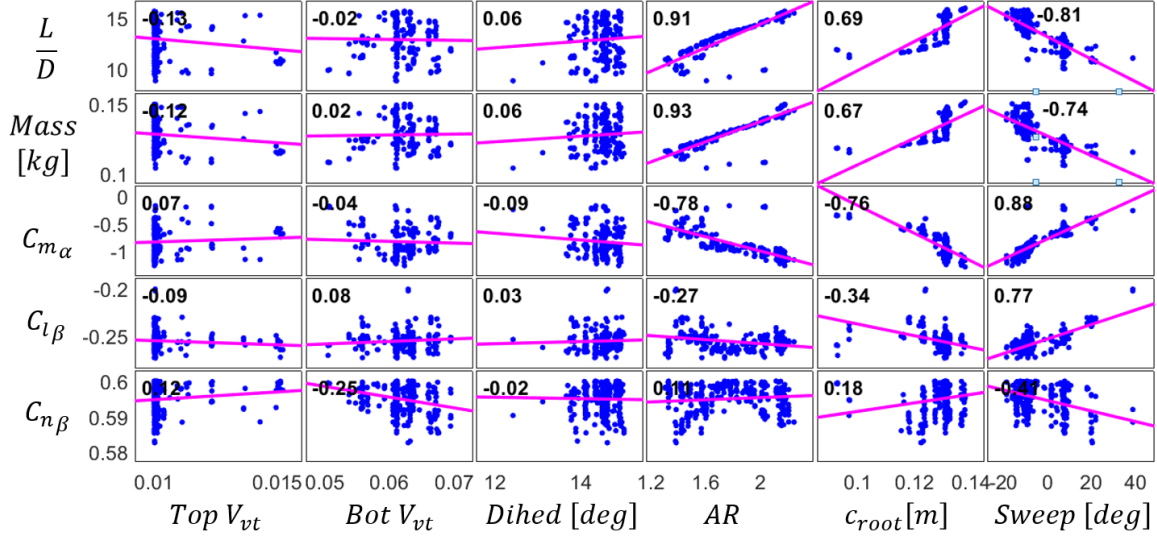


Figure 5.51: Variable correlations for the 30cm Flying Wing optimisation without propeller

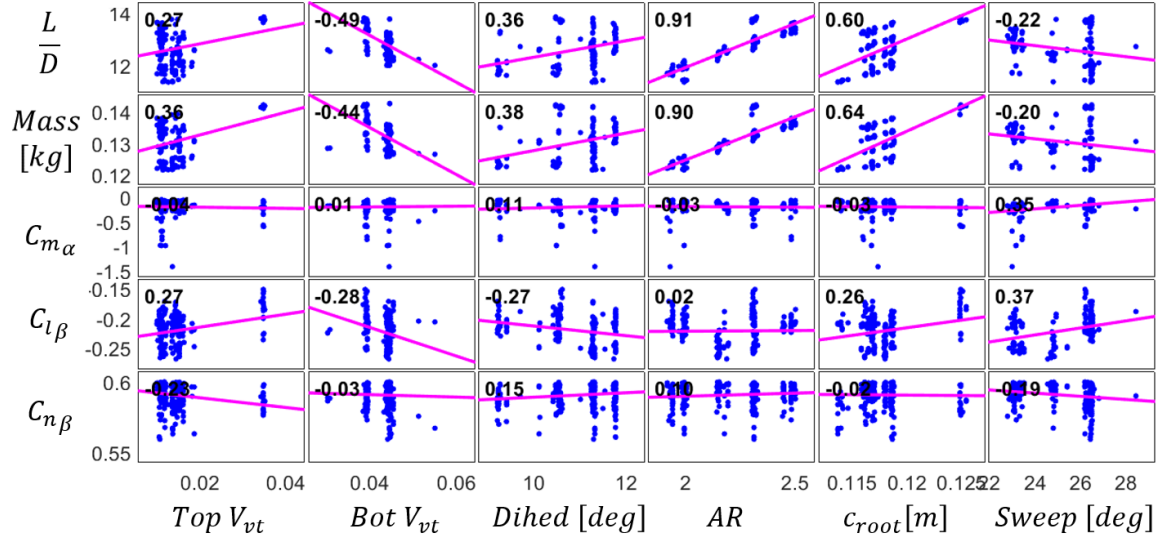
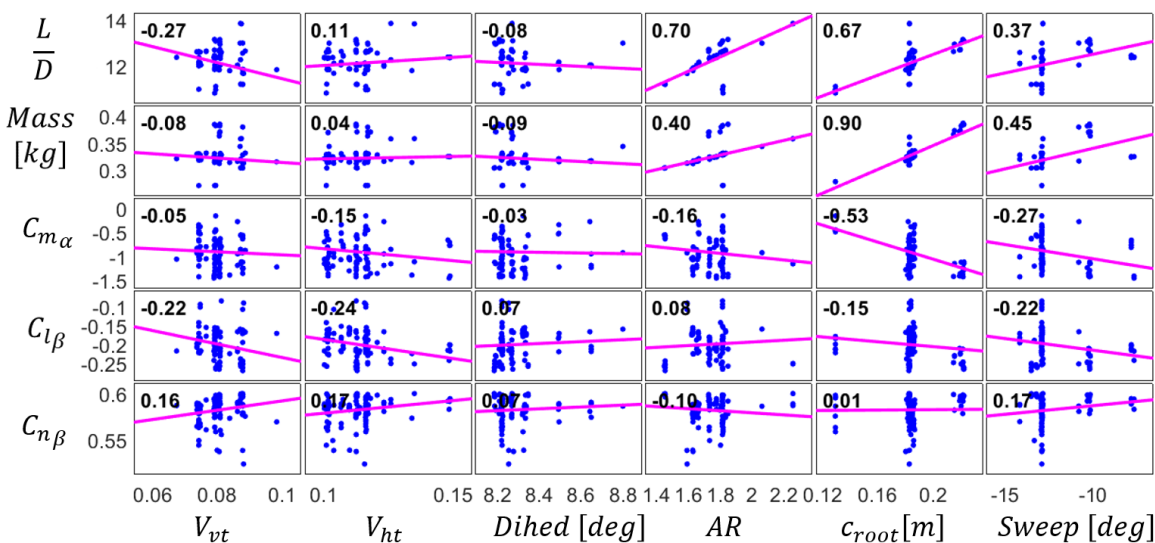
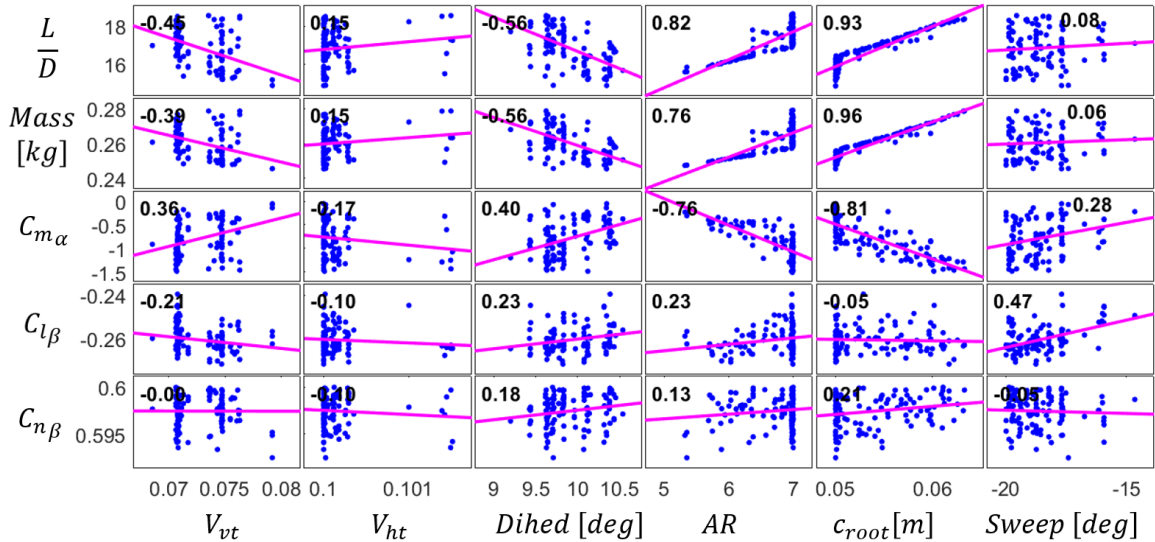


Figure 5.52: Variable correlations for the 30cm Flying Wing optimisation with 4" propeller



Chapter 6

Conclusions and Future Work

This chapter concludes the thesis, summarizing the primary achievements and conclusions, before providing future work suggestions. The key results from Sections 5.3 and 5.4 are summarized in Section 6.1. Finally, section 6.2 outlines potential paths for further research.

6.1 Conclusions

Interest in Micro UAVs has increased over the past decade with the miniaturisation of micro-controllers and propulsion systems. With MAV performance improving rapidly, the demand for early stage design optimisation is increasing. MAV optimisation is complicated by the challenge of predicting aerodynamic forces at low Reynolds numbers. Non-linear lift distributions and laminar separation bubbles, consequences of low Reynolds numbers, require robust potential flow methods or RANS CFD programs to accurately model. While several recent studies have explored MAV optimisation, none of these include propeller slipstream effects. Propeller wash changes the flow conditions experienced by the wing and empennage, altering the aerodynamics and stability of the MAV. This thesis investigated the effect of propeller slipstream on MAV optimisation.

A Higher Order Free Wake (HOFW) potential flow method was used to model the aerodynamic forces of the MAVs. This solver was integrated with a Non-dominated Sorting Genetic Algorithm (NSGA II) to generate optimal MAV designs. A numerical longitudinal and lateral stability function was successfully developed and validated. The stability function was used to constrain the optimisation to aerodynamically stable MAV designs. Three common MAV configurations (Flying Wing, GenMAV and Winglets) and two size classes (30cm and 45cm) were optimised without propeller. These MAV classes were optimised again including

a tractor propeller. The key conclusions from these investigations are presented below:

- The optimisation without propeller developed optimised MAVs with performance similar-to or better-than published MAV designs from literature. Optimal aerodynamic designs featured a higher wing area and larger aspect ratio than the minimum mass designs.
- For the optimisation without propeller, significant performance improvements were seen with increased Reynolds number. The 45cm class ($Re 1.6 \times 10^5$) produced maximum lift-to-drag ratios 20-30% higher than the 30 cm class ($Re 1.0 \times 10^5$).
- The correlation of optimisation variables with performance objectives showed that high aspect ratio wings with a forward sweep were most desirable for the optimisation without propeller. A combination of wing dihedral and empennage size was used to meet stability constraints.
- The feasibility of implementing propeller modelling into MAV optimisation was confirmed. However, care must be taken to ensure force prediction from the propeller slipstream converges sufficiently.
- The optimisation with propeller produced significantly different optimal MAV designs to the optimisation without propeller. The optimal designs produced higher L/D ratios compared to published results that include propeller effects.
- As predicted by literature, the addition of propeller reduced the maximum lift-to-drag ratios by 25-35%. Furthermore, for the 30cm class, the reduction in lift-to-drag ratio was 25% lower than the 45cm class.
- Including a propeller reduced the longitudinal stability of the MAV. As a result the optimal solutions featured a 20-40% increase in wing sweep compared to the optimisation without propeller.
- The correlation of geometric variables with performance objectives changes with the addition of a propeller. Increased aspect ratio and root chord remained correlated with lift-to-drag ratio and mass. However, the influence on these variables on stability derivatives was altered. Wing sweep also influenced pitch stability less as the propeller

slipstream skewed the lift distribution towards the wing root.

- Considering the significant effects of the propeller on MAV aerodynamics and stability, optimisations without propeller effects must be considered incomplete. As the influence of geometric variables on MAV performance changes with the inclusion of a propeller, it is important that propeller slipstream is included in MAV optimisation.

6.2 Future Work

Based off the conclusions of this thesis, a number of potential pathways for future research are presented below:

- Experimental wind tunnel testing could provide further validation to the aerodynamic and stability effects of propeller slipstream on MAVs.
- Whilst this paper used L/D as the primary performance objective, more advanced performance objectives could be integrated into the optimiser. MAV range or endurance could be estimated using a more detailed model of the propulsion system and battery capacity. This would allow MAVs to be optimised directly for specified mission requirements.
- The addition of propeller geometry and location variables could be used to develop MAV wing planform and propeller designs optimised for each other. Varying the propeller location could investigate the aerodynamic effects of a tractor configuration compared to a pusher configuration.
- The inclusion of dynamic stability constraints to limit feasible designs to those with favourable modal dynamics.
- Although optimisation with propeller effects is feasible, it is computationally expensive compared to optimisation without propeller. Integrating the optimiser with a surrogate modelling function could drastically reduce the number of required optimisation generations. This would also allow the VAP 3.5 solver to be run for longer, ensuring convergence.

References

- Albertani, R., Hubner, P., Ifju, P., Lind, R. and Jackowski, J. 2004. Wind tunnel testing of micro air vehicles at low Reynolds numbers. World Aviation Congress and Exhibition.
- Ananda, G., Selig, M. S. and Deters, R.W. 2018. Experiments of propeller-induced flow effects on a low-Reynolds-number wing. AIAA Journal, 56.
- Bramesfeld, G. 2006. A higher-order vortex lattice method with a force-free wake. PhD Thesis. College of Engineering, Pennsylvania State University.
- Brandt, B. 2005. Small-scale propeller performance at low speeds. Masters of Science Thesis, Department of Aerospace Engineering, University of Illinois at Urbana-Champaign..
- Bronz, M., Moschetta, J.M., Brisset, P. and Gorraz, M. 2009. Towards a long endurance MAV. International Journal of Micro Air Vehicles, 1.
- Campbell, L. 2020. Computational optimisation analysis of MAV wing designs. Honours Thesis. School of Aerospace, Mechanical and Mechatronic Engineering, The University of Sydney.
- Carmichael, B. 1981. Low Reynolds number Airfoil survey, volume 1. National Aeronautics and Space Administration. Contractor Report (CR).
- Chen, Y. 2016. Numerical optimisation. Aarhus University of Denmark.
[www.jade-cheng.com/au/coalhmm/optimization/.](http://www.jade-cheng.com/au/coalhmm/optimization/)
- Chen, Z.J. and Qin, N. 2013. Planform for low-Reynolds-number thin wings with positive and reflex cambers. Journal of Aircraft, 50.

Chen, M and Hubner, J. 2021. Experimental investigation of wing-on-rotor effect at low disk loading and Reynolds number. *Journal of Aircraft*. 58.

Chinwicharnam, K. and Thipyopas, C. 2016. Comparison of wing-propeller interaction in tractor and pusher configuration. *International Journal of Micro Air Vehicles*, 8.

Cole, J. 2016. A higher-order free-wake method for aerodynamic performance prediction of propeller-wing systems. The Pennsylvania State University Graduate School. Dissertation in Aerospace Engineering.

Cole, J., Maughmer, M. D., Kinzel, M. and Bramesfeld G. 2019. Higher-order free-wake method for propeller-wing systems. *Journal of Aircraft*. 56.

Cosyn, P. and Vierendeels, J. 2007. Design of fixed wing micro air vehicles. *Aeronautical Journal*, 111.

Cosyn, P. and Vierendeels, J. 2006. Numerical investigation of low-aspect-ratio wings at low Reynolds numbers. *Journal of Aircraft*. 43.

Deters, R.W. 2014. Performance and slipstream of small-scale propellers at low Reynolds numbers. Ph.D. Thesis, Department of Aerospace Engineering, University of Illinois.

Drela, M. 1988. Low-Reynolds-number airfoil design for the M.I.T. Daedalus prototype - A case study. *Journal of Aircraft*. 25.

Drela, M. 1989. XFOIL: An analysis and design system for low-Reynolds-number airfoils. Low-Reynolds-number aerodynamics. 54.

Dunsby, J. Currie, M. and Wardlaw, R. 1959. Pressure distribution and force measurements on a VTOL tilting wing-propeller model. NRC LR-255.

Durai, A., Dodamani, R., Antony, R., Chitlur, S., Gopalan, R. and Ahmed, S. 2011. Experimental studies on a propelled micro air vehicle. 29th AIAA Applied Aerodynamics Conference.

Farah, S. 2019. Aerodynamic design and multi-objective optimisation of MAV wings. Honours Thesis. School of Aerospace, Mechanical and Mechatronic Engineering, The University of Sydney.

Ferraro, G. Kipouros, T. Savill, M. Rampurawala, A. and Agostineli, C. 2014. Propeller-wing interaction prediction for early design. 52nd Aerospace Sciences Meeting.

Franke, A. and Weinig, F. 1939. The effect of the slipstream on an airplane wing. National Advisory Committee for Aeronautics. Technical Memorandums, No. 920.

Gamble, B.J. and Reeder, M.F. 2009. Experimental analysis of propeller-wing interactions for a micro air vehicle. Journal of Aircraft, 46.

Hassanalian, M. and Abdelkefi, A. 2017. Design, manufacturing, and flight testing of a fixed wing micro air vehicle with Zimmerman planform. Meccanica, 52.

Hassanalian, M., Khaki, H. and Khosravi, M. 2014. A new method for design of fixed wing micro air vehicle. Journal of Aerospace Engineering, 229.

Hassanalian, M., Quintana, A. and Adelkefi, A. 2018. Morphing and growing micro unmanned air vehicle: Sizing process and stability. Aerospace Science and Technology, 78.

Jana, S., Kandath, H., Shewale, M., and Bhat, M.S. 2019. Effect of propeller-induced flow on the performance of biplane micro air vehicle dynamics. Journal of Aerospace Engineering, 234.

Johnson, R., Witkowski, D. and Sullivan, J. 1991. Experimental results of a propeller/wing interaction study. SAE International Journal of Aerospace, 100.

Kleinstein, G. and Liu, C. H. 1972. Application of airfoil theory for nonuniform streams to wing propeller interaction. Journal of Aircraft, 9.

Kroo, I. 1986. Propeller-wing integration for minimum induced loss. Journal of Aircraft, 23.

Kuzmina, S., Ishmuratov, F., Zichenkov, M., Chedrik, V., Amiryants, G.A. and Kulesh, V. 2018. Morphing wing technologies. in Wind tunnel testing of adaptive wing structures, Butterworth-Heinemann.

Lissaman, P.B.S. 1983. Low-Reynolds-number airfoils. Annual Review of Fluid Mechanics 15.

McMasters, J. H. and Henderson, M. L. 1980. Low-speed single-element airfoil synthesis. Technical Soaring. 6.

Miranda, L.R. and Brennan, J.E. 1986. Aerodynamic effects of wing tip mounted propellers and turbines, AIAA Journal. 86.

Mueller T. 1985. Low-Reynolds-number vehicles. Advisory Group for Aerospace Research and Development, E Reshotko.

Mueller, T. and DeLaurier, J. 2003. Aerodynamics of small vehicles. Annual Review of Fluid Mechanics. 35.

Mueller, T. 2007. Introduction to the designs of fixed-wing micro air vehicles: including three case studies. American Institute of Aeronautics & Astronautics.

Mueller, T. and Pelletier, A. 2000. Low-Reynolds-number aerodynamics of low-aspect-ratio, thin/flat/cambered-plate wings. *Journal of Aircraft*. 37.

Null, W., Noseck, A., and Shkarayev, S. 2005. Effects of propulsive-induced flow on the aerodynamics of micro airvehicles. 23rd AIAA Applied Aerodynamic Conference.

Null, W. and Shkarayev, S. 2005. Effect of camber on the aerodynamics of adaptive-wing micro air vehicles. *Journal of Aircraft*. 42.

Roberts, W. 1980. Calculation of laminar separation bubbles and their effect on airfoil performance. *Journal of Aircraft*. 18.

Ryder, J. 2020. Aerodynamic optimisation of mini aerial vehicles. Honours Thesis. School of Aerospace, Mechanical and Mechatronic Engineering, The University of Sydney.

Raymer, D. 2006. Aircraft design: a conceptual approach. American Institute of Aeronautics and Astronautics. Virginia, VA.

Roskam, I. 2000. Airplane Design. DAR Corporation, Lawrence, Kansas.

Schmitz, F. W. 1970. Aerodynamics of the model airplane. Part 1, Airfoil measurements. NTIS. Springfield, VA.

Shams, T., Shah, S., Shahzad, A., Javed, A. and Mehmod, K. 2020. Experimental investigation of propeller-induced flow on flying wing micro aerial vehicle for improved 6DOF modeling. IEEE. 66.

Shkarayev, S., Moschetta, J., and Bataille, B. 2008. Aerodynamic design of micro air vehicles for vertical flight. *Journal of Aircraft*, 45.

Stewart, K., Wagener, J., Abate G., and Salichon, M. 2007. Design of the Air Force research laboratory micro aerial vehicle research configuration. 45th AIAA Aerospace Sciences Meeting and Exhibit.

Sudhakar, S., Kumar, C., Arivoli, D., Dodamani, R., and Venkatakrishnan, L. 2013. Experimental studies of propeller induced flow over a typical micro air vehicle. 51st AIAA Aerospace Sciences Meeting and Exhibit.

Thipyopas, C. and Moschetta, J. 2006. Comparison plusher and tractor propulsion for micro air vehicle applications. SAE Technical Paper 2006-01-2397.

Traub, L., and Lawrence, J. 2009. Aerodynamic characteristics of forward and aft swept arrow wings. Journal of Aircraft, 46.

Trips, D. 2010. Aerodynamic design and optimization of a long-range mini-UAV. Masters of Science Thesis. Faculty of Aerospace Engineering, Delft University.

Van Magill, B. 2016. Rapid prototyping and innovation in micro autonomous aerial system design. Honours Thesis. School of Aerospace, Mechanical and Mechatronic Engineering, The University of Sydney.

Velduis, L. 2004. Review of propeller wing aerodynamic interference. International Council of the Aeronautical Sciences. 65.

Veldhuis, L., Stokkermans, T., Sinnige, T., and Eitelberg, G. 2016. Analysis of swirl recovery vanes for increased propulsive efficiency in tractor propeller aircraft. 30th Congress of the International Council of the Aeronautical Sciences. 60.

Winslow, J., Otsuka, H., Govindarajan, B. and Chopra, I. 2018. Basic understanding of airfoil characteristics at low Reynolds numbers. *Journal of Aircraft*. 55.

Witkowski, D., Johnston, R. and Sullivan, J. 2012. Propeller/wing interaction. 27th Aerospace Sciences Meeting.

Wortmann, F. X. 1974. Airfoil design for man powered aircraft. Massachusetts Institute of Technology, Low Speed Symposium.

Xue, C. and Zhou, Z. 2020. Propeller-wing coupled aerodynamic design based on desired propeller slipstream. *Aerospace Science and Technology*. 97.

Yusoff, Y., Ngadiman, M. and Zain, A. 2011. Overview of NSGA-II for optimizing machining process parameters. *Procedia Engineering*, 15.

Zimmerman, C. 1936. Aerodynamic characteristics of several airfoils of low aspect ratio. National Advisory Committee for Aeronautics, Technical Note No. 539.

Appendix A

Relevant Theory

This chapter outlines the fundamental concepts, theories and nomenclature that will be used throughout this thesis. Firstly, aircraft geometry and reference frames will be defined. This will be followed by an outline of the aerodynamic forces and linear approximations used. Finally, the static longitudinal and lateral stability of an aircraft is described and stability criteria are defined.

A.1 Reference Frames

Aircraft motion is defined with respect to multiple sets of axes. Figure A.1 shows the relationship between the reference frames.

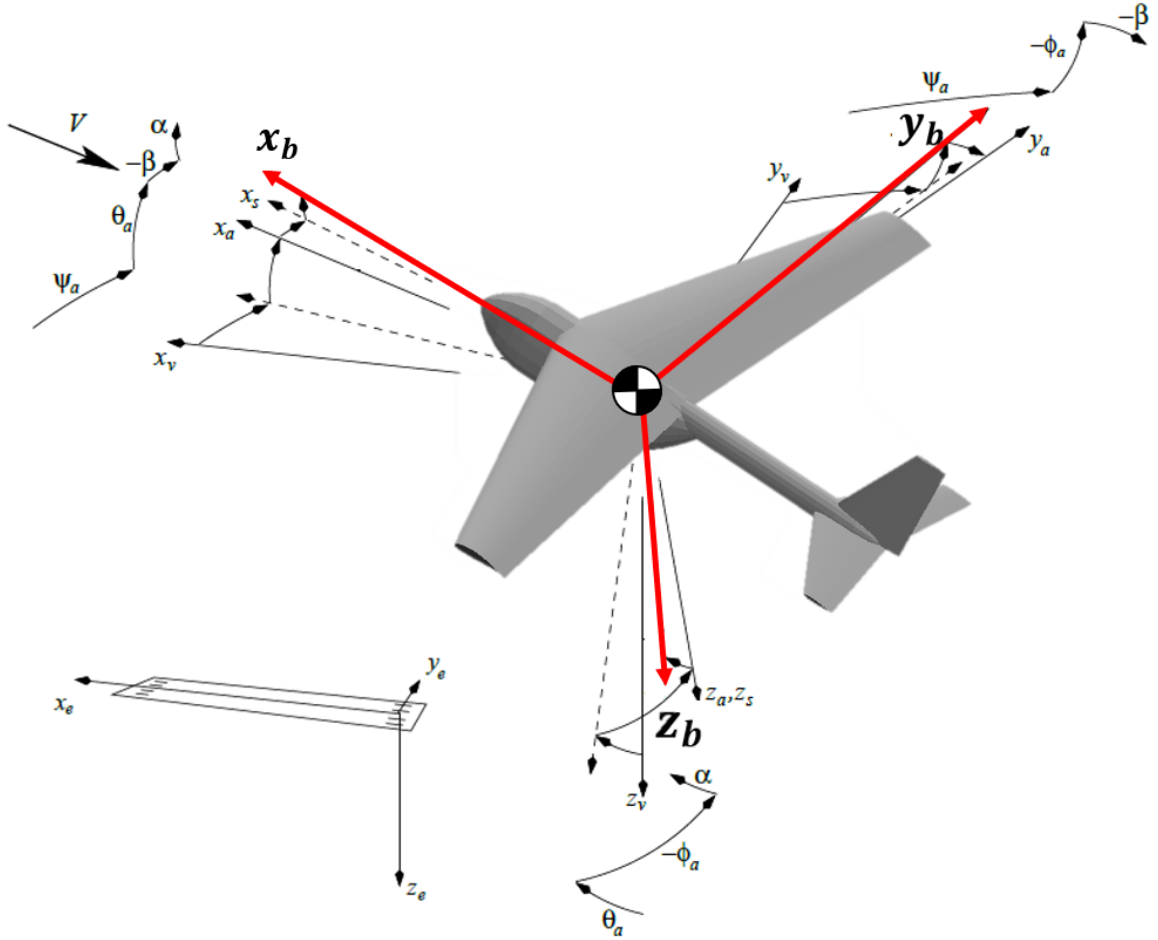


Figure A.1: Relationship between aircraft reference frames

The five primary axes systems used to define aircraft motion and position in Figure A.1 are described below:

- **Earth Axes (x_e, y_e, z_e):** Primarily used to represent aircraft position. The Earth axes estimate an inertial reference frame (non accelerating or rotating axes) attached to Earth surface. The x_e axis points North, y_e points East and z_e points downward towards the centre of the Earth.
- **Local-Vertical, Local-Horizontal LVLH Axes (x_v, y_v, z_v):** Translates with aircraft, with origin at centre of gravity. Axes aligned with the Earth axes.
- **Body Axes (x_b, y_b, z_b):** Translates with aircraft, with origin at centre of gravity. x_b is aligned with fuselage reference line, pointing towards nose. y_b is aligned through right

hand wing and z_b points downwards.

- **Stability Axes** (x_s, y_s, z_s): Translates with aircraft, origin at centre of gravity. x_s is aligned with the relative air path , offset from x_b by the angle of attack α . y_s is aligned with y_b and z_s perpendicular to x_s, y_s .
- **Air Path Axes** (x_a, y_a, z_a): Translates with aircraft, origin at centre of gravity. x_a, y_a are aligned to the relative air path, offset from x_b, y_b by the angle of attack α and sideslip angle β respectively. z_a defined perpendicular to x_a, y_a .

The angles between the reference frames are key parameters required to define aircraft motion. These angles can be broken into two key categories:

- **Aerodynamic Angles** (α, β): The aerodynamic angles represent the offset between the aircraft body axes and the relative air path. The angle of attack α is the offset between x_b and x_a . The side slip angle β is the offset between y_b and y_a . These angles are crucial for determining the aerodynamic performance of the aircraft. As the direction of the air flow changes relative to the aircraft body, the aerodynamic forces change significantly.
- **Euler Angles** (θ_a, ϕ_a, ψ_a): The Euler angles define the aircraft translation direction in pitch θ_a , yaw ψ_a and roll ϕ_a . These angles are the offset between the air path and LVLH reference frames.

A.2 Aircraft Geometry

Throughout this thesis several geometric parameters will be used to define aircraft models. Figure A.2 illustrates some of the key geometric parameters.

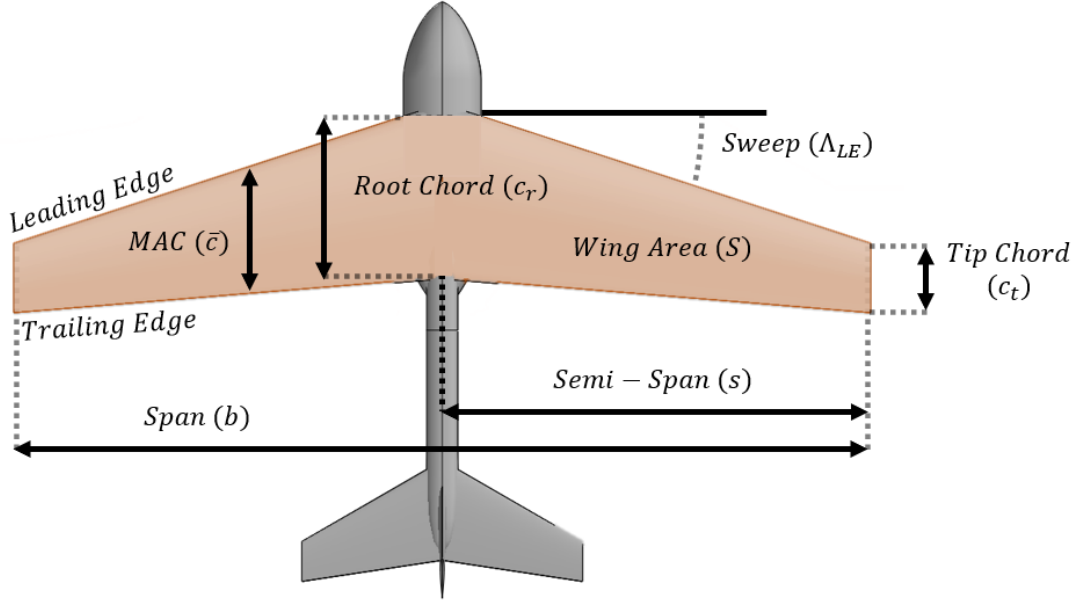


Figure A.2: Key aircraft geometric parameters

Span

Wingspan b is the distance between wingtips. The semi-span s is distance between the wing tip and the Fuselage Reference Line (FRL), representing the length of one side of the wing. For swept back wings, such as the model shown in Figure A.2, the span is measured by the distance between tips in y_b , not the distance along the leading or trailing edge.

Chord

The distance in x_b between the wing leading and trailing edge is the chord of the wing. It is common for the chord to change along the wing span, requiring definitions for root chord c_r and tip chord c_t . For a rectangular wing, the ratio between the tip chord and root chord is known as the taper ratio λ where:

$$\lambda = \frac{c_t}{c_r} \quad (\text{A.1})$$

The taper ratio is used to influence the spanwise lift distribution and reduce the outboard wing area to reduce the structural moment at the wing root. The Mean Aerodynamic Chord (MAC) is a useful parameter which is used to represent the entire wing in two dimensions. The MAC is the chord length where the resultant aerodynamic wing force acts through. The

MAC can be found using the relationship:

$$\bar{c} = \frac{\int_0^b c(y)^2 dy}{\int_0^b dy} \quad (\text{A.2})$$

For a straight tapered wing with root chord c_r and taper ratio λ the MAC can be simplified:

$$\bar{c} = \frac{2c_r(1 + \lambda + \lambda^2)}{3(1 + \lambda)} \quad (\text{A.3})$$

Aspect Ratio

For a rectangular wing, the aspect ratio (AR) is the ratio of the wingspan to mean chord. High aspect ratios indicate the wings are long and thin whilst low aspect ratios indicate the wings are short and wide as shown in Figure A.3.

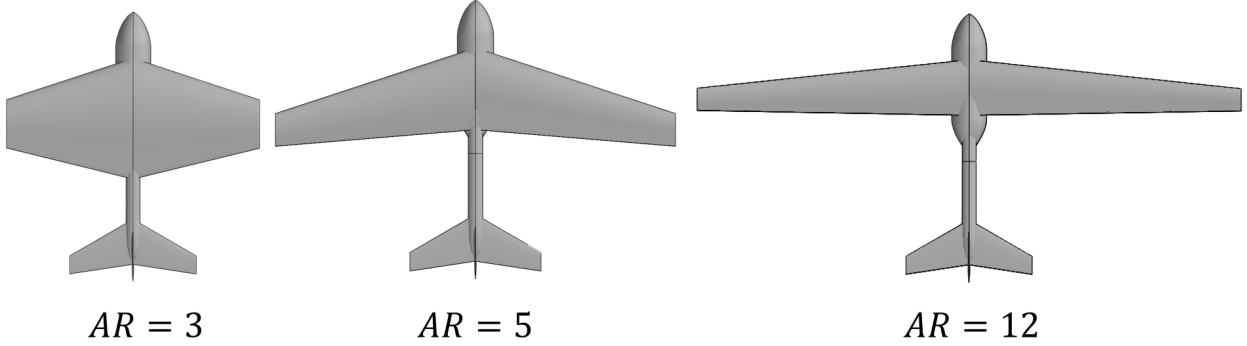


Figure A.3: Low, medium and high aspect ratio wings with constant wing area S

More generally, the wing aspect ratio can be found using equation A.4. Where b is the wingspan and S is the wing area.

$$AR = \frac{b^2}{S} \quad (\text{A.4})$$

The wing aspect ratio is an important parameter for aerodynamic efficiency. High aspect ratio wings produce less lift-induced drag. However, high aspect ratio wings have a higher surface area and are often heavier, requiring more structural support.

Sweep

Leading edge wing sweep Λ_{LE} is the angle between the y_b axis and leading edge. Positive

wing sweep (swept back wings) directs airflow outboard along the leading edge, changing the experienced angle of attack of the wing tips. Negative sweep creates inboard airflow, directing air to the root chord. At high Mach numbers ($M > 0.8$) wing sweep is used to reduce wave drag from supersonic shock waves. For subsonic aircraft this effect is negligible.

Wing sweep is also an important parameter for static longitudinal stability. Positive (negative) sweep pushes the aircraft centre of gravity backwards (forwards). Sweep can be used to tune the pitch stability.

Dihedral

Wing dihedral γ is the angle between the wing and y_b axis as shown in Figure A.4. Positive dihedral is defined such that the wing tip is higher than the wing root.

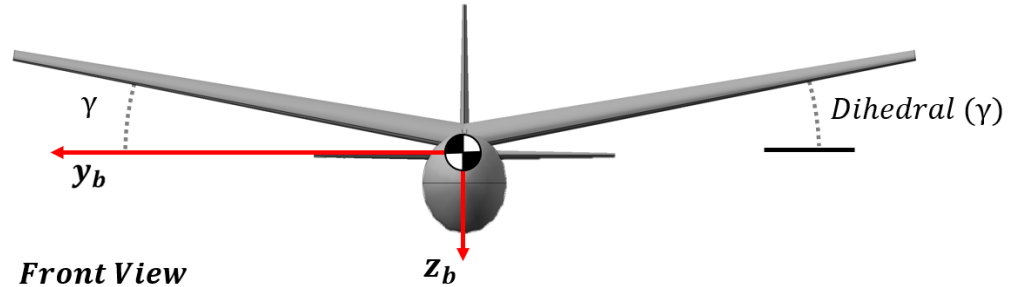


Figure A.4: Example of wing dihedral angle

Wing dihedral redirects the wing normal force laterally, affecting the aircraft roll and yaw dynamics. Dihedral is used to improve the lateral stability of the aircraft.

Twist and Incidence

The wing twist θ_t is the angle between the root chord and tip chord reference lines. Positive twist is defined as twisting down as shown in Figure A.5. Wing incidence (θ_i) is the angle between the root chord line and fuselage reference line, with positive defined as the root chord twisted up.

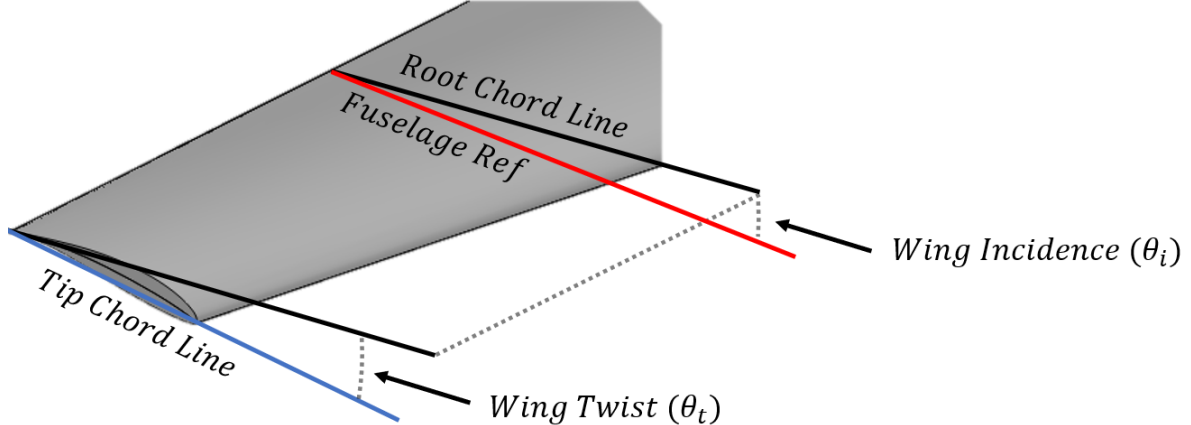


Figure A.5: Example of wing twist and incidence

Wing twist is used to control the wing tip stalling behaviour. The wing tips are usually the first wing section to stall and can cause loss of aileron effectiveness. Twisting the wing tip down defers stall at the tip. Wing incidence is often used to set the wing angle of attack at cruise so that the x_b body axis is aligned with the air path x_a .

A.3 Aerodynamic Forces and Coefficients

When exposed to airflow, a wing will create a pressure differential between the upper and lower surface. The high pressure under side and low pressure upper side generates a normal force perpendicular to the chord line. The aerodynamic centre (AC) is defined as the point through which net aerodynamic forces are applied such that the pitching moment remains constant with angle of attack. This allows us to simplify calculations by assuming the total aerodynamic force acts through a single point. The lift force (L) is the normal force component in the z_a air path axis. The drag force (D) is the resistance of an aircraft to travel through air. Drag is a combination of the normal force component in the x_a air path axis and of the friction between the aircraft surface and the airflow. The aircraft wing, tail and fuselage are the primary bodies that generate aerodynamic forces on an aircraft. The lift and drag force remains orientated with the relative wind as shown in Figure A.6.

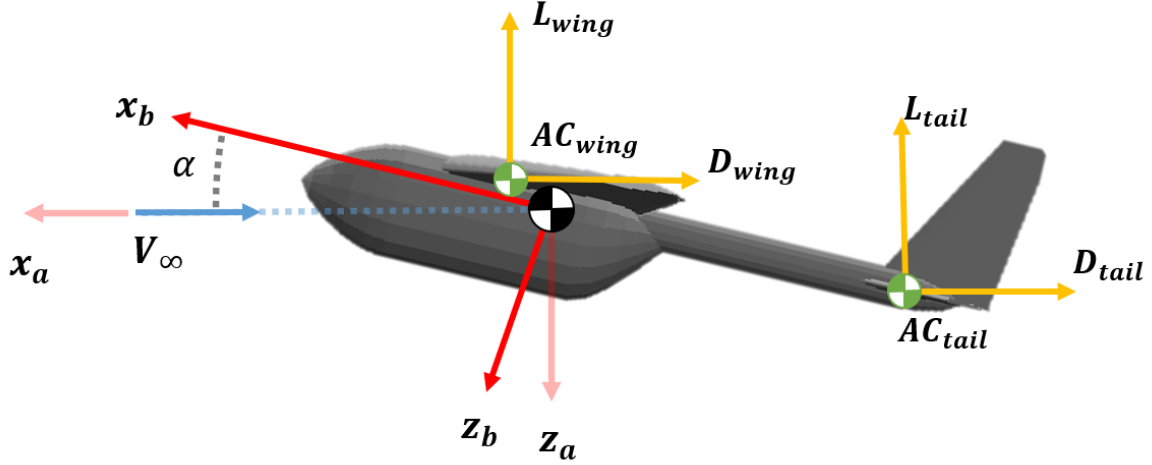


Figure A.6: Diagram of aerodynamic forces acting on aircraft

To understand the aerodynamic characteristics independent of the flow conditions, the lift and drag force are normalised by the free stream dynamic pressure q and wing area S . The resulting lift and drag coefficients are shown in Equations A.5 and A.6.

$$C_L = \frac{L}{qS} = \frac{L}{\frac{1}{2}\rho V_\infty^2 S} \quad (\text{A.5})$$

$$C_D = \frac{D}{qS} = \frac{D}{\frac{1}{2}\rho V_\infty^2 S} \quad (\text{A.6})$$

It is often useful to make approximations for the lift and drag coefficients to simplify analysis. The lift coefficient can be estimated as a function of angle of attack as shown in Equation A.7

$$C_L \approx C_{L_0} + C_{L_\alpha} \alpha \quad (\text{A.7})$$

C_{L_0} is the lift coefficient at zero angle of attack and C_{L_α} is the lift curve slope with respect to angle of attack α . This approximation is very accurate for low angles of attack. However, at high angle of attack C_L becomes non-linear due to flow separation and as a result Equation A.7 is inaccurate. The drag can be estimated as a second order polynomial function of lift coefficient as shown in Equation A.8.

$$C_D \approx C_{D_0} + \frac{C_L^2}{\pi AR e} \quad (\text{A.8})$$

C_{D_0} is the drag due to viscous skin friction and e is the Oswald span efficiency factor, a measure of lift distribution efficiency. The drag proportional to C_L is called the lift-induced drag C_{D_i} . It can be seen that increasing wing aspect ratio decreases C_{D_i} if the Oswald span efficiency factor e is kept constant.

A.4 Static Longitudinal Stability

The static longitudinal stability refers to the pitching moment M response to angle of attack. The pitching moment is the moment about the x_b and can be normalised similar to lift and drag as shown in Equation A.9.

$$C_M = \frac{M}{\frac{1}{2}\rho V_\infty^2 S \bar{c}} \quad (\text{A.9})$$

The derivative of the pitching moment with respect to angle of attack is called the pitch stiffness, shown in Equation A.11

$$C_{M_\alpha} = \frac{\partial C_M}{\partial \alpha} \quad (\text{A.10})$$

For longitudinal stability, a positive angle of attack disturbance must produce a negative change in pitching moment, correcting the aircraft back to equilibrium. In other words, C_{M_α} must be negative for static stability.

$$C_{M_\alpha} < 0 \quad \text{for stability} \quad (\text{A.11})$$

Similar to the wing and tail aerodynamic centres, the aerodynamic centre for the entire aircraft is called the neutral point (N_0 or NP). The net aerodynamic force acting through the neutral point produces no change in pitching moment with changes in angle of attack ($C_{M_\alpha} = 0$ when $x_{cg} = N_0$). When the aircraft centre of gravity coincides with the neutral point, the aircraft is neutrally stable. A schematic of an aircraft highlighting key longitudinal stability parameters is shown in Figure A.7.

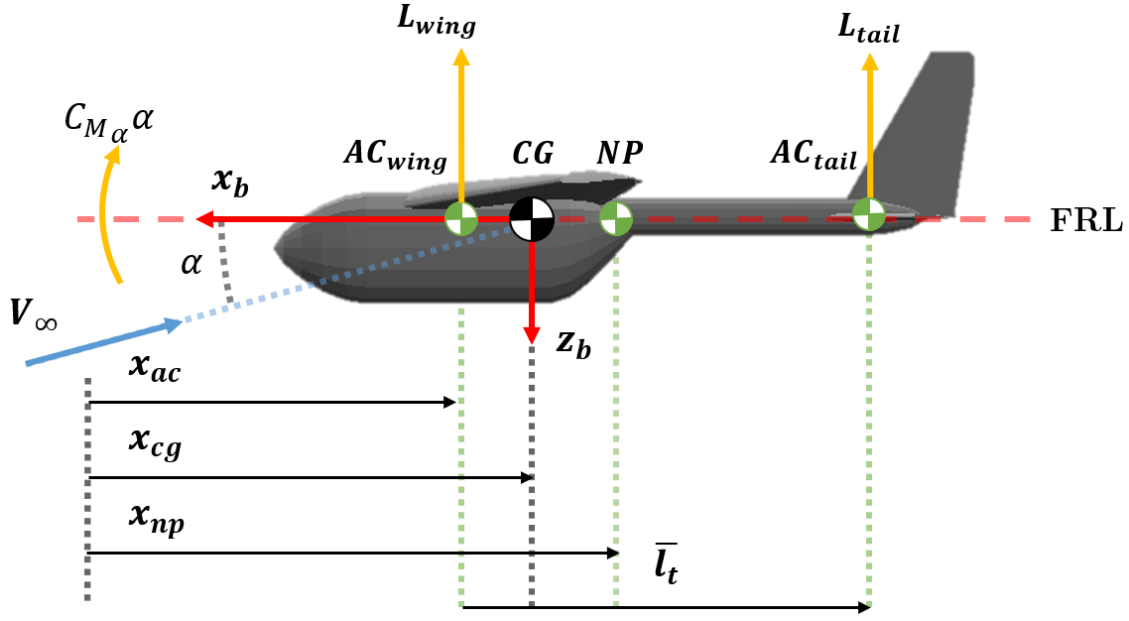


Figure A.7: Location of centre of gravity (CG), neutral point (NP) and aerodynamic centre (AC)

In Equation A.12 the aerodynamic forces around the centre of gravity are balanced. Static margin (distance between centre of gravity and neutral point N_0) is inversely proportional to C_{M_α} .

$$C_{M_\alpha} = C_{L_\alpha} \left(\frac{x_{cg}}{\bar{c}} - N_0 \right) \quad (\text{A.12})$$

If the centre of gravity is pushed too far forward, C_{M_α} becomes very large and negative, creating strong correctional moment for changes in angle of attack. An aircraft in this state is stable, but not manoeuvrable, requiring large control deflections to disturb it from equilibrium. Aircraft are designed to place pitch stiffness C_{M_α} within stability and controllability limits.

A.5 Static Lateral-Directional Stability

The lateral stability is concerned with the roll moment l and yaw moment N as shown in Figure A.8.

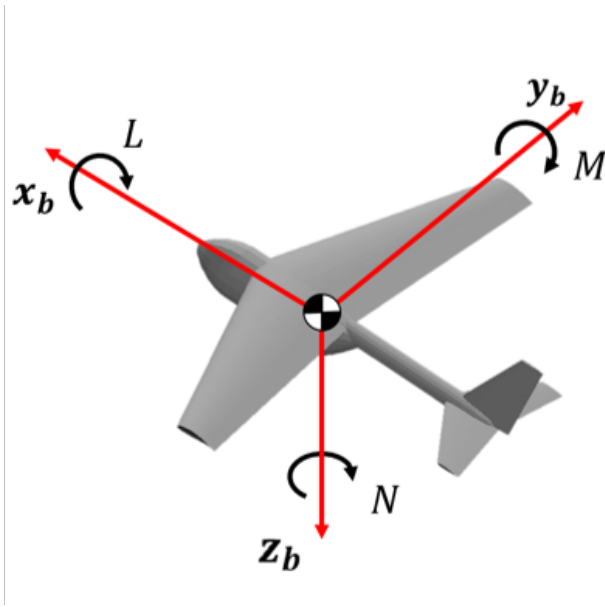


Figure A.8: Pitch, yaw and roll moments

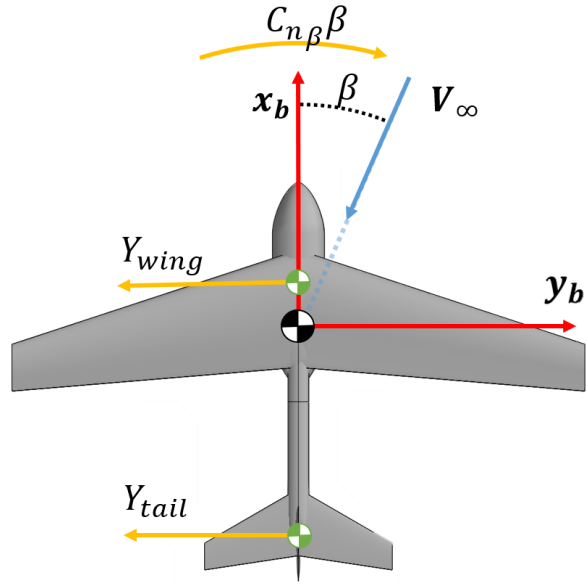


Figure A.9: Aircraft experiencing a sideslip disturbance

The roll and yaw moments can be normalised and converted into coefficients, shown in Equations A.13 and A.14.

$$C_l = \frac{l}{\frac{1}{2}\rho V_\infty^2 S b} \quad (\text{A.13})$$

$$C_n = \frac{N}{\frac{1}{2}\rho V_\infty^2 S b} \quad (\text{A.14})$$

The lateral-directional stability is dependant on change in lateral moments C_N and C_l with disturbances in sideslip angle. The derivative of the yaw moment C_N with respect to sideslip is called the yaw stiffness, shown in Equation A.15.

$$C_{n_\beta} = \frac{\partial C_N}{\partial \beta} \quad (\text{A.15})$$

For an aircraft to be directionally stable, a positive sideslip disturbance must cause a positive C_n change. A positive C_{n_β} change re-aligns the aircraft body axes with the wind axes and reducing sideslip.

$$C_{n_\beta} > 0 \quad \text{for stability} \quad (\text{A.16})$$

The derivative of roll moment with respect to sideslip is called the dihedral effect, shown in

Equation A.17.

$$C_{l_\beta} = \frac{\partial C_l}{\partial \beta} \quad (\text{A.17})$$

When experiencing a positive sideslip disturbance, a laterally stable aircraft will generate a negative rolling moment. As the aircraft rolls away from the relative wind flow, the rising wing generates more drag than the opposite wing, yawing the back to alignment with the air path.

$$C_{l_\beta} < 0 \quad \text{for stability} \quad (\text{A.18})$$

Similar to the longitudinal stability, an aircraft that is too stiff in yaw or roll (large positive C_{N_β} and large negative C_{l_β}) can become very unmanoeuvrable and difficult to control. Hence, feasible C_{l_β} and C_{N_β} values are constrained by stability and controllability limits.

Appendix B

VAP 3.5 Input Settings

VAP 3.5 is written in MATLAB and is run using an XML input file. The XML input file includes many fields which define the simulation settings, solver settings, flight conditions, vehicle geometry and propeller geometry. This chapter outlines the fields used to run the VAP 3.5 method.

B.1 Simulation Settings

The simulation settings are passed into fcnVAP_MIN.m in the VAP_IN structure.

- print - toggles VAP printing iteration history to command window
- plot - toggles VAP plotting simulation geometry
- viscous - toggles viscous correction of aerodynamic forces
- circplot - toggles vorticity distribution plotted on aircraft geometry
- gif - toggles gif generation
- verbose - toggles plotting panel index on aircraft geometry
- plotuinf - toggles quiver plots showing free stream flow direction
- gpu - toggles use of gpu in calculation

B.2 Solver Settings

The solver settings are passed into fcnVAP_MAIN.m in the input XML file.

- settings - defines start of solver settings

- relax - toggles wake relaxation
- steady - selects quasi-steady or unsteady solver
- maxtime - maximum number of iterations
- delta_time - time step size (seconds)
- start_forces - times at which force calculation begins
- stiff_wing - toggles rigid and elastic structure model
- fixed_lift - toggles fixed lift analysis in which velocity is calculated to match lift to aircraft weight
- gust_mode - toggles the use of the gust model

B.3 Flight Conditions

Basic properties of the operating conditions

- conditions - defines start of flight condition settings
- density - air density (kg/m³)
- kin_viscosity - air kinematic viscosity (m²/s)
- gust_amplitude - gust amplitude (m/s)
- gust_length - gust length (seconds)
- gust_start - time at which gust starts (seconds)

B.4 Vehicle and Propeller Geometry

All DVE panels for the fuselage and lifting surfaces are defined here.

- vehicle - defines start of vehicle settings
- global_x - location of vehicle x origin (m)

- global_z - location of vehicle y origin (m)
- global_y - location of vehicle z origin (m)
- speed - free stream velocity (m/s)
- weight - aircraft mass, ignored if not using fixed lift analysis
- interference_drag - percent of drag correction increase
- alpha - angle of attack (deg)
- beta - sideslip angle (deg)
- roll - roll angle (deg)
- fpa - flight path angle (deg)
- track - heading track of vehicle (deg)
- radius - defines turning radius of vehicle (deg)
- ref_area - wing area (m²)
- ref_span - wing span (m)
- rec_cmac - mean aerodynamic chord (m)

Each lifting surface is then defined within the vehicle settings, using the following fields.

- wing - defines start of wing settings
- symmetry - toggles geometry reflection about x-z plane
- incidence - vehicle geometry incidence angle (deg)
- triangular_elements - toggles use of triangle DVEs
- chordwise_elements - number of chordwise DVEs
- vehicle_x - reference x origin for panel coordinates (m)
- vehicle_y - reference y origin for panel coordinates (m)
- vehicle_z - reference z origin for panel coordinates (m)

Each panel is defined within the wing settings, using the following fields:

- panel - defines start of settings for a distinct panel
- spanwise_elements - number of spanwise DVEs
- strip_airfoil - airfoil name of local panel
- wing_x - x position of the panel leading edge vertex (m)
- wing_y - y position of the panel leading edge vertex (m)
- wing_z - z position of the panel leading edge vertex (m)
- chord - chord length of panel (m)
- twist - wing twist of panel (deg)

Similarly, the propeller geometry is defined:

- rotor - defines start of propeller settings
- rpm - revolutions per minute (rpm)
- collective - collective pitch shift of propeller blade (deg)
- ref_diam - propeller diameter (m)
- rotation_direction - rotation direction, defined as either CW for clockwise or CCW for counterclockwise
- veh_x_hub - x location of propeller hub (m)
- veh_y_hub - y location of propeller hub (m)
- veh_z_hub - z location of propeller hub (m)
- veh_x_axis - x component of the propeller direction unit vector
- veh_y_axis - y component of the propeller direction unit vector
- veh_z_axis - z component of the propeller direction unit vector
- blades - number of propeller blades

- chordwise_elements - number of chordwise DVEs on propeller blades

The propeller blade DVEs are defined similar to the wing panels:

- spanwise_elements - number of spanwise DVEs
- strip_airfoil - airfoil name of local panel
- rotor_x - defines x position of panel DVE with respect to hub and vehicle x-y plane (m)
- rotor_y - defines y position of panel DVE with respect to hub and vehicle x-y plane (m)
- rotor_z - defines z position of panel DVE with respect to hub and vehicle x-y plane (m)
- chord - chord length of panel (m)
- twist - blade twist of panel (deg)

Appendix C

Extra Optimisation Figures

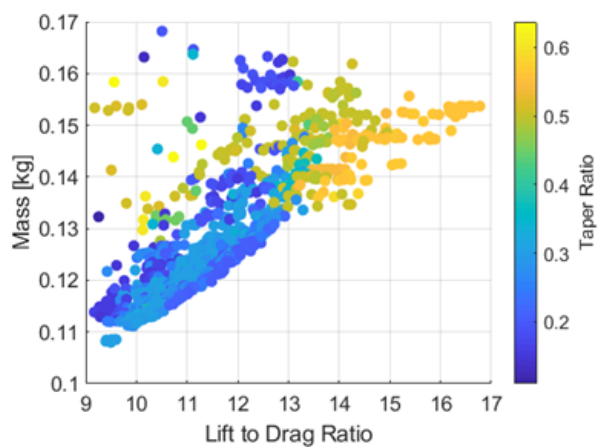


Figure C.1: Winglet 30cm: Taper

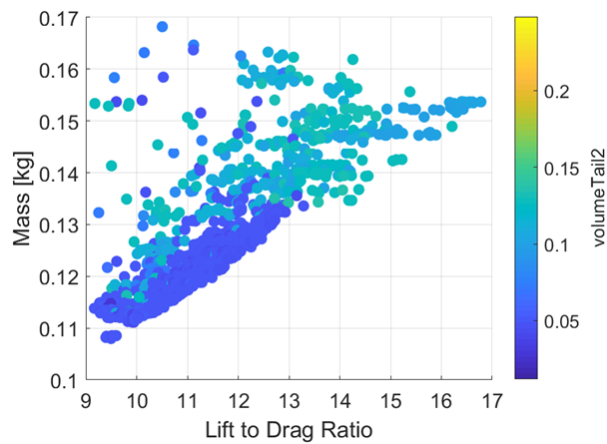


Figure C.2: Winglet 30cm: Winglet Volume

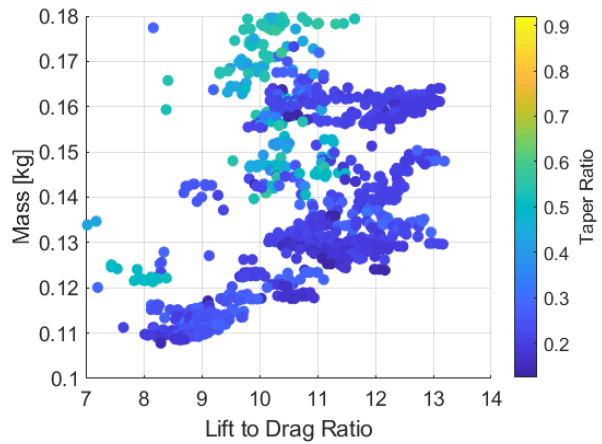


Figure C.3: Winglet 30cm with 4" prop: Taper

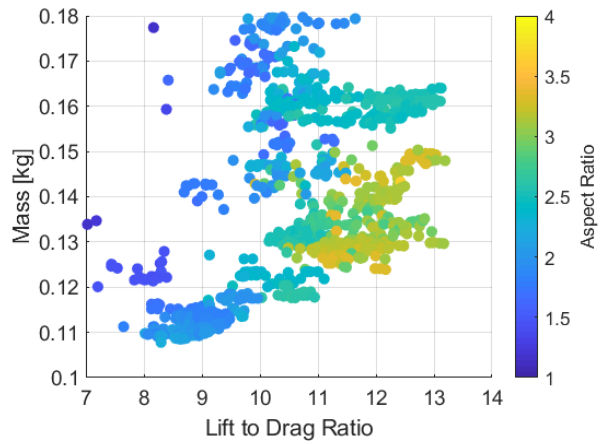


Figure C.4: Winglet 30cm with 4" prop: Winglet Volume

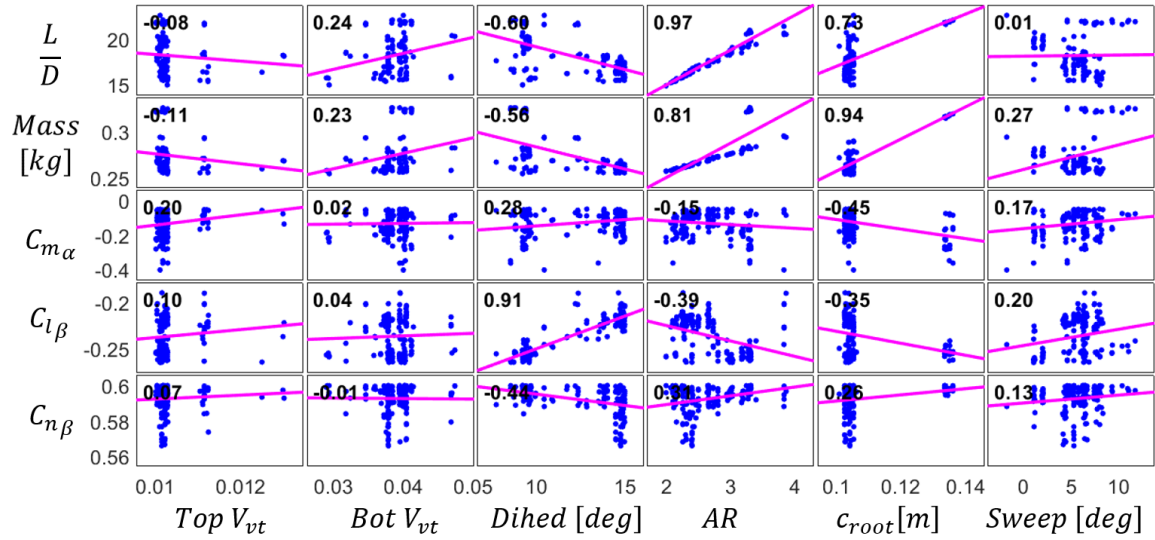


Figure C.5: Variable correlations for the 45cm Flying Wing optimisation without propeller

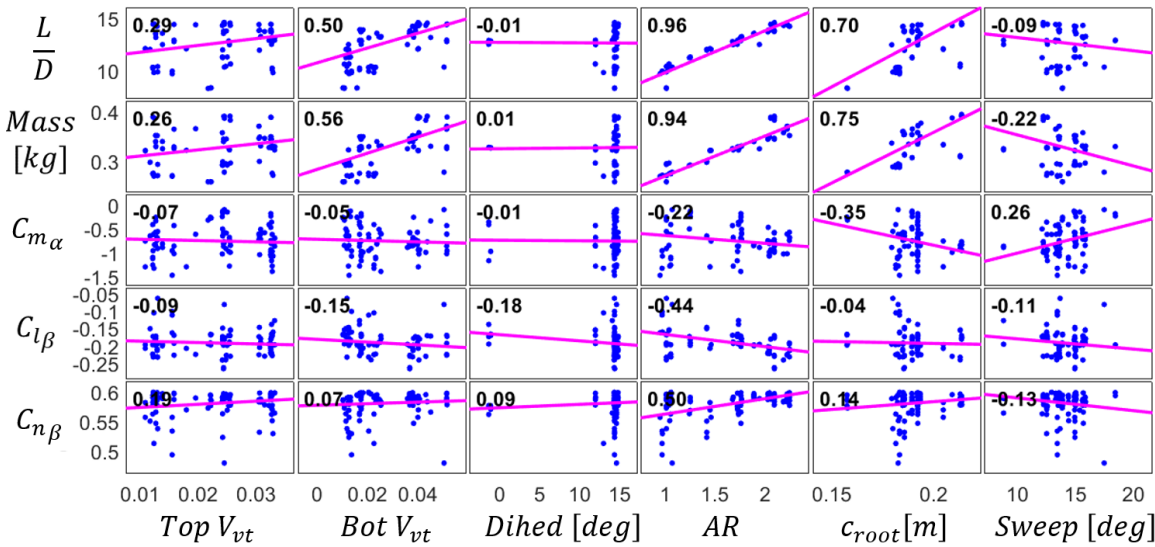


Figure C.6: Variable correlations for the 45cm Flying Wing optimisation with GWS5x4.3